

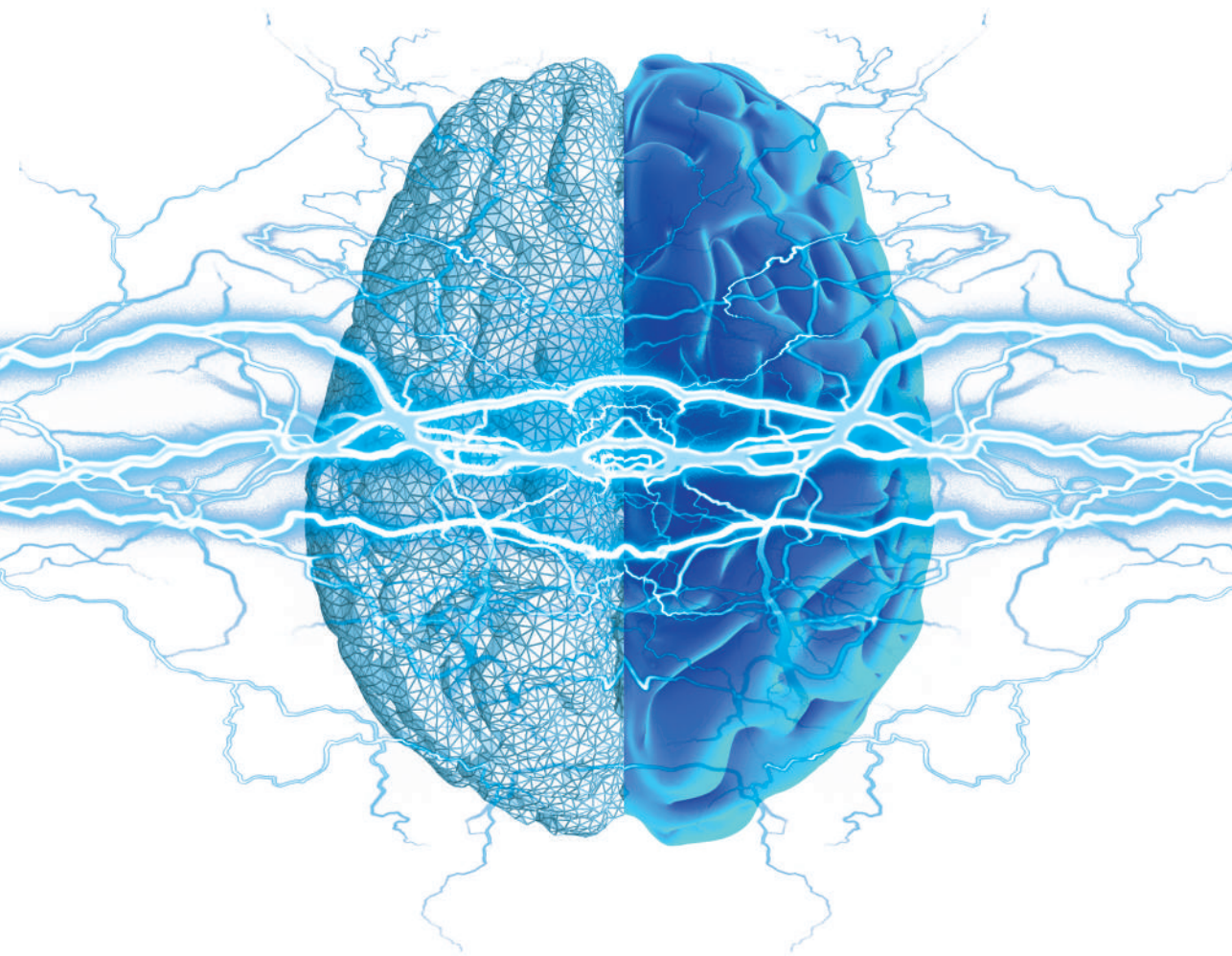
## PDF hosted at the Radboud Repository of the Radboud University Nijmegen

The following full text is a publisher's version.

For additional information about this publication click this link.

<http://hdl.handle.net/2066/134524>

Please be advised that this information was generated on 2016-06-08 and may be subject to change.



# Simulation of stimulation

On modeling and measuring the effects of transcranial  
direct current stimulation on the human brain

**Sumientra Rampersad**



# Simulation of stimulation

On modeling and measuring the effects of transcranial  
direct current stimulation on the human brain



© 2014 Sumientra Rampersad

All rights reserved. No part of this work may be reproduced or transmitted in any form or by any means without permission of the author.

Cover design: In Zicht Grafisch Ontwerp, Arnhem, the Netherlands

Layout: Sumientra Rampersad

Print: Ipskamp Drukkers, Enschede, the Netherlands

ISBN: 978-94-6259-510-1

The research presented in this thesis was carried out at the Department of Neurology of the Donders Institute for Brain, Cognition and Behaviour and the Radboud University Nijmegen Medical Centre in Nijmegen, the Netherlands. The project was conducted within the context of the BrainGain consortium that was financially supported by the Smart Mix Programme of the Netherlands Ministry of Economic Affairs and the Netherlands Ministry of Education, Culture and Science. Printing of this thesis was financially supported by the Radboud University Nijmegen Medical Centre.

# Simulation of stimulation

On modeling and measuring the effects of transcranial  
direct current stimulation on the human brain

Proefschrift ter verkrijging van de graad van doctor  
aan de Radboud Universiteit Nijmegen  
op gezag van de rector magnificus prof. dr. Th.L.M. Engelen  
volgens besluit van het college van decanen  
in het openbaar te verdedigen  
op woensdag 21 januari 2015 om 16.30 uur precies

door

**Sumientra Rampersad**  
geboren op 22 juli 1984  
te Ermelo

**Promotor**

Prof. dr. ir. D.F. Stegeman

**Copromotor**

Dr. T.F. Oostendorp

**Manuscriptcommissie**

Prof. dr. G. S. E. Fernández

Prof. dr. A. J. van Opstal

Prof. dr. N. F. Ramsey (UMC Utrecht)

# Contents

Abbreviations and symbols	vii
Introduction	ix
1 Stimulation and simulation	1
2 Modeling the layered structure of the skull	25
3 Volume conduction effects of various tissue types	43
4 Electric field distributions for six conventional configurations	67
5 Optimization of electrode placement	91
6 Measuring the effects of optimized configurations on excitability	111
7 Conclusion	127
References	139
Samenvatting	151
Dankwoord	161
Curriculum vitae	169



# Abbreviations and symbols

## Abbreviations

A1	primary auditory cortex
AEF	auditory evoked fields
AMP	amplitude change
ANG	angular change
cGM	cerebellar gray matter
CSF	cerebrospinal fluid
cWM	cerebellar white matter
DLPFC	dorsolateral prefrontal cortex
DTI	diffusion tensor imaging
DW	diffusion-weighted
EC	eddy current
ECT	electroconvulsive therapy
EEG	electroencephalography
EMG	electromyography
EIT	electrical impedance tomography
FDI	first dorsal interosseus
FEM	finite element method
FOV	field of view
GM	gray matter
IFG	inferior frontal gyrus
M1	primary motor cortex
MAG	relative magnitude factor
MEG	magnetoencephalography
MEP	motor-evoked potential
MRI	magnetic resonance imaging

PAR	parallelity
RDM	relative difference measure
SOA	supraorbital area
T1/T2w	T1/T2-weighted
tACS	transcranial alternating current stimulation
tDCS	transcranial direct current stimulation
TE	echo time
TES	transcranial electric stimulation
TI	inversion time
TES	transcranial electric stimulation
TMS	transcranial magnetic stimulation
TR	repetition time
tRNS	transcranial random noise stimulation
WM	white matter

## Symbols

$\sigma$	conductivity [S/m]
$I$	current [A]
$\vec{J}$	current density [A/m <sup>2</sup> ]
$\rho$	charge density [C/m <sup>2</sup> ]
$\vec{E}$	electric field [V/m]
$\phi$	electric potential [V]
$\mathbf{B}$	magnetic field [T]
$\hat{n}$	normal vector
$\mu_0$	permeability of free space [F/m]
$\epsilon_0$	permittivity of free space [F/m]

# Introduction

Transcranial direct current stimulation, tDCS for short, is a technique that uses weak currents sent through electrodes on the scalp to transiently alter characteristics of the brain. Targeting specific cortical areas researchers have employed tDCS to influence motor functioning, emotion, memory, language processing and various other cognitive functions. Positive results have been reported in studies aiming to improve functioning in both healthy people and patients suffering from neuropathological conditions like depression and epilepsy. Although results of this safe and simple technique are promising, its effects can be rather small or short-lived and striving for improvement is indicated.

Volume conduction modeling has emerged as a valuable tool in the field of non-invasive brain stimulation. By creating a realistic *in silico* representation of the human head, it is possible to calculate the electric field resulting from tDCS inside the brain. Such simulations provide answers to questions as 'Where in the brain is the electric field maximal?' and 'What is the direction of the field relative to the neuronal fibers?', information that is highly valuable to better understand a technique with working mechanisms that are largely unknown. Furthermore, as possible variations in the application of tDCS are numerous, modeling has become a critical component in the process of improving and individualizing the technique and its outcome.

This thesis investigates the electric field distribution resulting from tDCS aiming to both better understand and improve the technique. Chapter 1 provides extensive background information covering the history, application, targets and effects of tDCS. After giving an introduction to volume conduction modeling, the chapter continues with an overview of the current state of affairs in the field of tDCS simulations and concludes with a description of what this thesis will add to that field.

Chapters 2 and 3 are dedicated to investigating the efficiency and accuracy of certain modeling approaches. Growing computational capabilities have allowed more detail to tDCS models, but every extra detail comes at a cost. Therefore, these chapters investigate the influence of adding certain features to a model. The skull, an

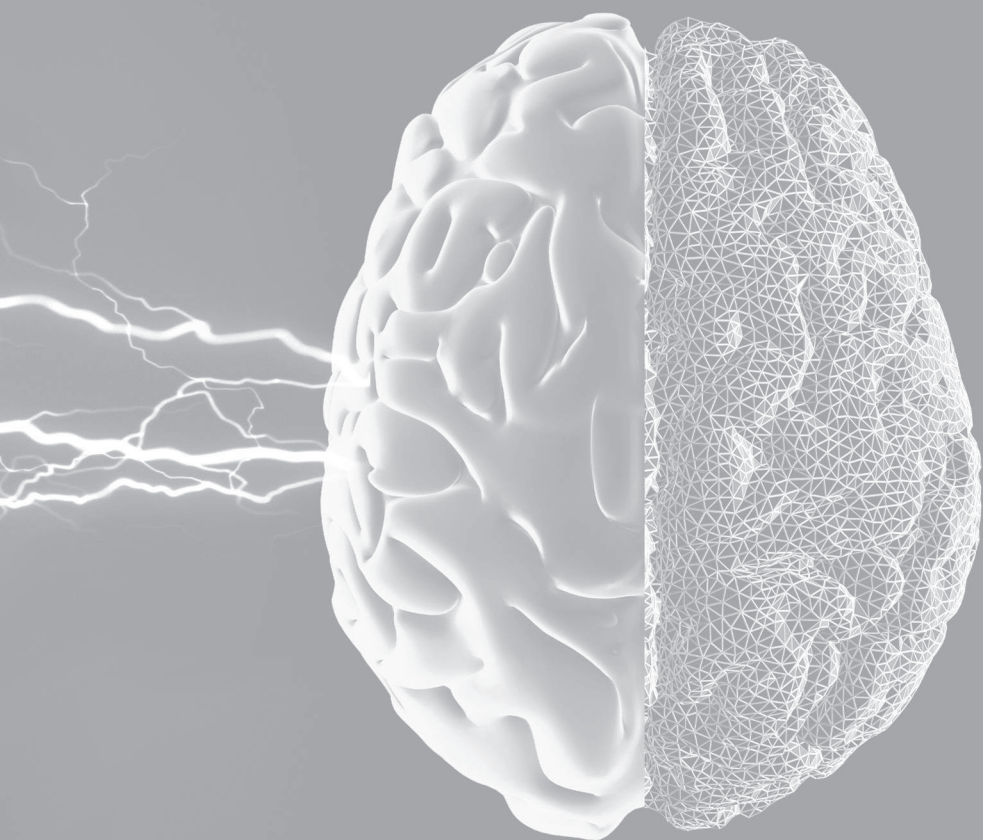


important barrier to the transcranial current, is studied in Chapter 2 using a spherical representation of the head. The influence of various other tissues is studied in Chapter 3.

The thesis continues with models of conventional and optimized tDCS. Using the currently most detailed model for tDCS, Chapter 4 describes the electric field distributions resulting from six conventional electrode configurations targeting different brain structures. As these conventional methods lead to suboptimal field strengths in the targeted areas, Chapter 5 explores a method to maximize this parameter. Additionally, field strength in the presumably most effective direction is optimized. These two optimal configurations are then experimentally compared with each other and with the conventional configuration in Chapter 6. These experiments not only serve as a validation of the modeling outcome and verification of the optimal configuration, but also allow insights into the mechanisms behind tDCS.

Chapter 7 provides a summary of the thesis, before discussing the main findings of all chapters in relation to each other and highlighting points for future research.









## 1.1 Transcranial direct current stimulation

After a long history of applying currents to the brain primarily as treatment for psychiatric illness, the present-day technique of transcranial direct current stimulation (tDCS) is a safe and easy means of temporarily altering neural excitability. The technique is used to investigate and improve brain function in both patients and healthy subjects.

### 1.1.1 Historical perspective

The use of electric currents for medical treatment dates back to Greek and Roman times. Pulses of current issued by live torpedo fish held against the human body were used for their transient analgesic effects. Around 43–48 CE Roman physician Scribonius Largus prescribed in his *Compositiones*<sup>a</sup> the use of torpedo fish to cure headaches<sup>[74]</sup>. This not only constitutes the first documented use of electricity as a medical treatment, but it is also the first application of transcranial brain stimulation.

#### 18th century: Animal electricity

Although electric fish were long used as medical treatment, scientific studies of animal electricity only started in the 18th century. John Walsh's investigations of the shocks produced by electric eels<sup>b</sup>, carried out between 1772 and 1775, inspired the work of Luigi Galvani, which would become the basis of modern electrophysiology<sup>[161]</sup>. Observing muscle twitches in dead frog legs upon touching them with metal, Galvani claimed in a now-famous essay<sup>c</sup> that electric sparks could trigger intrinsic animal electricity. Fellow Italian physicist Alessandro Volta applauded Galvani's experiments, but did not agree with the interpretation. He believed that the electricity was actually generated by connecting two dissimilar metals. Determined to prove this theory and disprove Galvani, Volta invented the *voltaic pile*, a stack of alternating dissimilar metals, organized much like the electric organs of torpedo fish. Volta's apparatus was able to deliver a steady direct current and would become the precursor of the modern-day battery. Ironically, Giovanni Aldini then used this device in a series of experiments aimed to defend his uncle Galvani<sup>[115]</sup>. Aldini first applied *galvanism* (direct currents) to dead animals like birds and oxen, producing muscle twitches by direct stimulation of the muscles, but also via stimulation of

<sup>a</sup>Scribonius Largus. *De compositionibus medicamentorum liber unus* (Ed. Jean Ruel, Paris, 1528).

<sup>b</sup>Walsh only described his findings in a 1773 letter that was read before the Royal Society.

<sup>c</sup>Aloysii Galvani. *De viribus electricitatis in motu musculari commentarius* (Bologna, 1791).

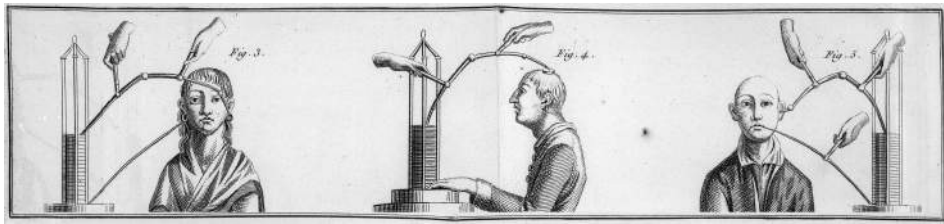


**Figure 1.1** Reproduction of plate 5 from Luigi Aldini's 1804 essay, illustrating how he applied *galvanism* to patients with mental disorders. The middle panel shows Luigi Lanzarini, a farmer suffering from depression before he was cured by Aldini's treatment that consisted of direct currents sent through the head. Optimal effects were reached by connecting a voltaic pile to head and hands. If this was not possible, Aldini used other locations (left and right panels)<sup>[115]</sup>. This illustration was acquired from the Wellcome Library, London.

the brain<sup>a</sup>. In 1802 Aldini reproduced these results on human cadavers. As Aldini believed electricity to be a useful medical tool, he also started applying it to treat patients with mental disorders. Via metal arcs connected to the bottom and top of a voltaic pile, he applied currents to patients' heads (Fig. 1.1). At least one documented account exists of Aldini successfully treating a man for *melancholia* (depression)<sup>[115]</sup>.

## 20th century: Systematic studies

Several other researchers used direct currents as stimulating or sedative treatment and successful treatments of depression were reported, but results were variable. Due to the higher success rate of electroconvulsive therapy (ECT, electricity-induced seizures) in treating depression, interest in brain polarization declined from the 1940s on<sup>[122]</sup>.

In the 1960s, a series of electrophysiological measurements in animals produced the first direct evidence of the effects of current stimulation to the brain and shed some light on its working mechanisms. The effects of polarizing currents on neuronal cells were investigated by applying currents directly to the cortex and measuring from within the cortex. Anodal polarization, i.e. with the positive electrode on or just inside the cortex, in anesthetized cats<sup>[28,125]</sup> and rats<sup>[15]</sup> led to increases in both spontaneous neural activity and in the size of sensory evoked potentials. Cathodal polarization resulted in decreased effects. These polarity-dependent effects were reversed for deeper lying neurons<sup>[28]</sup> and non-pyramidal tract neurons<sup>[125]</sup> in the motor cortex, suggesting that the type of neuron and its direction with respect to the

<sup>a</sup>Jean Aldini. Essai théorique et expérimental sur le galvanisme, avec une série d'expériences faites devant des commissaires de l'Institut national de France, et en divers amphithéâtres anatomiques de Londres (Paris, 1804).

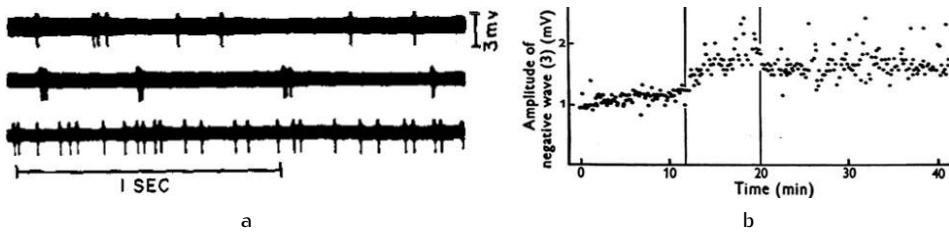


**Figure 1.2** Intracortical recordings after brain polarization in anesthetized animals (adaptation of figures from Creutzfeldt et al.<sup>[28]</sup> (a) and Bindman et al.<sup>[15]</sup> (b)). Currents applied directly to the cortex affected both spontaneous neural activity and sensory evoked potentials. a) Neural activity (top panel: control) was decreased after surface-negative (middle) and increased after surface-positive polarization (bottom) in cats. b) The peak amplitude of the sensory evoked potential (third negative wave) in rats increased after a surface-positive current was passed through the cortex between the 12th and 20th minute.

current were influential to the outcomes. Furthermore, these effects not only occurred during stimulation, but dependent on stimulation duration could be retained for hours after<sup>[15]</sup>.

Over the following years, several studies were published of brain polarization applied to both humans and animals to induce behavioral changes. Treatment of depression was still the most common application, with several clinicians reporting improvements in mood during and after stimulation<sup>[82,25,9]</sup>. Currents were consistently applied with one or two positive electrodes on the forehead and a reference on an arm or leg, but other stimulation parameters were as varied as the patients they were applied to. A first randomized controlled trial, stimulating 24 patients 8 hours daily for 14 days, found a significant difference between real and placebo treatment<sup>[27]</sup>. Improvements were also seen in schizophrenic<sup>[133]</sup> and manic patients<sup>[24]</sup>, while other studies reported no effects in similar populations<sup>[80,7]</sup>. In the same period, the first reports emerged of stimulating healthy subjects. Positive results included increased alertness<sup>[82]</sup> and faster responses in motor tasks<sup>[37]</sup>, while a study by Hall et al.<sup>[59]</sup> showed no effect on mood nor on a verbal learning task. Improved task performance was also shown in monkeys for a reaction time task<sup>[135]</sup> and rats for learning avoidance responses<sup>[2,150]</sup> after direct stimulation of the dorsolateral pre-frontal cortex.

### 1.1.2 Measuring corticospinal excitability

In the 1980s new techniques were developed for direct measurements of neuronal excitability of the brain. Excitability can be evaluated by inducing action potentials in cortical neurons. Note that the weak brain stimulation described above does not



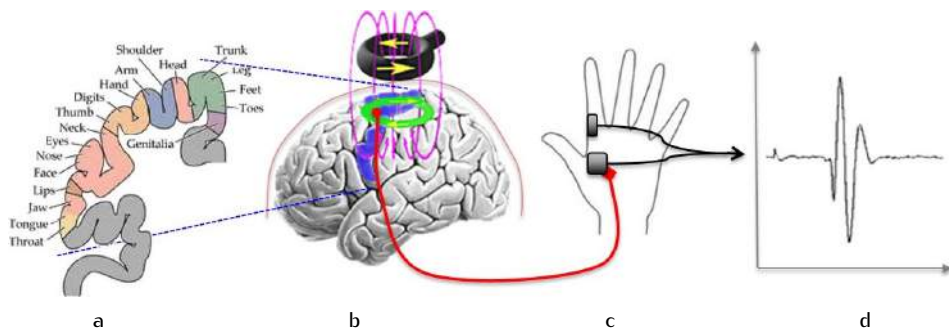


**Figure 1.3** Measuring motor cortical excitability using TMS and EMG. Sending a current pulse through a coil held to the scalp (b) induces a magnetic field (pink lines) that penetrates the skull and induces an electric field in the brain (green circle). When applied over M1 (blue area), this field can evoke action potentials in the cortical motor neurons. Due to the division of the motor cortex into distinct areas representing certain muscle groups (a), a specific muscle can be targeted. The resulting muscle activity can be measured on the skin with EMG (c), producing a characteristic motor evoked potential (d). The placement of EMG electrodes indicated here is used for measurements of the FDI muscle.

induce action potentials. Electric activation of cortical neurons had previously only been possible by direct stimulation of the cortex. Transcranially inducing action potentials was too painful due to the resistive skull and skin fat necessitating high currents. After promising results had been reported of transcranial electric stimulation with very brief pulses<sup>[94]</sup>, and magnetic induction had been shown able to activate nerves in the arm<sup>[121]</sup>, both concepts were finally combined into transcranial magnetic stimulation (TMS).

In 1985, Anthony Barker and colleagues<sup>[10]</sup> developed a stimulator that could send a strong, brief current pulse<sup>a</sup> through a 10 cm diameter coil. The current in the wire induces a magnetic field around it that, due to its rapid change, induces an electric field<sup>b</sup> (Fig. 1.3b). When the coil is held tangentially to the scalp, the magnetic field penetrates the scalp and skull without significant attenuation and electric fields are induced in the brain without causing discomfort. The fields induced in the brain are directed parallel and opposite to the currents in the coil. This induced field can depolarize neurons that lie underneath the coil and evoke the discharge of action potentials.

If a TMS pulse is applied over the primary motor cortex (M1) of the brain (Fig. 1.3a,b), the underlying cortical neurons are activated and send impulses along the corticospinal tract via the spinal motoneurons to the muscle fibers they innervate.

<sup>a</sup>Peak of 4 mA after 110  $\mu$ s.

<sup>b</sup>More information on electromagnetic fields and induction can be found in Section 1.2.1.

This muscle activity, contralateral to the stimulated M1, can be observed as a muscle twitch and can be recorded on the skin using electromyography (EMG). The motor evoked potential (MEP), measured via electrodes on the skin over the muscle (Fig. 1.3c,d), provides a measure of the excitability of the cortical neurons that project to the muscle.

As the general organization of the motor cortex into distinct areas that project to specific muscle groups is well known, individual muscles can be targeted. For measurements of M1 excitability investigators commonly target muscles of the hand, such as the first dorsal interosseus muscle (FDI), which moves the index finger towards the thumb (Fig. 1.4c). Used in this way, the technique is referred to as single-pulse TMS; TMS can also be applied repetitively (rTMS) to induce excitability changes in the brain. For neuroscientific research, TMS is mostly applied using a figure-of-eight coil that produces a peak electric field under the intersection of its two rings, leading to more focal stimulation.

### 1.1.3 Effects of tDCS

Early reports of transcranial polarization of the brain had primarily been descriptive studies. When measurements of corticospinal excitability via TMS became possible, allowing the unambiguous demonstration of the efficacy of tDCS, a new era began for tDCS as a popular neuroscientific instrument.

#### Electrophysiological measurements

Priori et al.<sup>[123]</sup> were the first to employ TMS to quantitatively evaluate the effects of tDCS. They were also the first to apply DC currents via two large electrodes attached to the head, specifically over the motor cortex and to the chin. At the end of a 7-second session of anodal tDCS (positive electrode over M1), a consistent decrease in MEP size was seen compared to before stimulation. The depression in MEP size was proportional to the stimulation current.

Applying similar techniques, Nitsche & Paulus<sup>[108,109]</sup> confirmed and expanded these findings on tDCS-elicited excitability changes with a series of experiments that would become the basis of future tDCS applications. In their first experiment, they measured TMS-evoked motor potentials of the right hand before and at the end of a 4-second period of tDCS in 10 healthy volunteers. Of the six electrode configurations that were tested, only one resulted in significant changes in MEP size for both current directions (Fig. 1.4). Therefore, this montage, which consisted of one electrode over the motor cortex and one over the contralateral supraorbital area (SOA), was used for the remaining experiments. In agreement with previous animal

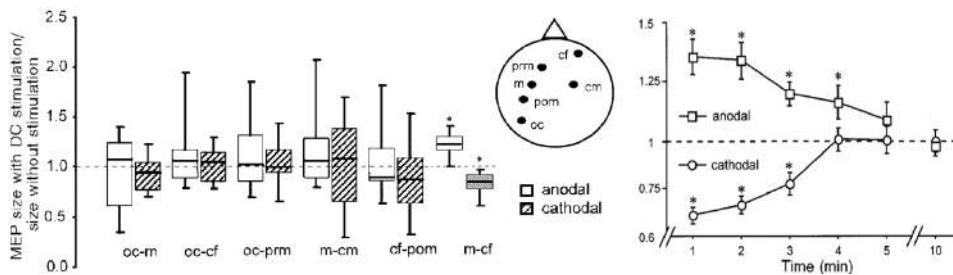


**Figure 1.4** The first measurements of corticospinal excitability changes resulting from tDCS (adaptation of figures from Nitsche & Paulus<sup>[108]</sup>). Six electrode configurations were tested for their effects on excitability during both anodal and cathodal tDCS (left panel). Only the motor cortex – forehead (m-cf) configuration was found effective for both polarities and was therefore selected for a series of follow-up experiments. Excitability was either increased (anodal tDCS) or decreased (cathodal tDCS) for several minutes after stimulation with a duration of 5 minutes (right panel).

studies, anodal stimulation increased and cathodal stimulation decreased cortical excitability. Further experiments showed that these excitability changes could persist for minutes after stimulation had stopped if a current of at least 0.6 mA was applied for at least 3 minutes<sup>[108]</sup>. Further increases in stimulation duration progressively increased the duration of the effects, but not the size. Aftereffects lasting up to 90 minutes were reported for 13 minutes of anodal stimulation<sup>[109]</sup> and up to 60 minutes for 9 minutes of cathodal stimulation<sup>[107]</sup>.

## Functional effects

The findings of Nitsche and Paulus attracted new attention to transcranial DC stimulation. Since the year 2000, the number of publications using tDCS has grown roughly exponentially. With the ability to selectively induce significant yet transient excitability changes, the technique seemed effective, simple and safe. Hence investigators started using tDCS to target various areas of the brain in both healthy subjects and patients suffering from neurological conditions.

The original target for DC stimulation, depression, has remained an important focus in clinical studies. Several placebo-controlled trials resulted in significantly diminished depression scores after a series of daily tDCS sessions, with effects lasting for at least a month<sup>[19,84]</sup>. The use of tDCS to treat depression is currently only surpassed by its popularity for stroke treatment<sup>[104]</sup>. Motor recovery after stroke was shown to be improved in the paretic hand<sup>[66]</sup> and ankle<sup>[86]</sup>. Both anodal stimulation of the affected and cathodal stimulation of the unaffected side were associated with

motor improvements<sup>[45,18]</sup>. Combining tDCS with physical therapy can improve the effects of each intervention by itself<sup>[81]</sup>. Other patient groups for which symptomatic improvement has been reported include patients with migraine<sup>[146]</sup>, Parkinson's disease<sup>[47]</sup>, obesity<sup>[100]</sup>, Alzheimer's disease<sup>[17]</sup>, epilepsy<sup>[50]</sup> and people suffering from chronic pain<sup>[16]</sup> due to fibromyalgia<sup>[48]</sup> or spinal cord injury<sup>[44]</sup>. Although positive effects have been reported, the improvements were often small and disappeared within hours after stimulation. For tDCS to be viable as a clinical therapy the after-effects should be prolonged. This might be achieved by repetitive application of tDCS<sup>[18,44,19,81]</sup>.

DC stimulation has increasingly been employed to modulate cognitive functioning in healthy subjects. The majority of these studies targeted either the motor cortex or the dorsolateral prefrontal cortex (DLPFC) to influence learning or memory. Improvements in visuomotor learning were shown after anodal stimulation of M1 or visual area V5<sup>[5]</sup>, using a visually guided tracking task. Anodal tDCS of the left DLPFC enhanced working memory in a letter memory paradigm<sup>[46]</sup> and increased verbal fluency<sup>[69]</sup>. Several other investigators reported improved learning or memory after anodal tDCS, while in other studies no results or even impaired performances were found<sup>[104]</sup>. DC stimulation was also shown to be effective in an experimental study on deceptive behavior<sup>[124]</sup> and to be able to influence verbal insight problem solving<sup>[95]</sup>, demonstrating the versatility of the possible applications.

#### 1.1.4 Application

Over the past decade, electrode and stimulation parameters for tDCS have been fairly consistent. Using these rather standardized settings, researchers have not reported any harmful adverse effects. Table 1.1 provides an overview of the most commonly targeted brain regions in recent literature with a wide range of applications.

##### Electrode and stimulation parameters

After Nitsche & Paulus<sup>[108]</sup> found only their 'M1 – contralateral forehead' montage to be effective in changing M1 excitability, this configuration soon became the standard to stimulate M1. When investigators started targeting other brain areas they adopted a similar approach. It eventually became standard practice to place one electrode, often described as the stimulating or active electrode, over the target area and a reference over the contralateral supraorbital area (SOA). Although this nomenclature has become accepted, it should be noted that it is not correct, as both electrodes stimulate equally, but oppositely. Some investigators make use of this

**Table 1.1** Brain areas that have been commonly stimulated with tDCS in recent studies with a wide range of applications. The locations of these areas in the brain can be seen in Fig. 4.7. Conventional electrode configurations for these target areas are presented in Table 4.1 and illustrated in Fig. 4.3.

Target area	Application
motor cortex hand area	motor recovery <sup>[21]</sup> , pain <sup>[167]</sup> , smoking <sup>[56]</sup>
M1 leg area	motor recovery <sup>[86]</sup> , spinal network excitability <sup>[134]</sup>
dorsolateral prefrontal cortex	appetite <sup>[100]</sup> , depression <sup>[84]</sup> , emotion <sup>[106]</sup> , memory <sup>[70]</sup> , pain <sup>[87]</sup> , problem solving <sup>[95]</sup>
inferior frontal gyrus	apraxia <sup>[89]</sup> , behavioral inhibition <sup>[35]</sup> , language <sup>[117]</sup> , motor resonance <sup>[38]</sup>
occipital cortex	migraine <sup>[146]</sup> , visual recovery <sup>[119]</sup>
cerebellum	cerebello-brain inhibition <sup>[54]</sup> , motor adaptation <sup>[71]</sup>

trait by placing the electrodes symmetrically for bihemispheric opposite stimulation of e.g. both motor cortices<sup>[81]</sup>. The most commonly used electrode locations for the target areas mentioned in Table 1.1 are presented in Chapter 4 (Table 4.2 and Fig. 4.3, p. 74). The most-used electrodes are 25–35 cm<sup>2</sup> flexible conductive rubber patches inserted in saline-soaked sponges.

When the anode, the positive electrode, is placed over the target area, we speak of anodal stimulation and otherwise of cathodal stimulation. It is generally accepted that anodal tDCS is excitative and cathodal tDCS inhibitive to the underlying cortex, but the opposite has been reported as well<sup>[162,85]</sup>. Anodal tDCS in general results in stronger and more consistent effects than cathodal tDCS and is used more often<sup>[104]</sup>. Direct current stimulation is commonly applied for 5–20 minutes with intensities of 1–2 mA.

Other forms of transcranial current stimulation have been developed over the past decades. Transcranial alternating current stimulation (tACS) uses largely the same methods and parameters as tDCS, but the applied current varies over time. Mostly a sinusoidally oscillating current is used that either switches polarity every half cycle<sup>[3,166]</sup> or is applied in combination with a DC offset<sup>[91,55]</sup>. Some investigators combined a spectrum of frequencies, producing transcranial random noise stimulation (tRNS)<sup>[153,23]</sup>. These time-varying modes of stimulation can affect excitability<sup>[153,55]</sup>

and brain function<sup>[3,23]</sup> similarly to tDCS, but can also modulate intrinsic oscillations of the brain<sup>[91,166]</sup>.

### Adverse effects

During stimulation, it is common for subjects to experience tingling, itching or burning sensations in the skin underneath the electrodes. These feelings, which mostly subside after a few minutes of stimulation, can be slightly painful. Actual skin burns have only been reported in one study in which impedance was extremely high due to incorrect application<sup>[104]</sup>; with correct application this should not occur. Furthermore, all certified stimulators are constructed to terminate stimulation if the impedance becomes too high. Adverse effects after stimulation can occur in the form of a mild headache or fatigue and rare cases of transient nausea and vertigo have been reported<sup>[104]</sup>.

Skin sensations can be reduced by using larger electrodes, resulting in a lower current density in the skin. As the strength of these sensations is proportional to the rate of change of the current, the feelings are strongest when the current is switched from 0 to 1 mA immediately. The sudden switching of the current can also induce phosphenes: perceiving a flash of light due to excitation of the retina by sources other than light<sup>a</sup>. Both experiences can be avoided by ramping the current up and down linearly over a few seconds at the start and end of stimulation, respectively.

### Sham stimulation

As with any intervention applied in clinical or neuroscientific research, some form of placebo treatment is required for systematic studies of the effects through randomized controlled trials. Placebo treatment for non-invasive brain stimulation is called sham stimulation. As subjects are only aware of tDCS stimulation through the skin sensations they may experience, sham stimulation is based on mimicking these sensations. Some subjects do no longer feel the currents once they have reached a constant level and for many others the feelings subside after a few minutes. In any case, the feelings are strongest at the start of stimulation. These effects are commonly exploited to apply placebo treatment by ramping the current up and immediately down at the beginning of a session.

---

<sup>a</sup>Phosphenes in the shape of spots or bars of light can occur due to electrical but also mechanical stimulation of the retina, e.g. by rubbing the eyes, or by stimulation of the visual cortex.

## 1.2 Volume conduction modeling

The electric field and current density induced in the human body by externally applied currents can be calculated using volume conduction models. A volume conductor is a continuous passive conducting medium; a volume conduction model is a model of its geometry and electromagnetic properties. The partial differential equations that govern the electromagnetic fields in such a conductive medium, accompanied with the prevailing boundary conditions, can then be solved analytically for some rare cases, and can be numerically approximated for more realistic geometries.

### 1.2.1 Electromagnetic fields

How electric and magnetic fields are mutually influenced by each other and by charges and currents is described by a set of equations that were proposed in an early form by James Clerk Maxwell<sup>[92]a</sup>:

$$\begin{aligned}
 (1) \quad \nabla \cdot \vec{E} &= \frac{\rho}{\epsilon_0} & (3) \quad \nabla \cdot \vec{B} &= 0 \\
 (2) \quad \nabla \times \vec{E} &= -\frac{\delta \vec{B}}{\delta t} & (4) \quad \nabla \times \vec{B} &= \mu_0 \left( \vec{J} + \epsilon_0 \frac{\delta \vec{E}}{\delta t} \right),
 \end{aligned} \tag{1.1}$$

where  $\vec{E}$  [V/m] is the electric field<sup>b</sup>,  $\vec{B}$  [T] the magnetic field,  $\vec{J}$  [A/m<sup>2</sup>] the current density,  $\rho$  [C/m<sup>3</sup>] the charge density,  $\epsilon_0$  [F/m] and  $\mu_0$  [N/A<sup>2</sup>] the permittivity and permeability of free space, respectively, and the vector differential operator  $\nabla = (\frac{\partial}{\partial x}, \frac{\partial}{\partial y}, \frac{\partial}{\partial z})$  describes the divergence ( $\nabla \cdot \vec{f}$ ) and curl ( $\nabla \times \vec{f}$ ) of a vector field ( $\vec{f}$ ). According to these equations an electric field is generated whenever a charge density distribution (Eq. 1.1.1) or a time-varying magnetic field (Eq. 1.1.2) is present and that a magnetic field is generated in the presence of a current density distribution or a time-varying electric field (Eq. 1.1.4)<sup>c</sup>. Because charge is conserved we know that

$$\nabla \cdot \vec{J} = -\frac{\delta \rho}{\delta t} \tag{1.2}$$

always holds. Finally, the constitutive equation

$$\vec{J} = \sigma \vec{E} \tag{1.3}$$

<sup>a</sup>Assuming the absence of dielectric or magnetic materials, the polarization and magnetization fields have been omitted from the equations presented here.

<sup>b</sup>In this book, vectors describing physical quantities that have magnitude and direction are displayed with arrows overhead; other vectors will be displayed in bold.

<sup>c</sup>The third law describes the non-existence of magnetic monopoles.

describes the relation between the electric field and the resulting current density inside a material with conductivity  $\sigma$ . The latter equation is the equivalent of Ohm's law ( $I = \frac{1}{R}V$ ) for volumetric current distributions. The conductivity  $\sigma$  [S/m] is a measure of the ability of a medium to conduct current; its reciprocal is resistivity  $\rho$  [Ωm]. The direction of the current density follows that of the electric field in an isotropic material;  $\sigma$  is then a scalar value. For materials in which the conductivity is anisotropic (directionally dependent), these properties can be conveyed by writing  $\sigma$  as a  $3 \times 3$  tensor  $\boldsymbol{\sigma}$ .

### Stationary fields

In a stationary situation, i.e. the fields do not change over time, Maxwell's equations can be simplified. In such a situation, the electric field has zero curl (Eq. 1.1.2) and can therefore be expressed as the gradient of a scalar potential field:

$$\vec{E} = -\nabla\phi, \quad (1.4)$$

with  $\phi$  defined as the electric potential. The right hand side of Equation 1.2 becomes zero as well, and by substituting Equations 1.3 and 1.4 into 1.2, we end up with Laplace's equation:

$$\nabla \cdot \boldsymbol{\sigma} \nabla \phi = 0. \quad (1.5)$$

Solving this partial differential equation results in a description of the potential field, from which other quantities such as the electric field (Eq. 1.4) and current density (Eq. 1.3) can be calculated.

### Quasi-static approximation

When the electromagnetic fields are not stationary but time-varying, they can still be treated in the same way as stationary sources if the temporal behavior stays within the low-frequency range. We say that quasi-stationary conditions apply if the effects of propagation, capacitance and induction are negligible. Via capacitance measurements of various tissues in living dogs<sup>[144]</sup> and in vivo impedance measurements of monkey cortical tissue<sup>[83]</sup>, it has been shown that the electric properties of biological tissues are primarily resistive for frequencies under 1 kHz. Plonsey & Heppner<sup>[118]</sup> later mathematically derived the criteria under which these simplifications can be made. Using the electromagnetic properties of biological tissues, they evaluated the errors resulting from these approximations and found that these indeed were negligible. Therefore, the quasi-static approximation can be applied for simulations of constant (tDCS) and slowly varying (tACS) electric brain stimulation.



## Boundary conditions

Laplace's equation describes the potential field in an infinite homogeneously conducting medium. If one wants to know the potential field in a closed volume conductor, the infinite medium description needs to be bounded by applying boundary conditions. Suppose we have a volume conductor domain  $\Omega$  with a boundary surface  $\delta\Omega$  surrounded by a non-conducting medium, like a human head surrounded by air, and we apply a potential  $\phi_0$  via electrodes to parts of the surface  $\delta\Omega_e$ . Current can flow in or out of the domain at  $\delta\Omega_e$  but not at the remainder of the surface  $\delta\Omega_{\sim e}$ . Here  $\vec{J} \cdot \hat{n} = 0$ , with  $\hat{n}$  the vector normal to the surface. Substituting Equations 1.3 and 1.4, the boundary conditions are:

$$\begin{aligned} (1) \quad \phi|_{\delta\Omega_e} &= \phi_0 \\ (2) \quad \sigma \nabla \phi \cdot \hat{n}|_{\delta\Omega_{\sim e}} &= 0. \end{aligned} \tag{1.6}$$

The Dirichlet boundary condition (Eq. 1.6.1) impresses the potential to the part of the surface interfacing with the electrodes and the Neumann boundary condition (Eq. 1.6.2) restricts current flow through the remainder of the surface.

### 1.2.2 The finite element method

For certain regular geometries with a homogeneous conductivity, Laplace's equation can be solved explicitly, the solution consisting of harmonic functions. In all other situations, having either inhomogeneous conductivities, a more complex geometry, or both, numerical methods are needed to approximate the solution. Possible approaches include the boundary element method, the finite difference method, the finite volume method and the finite element method (FEM). The latter was used for the research described in this thesis (Chapters 2–5) and will therefore be elaborated on here. A basic introduction to finite element analysis is provided in the next section. The mathematical derivation of the FEM is described separately.

#### Introduction to FEM

The finite element method is a mathematical technique for finding numerical approximations to partial differential equations. The method is widely applied in models of physical systems with applications ranging from fluid flow and heat transfer to structural mechanics and electromagnetics. The principle of finite element modeling is based on discretization. If the domain of interest is too complex for the governing equations to be solved analytically, the volume can be divided into many small subdomains of a regular shape. The solution can then be approximated by combining the equations that are set up for each individual element.

Objects of any shape can be reconstructed from tetrahedral building blocks (Fig. 1.7d). Tetrahedra and hexahedra are the most commonly used elements, but other geometries are possible as well. The approximation becomes increasingly accurate with decreasing element size, but as this leads to a higher number of elements, the computational burden increases as well. In order to be more computationally efficient, larger elements can be used in areas where the solution does not change quickly. The vertices of finite elements are referred to as nodes and the combination of all nodes and edges constitutes a mesh. Many software packages exist, both commercial and free, that can convert any geometry into a mesh. The input to such programs can be computer-aided design (CAD) models or boundary surface meshes consisting of triangles. In biomedical engineering, hexahedral models are often made directly from magnetic resonance images (MRI) by converting each voxel into a single element.

After the geometry is converted into a mesh, the relevant material properties need to be defined. When solving Laplace's equation (Eq. 1.5), a conductivity value has to be assigned to each element. Finally, the boundary conditions are applied. For example, with Dirichlet boundary conditions (Eq. 1.6), certain nodes at the surface of the mesh are assigned a potential  $\phi_0$ . Once all information about the geometry, conductivities and boundary conditions is available, the governing physical equations for the complete medium can be set up for each element individually and combined into a single matrix equation. The latter process is largely performed automatically by FEM software. By selecting an initial solution, calculating the resulting error and iterating until an error limit is reached, the equation is finally solved.

## Mathematical foundations

The FEM is a method for approximating the solution to a partial differential equation. Its mathematical derivation can be divided into three steps: 1) converting the partial differential equation into its weak form, 2) discretizing the problem, and 3) combining the discretized set of equations into a single matrix equation.

### 1. Weak formulation

Suppose we have a partial differential equation

$$-\nabla^2 u(\mathbf{x}) = f(\mathbf{x}) \quad \forall \mathbf{x} \in \Omega \quad (1.7)$$

and we want to approximate  $u(\mathbf{x})$ , the exact solution to this equation. The first step is to obtain the equation in its weak form. This is accomplished by multiplying both sides of the equation with a test function  $w(\mathbf{x}) \in W$  and then integrating over the

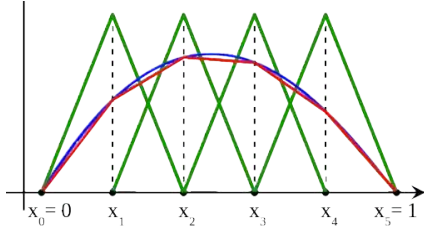


**Figure 1.5** Example of a finite element description in one dimension. A quadratic function (blue) is approximated by a piecewise linear function (red) that is reconstructed from a linear combination of basis functions (green).

domain  $\Omega$ :

$$-\int_{\Omega} (\nabla^2 u) w(\mathbf{x}) \, d\mathbf{x} = \int_{\Omega} f(\mathbf{x}) w(\mathbf{x}) \, d\mathbf{x}. \quad (1.8)$$

Using integration by parts<sup>a</sup> on the left-side, we obtain the weak formulation:

$$\int_{\Omega} \nabla u \cdot \nabla w \, d\mathbf{x} = \int_{\Omega} f(\mathbf{x}) w(\mathbf{x}) \, d\mathbf{x} \quad \forall w \in W. \quad (1.9)$$

## 2. Discretization

The next step uses Galerkin dimension reduction. Instead of trying to find a function  $u(\mathbf{x})$  that solves Equation 1.9 for all functions  $w \in W$ , we select a finite subset of functions  $W_h \subset W$  and try to find the function  $u_h \in W_h$  that solves the weak formulation for all  $w_h \in W_h$ . If we choose a basis<sup>b</sup>  $\{h_j\}_{j=1}^n$  for the subspace  $W_h$ , we can express  $u_h(\mathbf{x})$ , which is an approximation to the real solution  $u(\mathbf{x})$ , as a linear combination of these basis functions  $h_j(\mathbf{x})$  and constants  $\alpha_j$ :

$$u(\mathbf{x}) \approx u_h(\mathbf{x}) = \sum_{j=1}^N \alpha_j h_j(\mathbf{x}). \quad (1.10)$$

The discretization process is illustrated with an example in Figure 1.5. Suppose our domain  $\Omega$  is one-dimensional (1D) and the equation we are trying to solve (Eq. 1.7) is defined on  $[0,1]$ . In Figure 1.5, the  $x$ -axis represents the domain  $\Omega$  and the blue curve the solution  $u(x)$  that we want to approximate. We now discretize the domain by dividing it into several finite elements (line segments in 1D) connected by nodes ( $x_0 - x_5$ ). On each node  $n_j$  we place a basis function  $h_j(x)$ , for which we select the triangle function. This function has a value of 1 for  $h_j(n_j)$  and a value of 0 for all  $n_i$ , such that it is linear within an element and piecewise linear within the domain. By selecting suitable constants  $\alpha_j$ , a linear combination of these basis functions over all nodes (Eq. 1.10) results in a piecewise linear function  $u_h(x)$  that approximates  $u(x)$ , represented by the red line in Figure 1.5.

<sup>a</sup> $\int u(x) w'(x) dx = u(x) w(x) - \int u'(x) w(x) dx$

<sup>b</sup>A basis is a set of functions that, in a linear combination, can represent every continuous function in a function space.

The 1D example can be extended into two or three dimensions. Two-dimensional domains can be divided into triangular or quadrilateral elements. For a triangulation, both the basis functions and the approximation would then be piecewise linear functions that are linear on each triangle. In three dimensions tetrahedra and hexahedra are commonly used. The approximation in any dimension can be made more accurate by replacing the piecewise linear basis functions with piecewise quadratic or polynomial functions.

### 3. Matrix assembly

Similar to  $u_h$  (Eq. 1.10),  $w_h = \sum_{j=1}^N \beta_j h_j$  and we can simply choose  $w$  to be a basis function  $h_i$ . Substituting the latter and Equation 1.10 into 1.9, produces

$$\sum_{j=1}^n \alpha_j \int_{\Omega} \nabla h_j \cdot \nabla h_i \, d\mathbf{x} = \int_{\Omega} f(\mathbf{x}) h_i(\mathbf{x}) \, d\mathbf{x}. \quad (1.11)$$

If we now set

$$\begin{aligned} M_{ij} &= \int_{\Omega} \nabla h_j \cdot \nabla h_i \, d\mathbf{x} \\ f_j &= \int_{\Omega} f(\mathbf{x}) h_j(\mathbf{x}) \, d\mathbf{x} \end{aligned} \quad (1.12)$$

then Equation 1.11 can be written in the form of a matrix equation:

$$\begin{bmatrix} M_{11} & \cdots & M_{1n} \\ \vdots & \ddots & \vdots \\ M_{n1} & \cdots & M_{nn} \end{bmatrix} \begin{bmatrix} \alpha_1 \\ \vdots \\ \alpha_n \end{bmatrix} = \begin{bmatrix} f_1 \\ \vdots \\ f_n \end{bmatrix}, \text{ or} \quad (1.13)$$

$$\mathbf{M}\boldsymbol{\alpha} = \mathbf{f}.$$

The matrix  $\mathbf{M}$  is called the stiffness matrix and the vector  $\mathbf{f}$  the load vector. This linear system of equations can now be solved. If the matrix is sufficiently small, matrix inversion can be used. For a large system, the equation has to be solved iteratively. The latter process can be quite fast as  $\mathbf{M}$  is a sparse matrix, i.e. most  $M_{ij}$  are equal to 0.

## 1.3 Simulating tDCS

---

Volume conduction models of tDCS have been used to investigate the electric fields induced in the brain in an attempt to better understand the technique and its workings, and later to improve its application and effects. From spherical analytical descriptions, tDCS models have progressed into highly realistic representations of the human head.

### 1.3.1 Spherical models

In 1968, the first models of transcranial electric stimulation (TES) were published. Rush & Driscoll<sup>[137]</sup> constructed a mathematical model of three concentric spheres with different conductivities that represented the brain, skull and scalp of a human head (from here on denoted as RD model). This three-sphere model seemed a reasonably good fit to the geometry of the head (Fig. 1.6a). In such a spherical model with point electrodes, Laplace's equation (Eq. 1.5) can be solved analytically for Neumann boundary conditions. The electric potential within the spheres resulting from two point electrodes on the outer surface can be expressed by Legendre polynomials. Rush & Driscoll<sup>[137]</sup> evaluated the validity of their model using a model of a different kind: an electrolytic tank in the shape of a head with a half human skull submerged in conductive fluid. Electrodes attached above the centers of the frontal and occipital bones produced a rather uniform electric field in the homogeneous tank model (Fig. 1.6b) and in the mathematical model<sup>[137]</sup>. Agreement between the two models was good in areas where the skull thickness was comparable (Fig. 1.6c). One of the most important findings from these models was that only 45% of the applied current passed through the cranial cavity. The mathematical RD model became the basis for future spherical models of brain stimulation.

Having an analytical solution, a spherical model allows for validation of numerical approximation techniques. Spherical models with point-shaped sources of stimulation, as the RD model, have been used to model various techniques like TES and electrical impedance tomography (EIT)<sup>a</sup> and are also used for the forward calculations in electroencephalography (EEG) and magnetoencephalography (MEG) source localization. Within the contexts of EEG<sup>[154]</sup> and EIT<sup>[8]</sup> the FE method was shown to have good agreement with an analytical multi-sphere model.

It was only after the new rise of interest in tDCS had started in 2000 (Section

---

<sup>a</sup>EIT is a medical imaging technique that measures the potential on the perimeter of the head or torso to reconstruct an image of the impedance of the internal tissues.

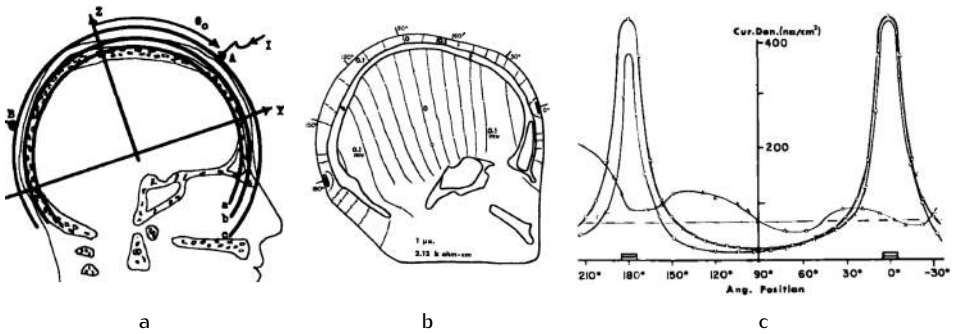


**Figure 1.6** The first models of transcranial electric stimulation constructed by Rush & Driscoll<sup>[137]</sup>. a) Fit of a three-sphere mathematical model to a sketch of a human head. b) Measured equipotential lines in the midsagittal plane of a tank model consisting of conductive fluid and a human skull. c) Comparison of the two methods, showing current densities for the theoretical (lower line in left half of figure) and tank models, at different angles from the stimulation electrodes. The skull thickness in the tank model (curved line) and spherical model (horizontal line) are indicated as well. These figures were reproduced with permission from the publisher.

1.1.3) that explicit models of tDCS were investigated. Miranda et al.<sup>[98]</sup> were the first to construct an FE model of tDCS by applying large rectangular electrodes patched to the RD model. While in experimental studies a homogeneous skin current density underneath the electrodes had always been assumed, this simulation showed that the current almost exclusively enters the skin around the perimeter of the electrodes (Fig. 2.2a).

The RD model was soon adapted into a four-sphere model to incorporate the highly conductive cerebrospinal fluid (CSF), which resulted in substantial shunting of the current<sup>[34,41]</sup>. These models were used to vary the parameters of stimulation: investigators tested small EEG-like electrodes<sup>[42]</sup> and concentric ring configurations<sup>[34]</sup> that resulted in improved focality, and studied the effects of changing the interelectrode distance<sup>[41]</sup>. A spherical model based on the RD model was used for the investigations in Chapter 2 of this thesis.

### 1.3.2 Realistic head models

As interest in tDCS has grown over recent years, so has the effort in simulating tDCS computationally. To achieve the highest amount of accuracy, a volume conduction model must incorporate a detailed description of the geometry of the structures in the head and realistic conductivity properties of each tissue. An important step in volume conduction modeling was the introduction of MRI-derived head models.

As the quality of MR images and the performance of computers increased, models included more different tissue types, a higher level of detail in geometry and realistic representations of anisotropically conducting tissues.

### Construction of a realistic FE head model

The creation of an MRI-derived head model starts with segmenting an MR image (Fig. 1.6a) into different tissue types by assigning a tissue index to each voxel (Fig. 1.6b). This can be done via automatic segmentation algorithms using gray-level thresholding and region-growing approaches. These segmentations should then be manually corrected slice by slice. A hexahedral model can be created directly from the segmentation by converting each voxel into a cubic element. More steps are required for a model with tetrahedral elements.

In order to construct a tetrahedral model, each segmented tissue compartment is first converted into a triangular surface mesh (Fig. 1.6c). Because the surface meshes need to be fully closed, the previous segmentation step has to be performed more carefully in order to prevent unconnected voxels. The triangular surface meshes can then be combined into one tetrahedral mesh with variable element sizes (Fig. 1.6d). The size of the elements in each compartment is determined by the resolution of the surface meshes and restrictions given to the meshing algorithm. Finally, each tetrahedral compartment is assigned a tissue index.

Obviously hexahedral models with one element per voxel are easier to construct than tetrahedral models. However, the former are computationally more demanding due to the high number of elements that follows from the small element size (typically  $1 \text{ mm}^2$ ). Also, the surfaces of tetrahedral models are more realistic. The blocky structure of hexahedral meshes can be corrected by shifting nodes on material interfaces, producing a so-called geometry-adapted hexahedral mesh. Such a mesh was used for the investigations in Chapter 3 of this thesis, where its construction process will be described in detail. Chapter 4 describes the creation of a tetrahedral head model that was used for the studies in Chapters 4 and 5. For both model types, the final step consists of converting the tissue indices into appropriate conductivity values.

### Tissue conductivity

In brain tissue, the conductivity along the neuronal fiber direction is much higher than in the direction perpendicular to the fibers. As a result, current tends to flow along the neuronal fibers. This directionally dependent behavior can be reconstructed by modeling brain tissue with anisotropic conductivity tensors. It has

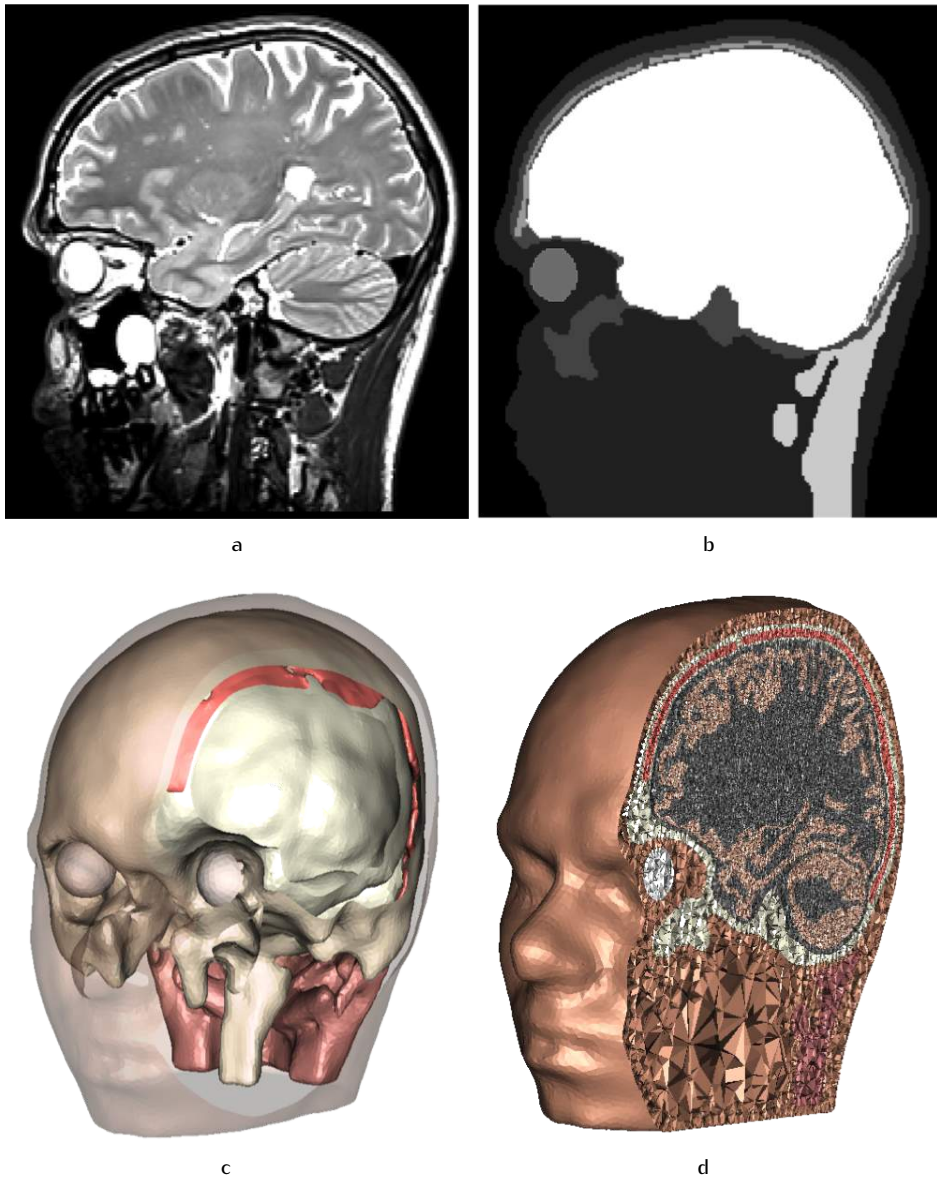


**Figure 1.7** Creation of a tetrahedral finite element volume conduction model. An MR image (a) is segmented into tissue types by assigning an index to each voxel (b). The segmentation is then converted into triangular surface meshes (c), which are finally combined into one tetrahedral mesh with tissue indices for each compartment (d). The brain compartments (GM and WM) are not segmented in these images, because they were added to this model separately. The creation process of this model is described in detail in Section 4.2.



been shown that, primarily in the WM, currents in the model will follow known fiber paths<sup>[149]</sup>. Basser et al.<sup>[11]</sup> and Tuch et al.<sup>[155]</sup> introduced the assumption that conductivity tensors share eigenvectors with diffusion tensors and can therefore be derived from diffusion tensor MR imaging (DTI). Positive validations of this model have been reported<sup>[155,110]</sup> and it has become a conventional method to incorporate brain anisotropy into volume conduction models<sup>[163,31,32]</sup>. However, many models do not include anisotropy at all.

### Realistic volume conduction models for tDCS

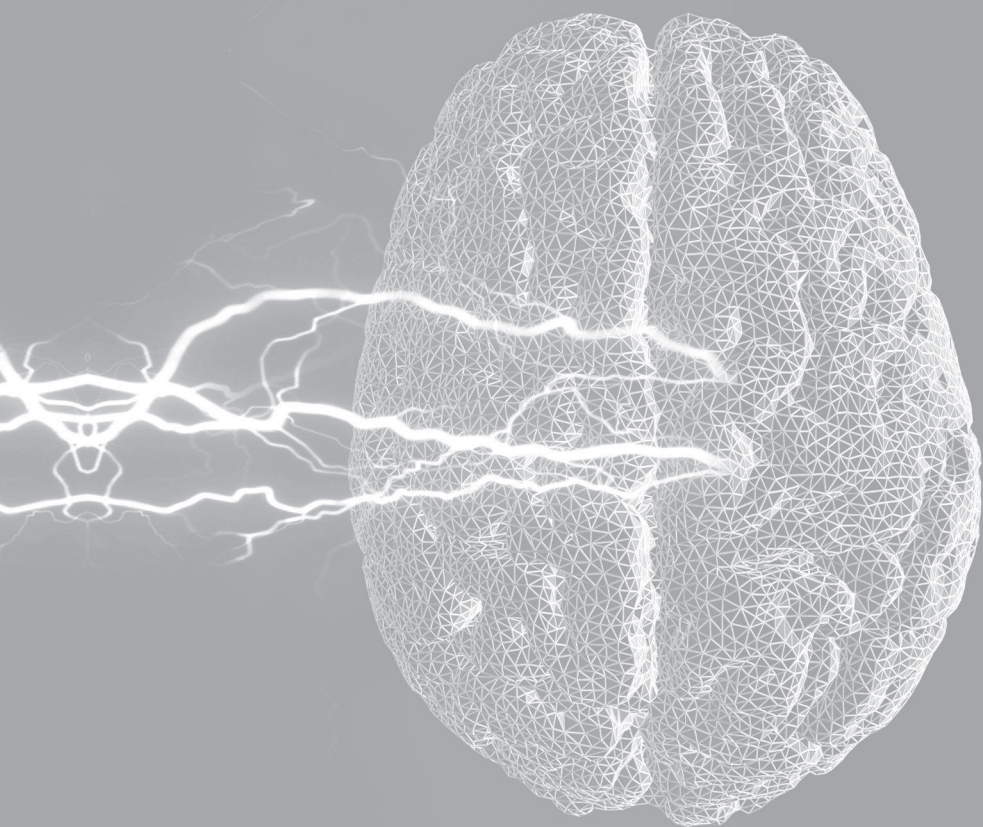
Wagner et al.<sup>[160]</sup> presented the first simulations of tDCS using a head-shaped model. This FE model included skin, skull, CSF, gray matter (GM) and white matter (WM) compartments. Although the geometry was derived from MR images, the overall level of detail was low and the brain compartments did not have gyri and sulci. Nevertheless, this study showed the future potential for brain stimulation models, examining a multitude of configurations and the effects of brain lesions.

Due to recent advances in computational capabilities and improved imaging and modeling methods, the possibilities for creating tDCS volume conduction models have grown enormously. In finite element models, the level of geometric detail can be increased by decreasing the size, and concurrently increasing the number, of the elements constituting a model. Currently, models exist that consist of several million elements of either tetrahedral<sup>[33,142,163]</sup> or hexahedral shape<sup>[113,141]</sup>. The small element size allows for these models to have realistically shaped gyri and sulci and some models even include small structures like eyes and blood vessels<sup>[113,141]</sup>. In a few studies, the three different layers of the skull, due to its low conductivity the most important barrier to the tDCS currents, were modeled explicitly<sup>[64]</sup> or by means of an anisotropic approximation<sup>[149]</sup>. The most recent improvement came when investigators started to incorporate realistic fiber directions based on DTI into their models, for white matter alone<sup>[111,149,145]</sup> or for both gray and white matter<sup>[163]</sup>. While many important aspects of tDCS volume conduction have been modeled in detail, no study yet has incorporated all these features into one model. Furthermore, while tDCS simulation studies are now abundant, experimental validation studies are scarce.

### 1.3.3 Models in this thesis

This thesis presents a model that does include all the features mentioned above, providing the currently most accurate predictions for tDCS. The detailed description of the creation process also supplies a framework for creating similar high-quality

models almost exclusively using freely available software (Chapter 4). This realistic model was used to simulate the electric fields induced with the conventional configurations for the five most commonly targeted brain areas (Chapter 4). Subsequently the electrode positions were optimized for each target area using this model (Chapter 5) and the optimizations were validated through measurements of corticospinal excitability using TMS and EMG (Chapter 6). But first, two studies will be presented that investigate the importance of increasing the detail and realism of tDCS volume conduction models (Chapters 2 and 3). The modeling results in this thesis might also be applied for different electrical stimulation techniques such as tACS, tRNS, TES and ECT.







## 2.1 Introduction

Calculating current distributions arising from tDCS gives insight into the potential effects DC stimulation may have on the brain. Models of tDCS can be used to investigate optimal electrode properties and locations for stimulating specific brain areas, but also for creating safety guidelines. To optimize the modeling of tDCS, it is important to identify the best approach to approximate the skull's anisotropic properties.

The relatively poorly conducting human skull poses a substantial barrier to the currents of tDCS. Using an electrolytic tank model<sup>a[137]</sup> and a spherical volume conduction model of transcranial stimulation<sup>[98]</sup> it was shown that a considerable amount of the injected current does not reach the brain compartment. The low skull conductivity also causes the injected current to spread, reducing its focality. This suggests that modeling the human skull accurately is an important step in improving simulations of tDCS.

A large part of the human cranial bone consists of two layers of compact tissue (compacta) enclosing one layer of cancellate bone (spongiosa). This layered structure can be visualized on an MR image of a human head (Fig. 1.7a). The higher conductivity of the internal spongiosa causes the skull to be more conductive in the tangential than the radial direction. In tDCS modeling, these properties have either been disregarded by modeling the skull as a single isotropic compartment<sup>[98,33,67,97,140,160]</sup> or approximated by incorporating the skull as an anisotropic layer<sup>[111,148]</sup>.

The latter studies showed that including tissue anisotropy in tDCS models may have significant consequences on the results. One would expect a model that is even closer to the actual anatomy, i.e. with three separate skull layers, to further improve the accuracy of tDCS modeling. This approach has improved current density calculations in a two-dimensional TES model<sup>[64]</sup> and source localization estimations in EEG and MEG studies<sup>[120,128,129]</sup> using point sources. The effect of layered skull on three-dimensional tDCS simulations has remained unknown.

This chapter describes simulations of tDCS with a model in which the skull is represented by three isotropic layers. The three-layer reference model is then compared with the commonly used isotropic and anisotropic skull approximations for a range of conductivities. To isolate the effects of different skull modeling techniques, the most simple model is used in the form of a spherical three-compartment volume conductor. Results will show that an isotropic representation of the skull is permitted if the optimal conductivity values are used.

<sup>a</sup>See Section 1.3.1.

## 2.2 Methods

---

The geometry of the spherical head model introduced by Rush & Driscoll<sup>[137]<sup>a</sup></sup> was used as the basis for four models of which only the conductive properties of the skull compartment were different. Two sets of simulations were performed with these models to investigate the effects of the approximation approaches for different conductivities and find the most appropriate values.

### 2.2.1 Model setup

The head model consisted of three concentric spheres with radii of 80, 85 and 92 mm representing brain, skull and skin, respectively. The tDCS electrodes were modeled as square patches with a surface area of 35 cm<sup>2</sup> and a thickness of 1 mm. Two such electrodes were placed on the outer sphere in three configurations: the electrodes were either 180, 90 or 45 degrees apart. When one imagines a reference electrode on the forehead, these geometries approach stimulation of e.g. cerebellum, visual cortex and motor cortex, respectively. The electrodes were given the conductivity of saline (1.4 S/m); 0.333 and 0.435 S/m were chosen for brain and skin conductivity, respectively<sup>[61]</sup>. Custom software was used to create the surfaces of the described geometry and the result was meshed with TetGen<sup>b</sup>, yielding a mesh of over  $5 * 10^5$  nodes and  $3 * 10^6$  tetrahedrons, with an average scaled Jacobian mesh quality of 0.48.

#### Reference model

In order to match the real skull's properties as closely as possible, the 5 mm thick skull layer was divided into three layers representing the lower compacta, spongiosa and upper compacta. Akhtari et al.<sup>[1]</sup> measured thicknesses and conductivities of the three layers of live human calvarian bone. The averages of the thicknesses they reported were used to scale the three skull layers in the Reference model, resulting in 1.2, 2.3 and 1.5 mm thickness from outmost to innermost layer. The conductivity values used for compacta and spongiosa are provided later on for each set of simulations.

---

<sup>a</sup>See Section 1.3.1 and Fig. 1.6a.

<sup>b</sup><http://tetgen.belios.de>.

### Anisotropic model

The skull in the Reference model was first approximated by a single anisotropic layer. The resulting model will be referred to as *Aniso*. Each element belonging to the skull compartment was given its own anisotropic conductivity tensor, of which the radial and tangential components are equal for all elements.

In order to determine the equivalent radial and tangential conductivities of a single anisotropic skull layer that should represent the actual three-layered skull, we will consider a rectangular piece of three-layered skull as an isolated block. This block, schematized in Fig. 2.1, consists of three isotropic layers, with  $\sigma_i$  the conductivities of the layers and  $h_i$  the heights, for  $i = c, s$  ( $c$  for compacta,  $s$  for spongiosa). If we now imagine a uniform current flowing through this conductor in either the radial ( $I_r$ ) or tangential ( $I_t$ ) direction, we can calculate the equivalent radial ( $\sigma_r$ ) and tangential ( $\sigma_t$ ) conductivities for the block as a whole in either situation:

$$\begin{aligned} \frac{1}{\sigma_r} &= \frac{\lambda_c}{\sigma_c} + \frac{\lambda_s}{\sigma_s} \text{ and} \\ \sigma_t &= \lambda_c \sigma_c + \lambda_s \sigma_s, \end{aligned} \quad (2.1)$$

where  $\lambda_i = h_i/(h_c + h_s)$ . We will term this pair of  $\sigma_r$  and  $\sigma_t$  values the *equivalent* anisotropic conductivity values for the spherical model. They are truly equivalent to the three-layer situation for a uniform current density in an isolated block. Combined these values serve as a set of eigenvalues from which the diagonal tensor  $\mathbf{D} = \text{diag}(\sigma_r, \sigma_t, \sigma_t)$  can be constructed. For each tetrahedral skull element,  $\mathbf{D}$  is rotated such that its radial component is directed along the normal to the surface, providing an anisotropic conductivity tensor for each element.

### Isotropic models

Another common method to model the skull is as a single isotropic layer. Two different isotropic approximation models were created, distinguished by a different rationale for choosing the conductivity.

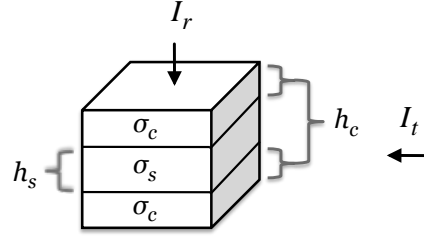
In the first model, labeled *IsoB*, the skull compartment was given a conductivity equal to the bulk conductivity of three-layered skull. This bulk skull conductivity  $\sigma_b$  was calculated via the volume constraint<sup>[164]</sup>:

$$\frac{4}{3}\pi\sigma_r\sigma_t^2 = \frac{4}{3}\pi\sigma_b^3, \quad (2.2)$$

which provides the bulk conductivity of an anisotropic layer. Averages of the spongiosa and compacta conductivities found by Akhtari et al.<sup>[1]</sup>:  $\sigma_c = 7$  mS/m and  $\sigma_s = 25$  mS/m, were inserted into Eq. 2.1 together with the  $h_i$  from the Reference model



**Figure 2.1** Schematic approximation of a piece of human skull as a block consisting of three layers with each its own conductivity  $\sigma$  and height  $h$ . The subscripts  $c, s$  represent the compact and spongy layers, respectively. Current flows through the skull either radially ( $I_r$ ) or tangentially ( $I_t$ ).



and the result was combined with Eq. 2.2. This resulted in a bulk skull conductivity  $\sigma_b = 13.5 \text{ mS/m}$ .

In tDCS, one might expect the current flowing between the electrodes to cross the skull predominantly radially. To simulate this behavior the *IsoR* model was created. The conductivity of its skull compartment was set equal to the equivalent radial conductivity ( $\sigma_r$ ) of the Reference model.

## 2.2.2 Computations

The FEM solving package SCIRun 4.0<sup>a</sup> was used to solve the Laplace equation (Eq. 1.5) on a finite element mesh with Neumann boundary conditions at the skin surface and Dirichlet boundary conditions on the outer surfaces of the electrodes (Eq. 1.6). The potential difference impressed on the two electrodes was chosen such that the total current flow between the electrodes was 1 mA.

### Analysis

The effectiveness of transcranial direct current stimulation is believed to be related to the current density in the targeted brain area<sup>[108]</sup>. The current density in each element was therefore calculated from the estimated potentials at the nodes using  $\vec{J} = -\sigma \vec{\nabla} \phi$  (Section 1.2.1).

The total current entering a compartment was calculated via a summation over the triangular faces of its surface:  $I = \sum_{\ell} \vec{J}_{\ell} \cdot \vec{A}_{\ell}$ , where  $\vec{A}_{\ell}$  is a vector directed along the outward normal of face  $\ell$  with a size equal to the area of face  $\ell$ . The summation runs over all faces for which the product in the summation is negative (i.e. current enters the sphere).

For each model the values of the current density norm  $|\vec{J}|$  for all  $m$  elements of the brain compartment were gathered into a vector  $\mathbf{J}$ . The results of the Reference model ( $\hat{\mathbf{J}}$ ) were compared to the results of each approximation model ( $\mathbf{J}$ ) via the

<sup>a</sup>Scientific Computing and Imaging Institute, Salt Lake City, UT, USA.

relative difference measure<sup>[93]</sup>

$$\text{RDM} = \sqrt{\sum_{k=1}^m \left( \frac{\hat{J}_k}{\hat{J}} - \frac{J_k}{J} \right)^2} \quad (2.3)$$

and the relative magnification factor<sup>[57,93]</sup>

$$\text{MAG} = \left| 1 - \sqrt{\frac{J}{\hat{J}}} \right|. \quad (2.4)$$

The RDM is a measure of the pattern of the errors and the MAG a measure of the size.

### Simulation 1

An important factor in the conductive properties of three-layered skull is the ratio between the conductivities of the compact and spongy layers:

$$\gamma \equiv \frac{\sigma_s}{\sigma_c}. \quad (2.5)$$

The set  $\gamma = \{1, 2, 3, \dots, 20\}$  encloses the minimum and maximum conductivity ratios calculated from the measurements of Akhtari et al.<sup>[1]</sup> By combining these  $\gamma$  values with Equations 2.1, 2.2 and 2.5 with  $\sigma_b = 13.5$  mS/m as a constraint, each  $\gamma$  yields a pair of conductivity values  $\{\sigma_s, \sigma_c\}$  for the Reference model, and a pair of conductivity values  $\{\sigma_r, \sigma_t\}$  for the anisotropic model, such that the equivalent anisotropy and the bulk skull conductivity for the two pairs are equal. Thus, for each  $\gamma$  value, a set of two models (three-layered and anisotropic) with equivalent conductive properties was constructed. For the IsoR model:  $\sigma_{\text{skull}} = \sigma_r(\gamma)$  with for each  $\gamma$  the corresponding  $\sigma_r$  from the Aniso model. As  $\sigma_b$  was kept constant, there was only one conductivity value for IsoB:  $\sigma_{\text{skull}} = \sigma_b$ . Note that for  $\gamma = 1$  all four models are equal. The RDM and MAG differences between the current densities in the Reference model and those in the approximation models were calculated for each model and each  $\gamma$  separately.

### Simulation 2

In simulation 1 the Reference model was approximated by choosing equivalent conductivity values. It is conceivable that choosing the parameters differently actually yields better approximations. Simulation 2 investigated whether this is the case.

For the Reference model,  $\gamma = 10$  was chosen, as this is the median of the range used for Simulation 1. For each approximation model a range of conductivities around

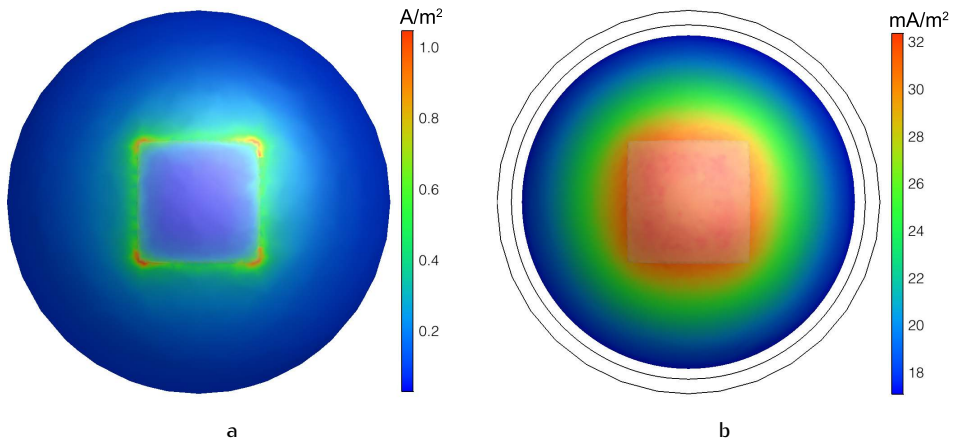


**Figure 2.2** Current density magnitude on the surfaces of the a) skin and b) brain compartments of the Reference model ( $\gamma = 20$ ) with the anode and cathode 180 degrees apart. The view is towards the anode. In the right figure, the anode is transparent and the black lines indicate the perimeters of the skull and skin compartments.

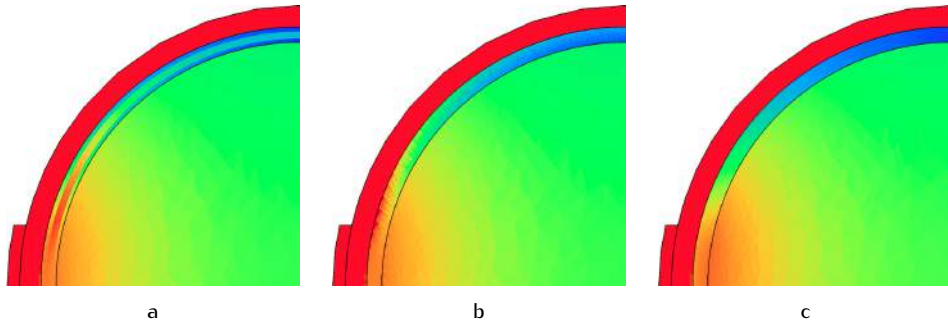


**Figure 2.3** Current density on a plane through the center of the a) Reference, b) Aniso and c) IsoR models. To show the different nature of the models more clearly,  $\gamma = 40$  was used for these plots. Current density in all images is on the same arbitrary scale, which was optimized for the skull; hence skin current density variations are not visible.

the values corresponding to  $\gamma = 10$  were selected. The single-layer isotropic model (here IsoR and IsoB are one model) was solved for a collection of conductivities  $\sigma_{\text{skull}} = \{1, 2, \dots, 20\}$  mS/m. For the Aniso model  $\sigma_r$  values were chosen within the range  $\sigma_r = \{4 : 14\}$  mS/m, based on the measurements by Akhtari et al.<sup>[1]</sup>, and combined with  $\sigma_t = \{14 : 22\}$  mS/m, such that for each pair  $\{\sigma_r, \sigma_t\}$  the ratio  $\gamma$  in an equivalent three-layered model falls within the range  $\gamma = \{1 : 20\}$ . For both approximation models the results for each (pair of) conductivity value(s) were compared to the results of the Reference model with  $\gamma = 10$  via the RDM and MAG measures.

## 2.3 Results

The results of Simulations 1 and 2 are first presented for the configuration with a 180-degree interelectrode angle. The effect of changing the electrode locations is described separately.

### Simulation 1

In order to compare this work to previous studies, first the current density distribution on the skin surface of the Reference model is discussed (Fig. 2.2a). For these plots  $\gamma = 20$  was chosen, as it shows the distributions most clearly and distributions were similar for all  $\gamma$ . The current density is highest on the perimeter of the electrode with peaks at its corners. On the surface of the brain compartment (Fig. 2.2b), the current density spreads more evenly with a large area of near-maximal current density under the electrode. Towards the center of the volume conductor the current is distributed more widely. This effect is stronger with increasing values of  $\gamma$ .

Figure 2.3 shows current densities on a cross-section of the volume conductor to visualize the effects of different skull modeling approaches on the current densities in the skull. In the Reference model (Fig. 2.3a), a significant amount of current is shunted through the highly conductive spongiosa layer. In the Aniso model's skull compartment (Fig. 2.3b), current flows primarily tangentially in the more superficial part of the skull. This is due to the skull's relatively high tangential conductivity in this model. Towards the brain compartment, the current density in the skull decreases. Here, the current is drawn towards the brain, because the conductivity of the brain is much higher than that of the skull. The isotropic approximation (Fig. 2.3c) results in an even spread of current density in the skull compartment.

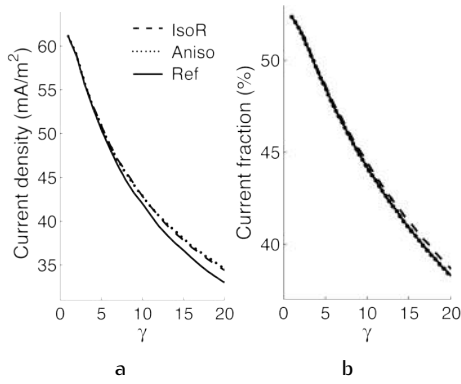


**Figure 2.4** Maximal current density in the brain compartment (a) and fraction of the injected current that enters the brain compartment (b). For the IsoB model the results at  $\gamma = 1$  apply.

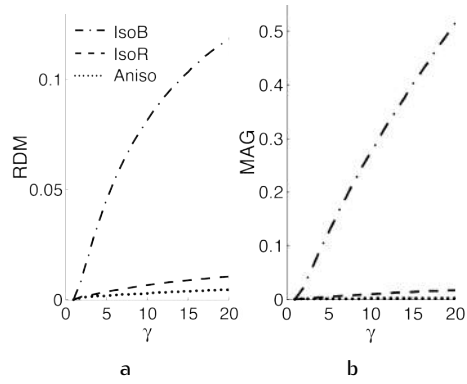


**Figure 2.5** Average current density errors in the brain compartment quantified by a) RDM and b) MAG differences between each approximation model and the Reference model.

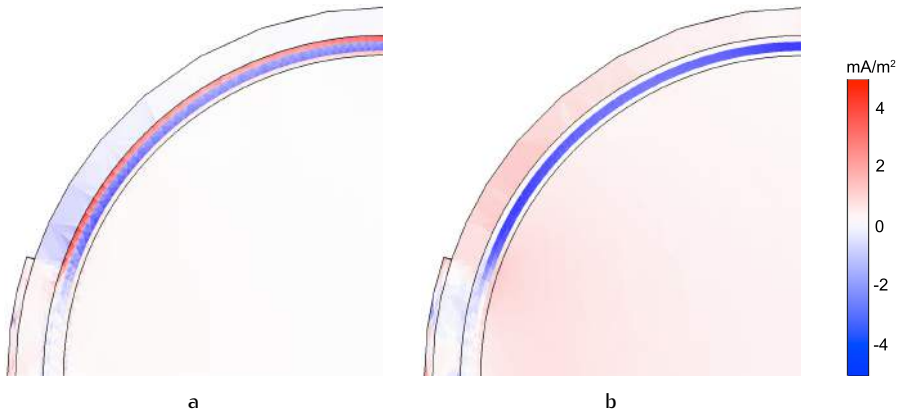


**Figure 2.6** Difference in current densities between the a) Aniso and b) IsoR models and the Reference model ( $\gamma = 20$ ), shown on a plane through the center of the model.

For each model, the maximum current density in the brain compartment decreases as  $\gamma$  increases (Fig. 2.4a), showing that the current spreads out more when the skull is less homogeneous. This is confirmed by the result that also the fraction of injected current that enters the brain compartment ( $I_{\text{brain}}/I_{\text{skin}}$ ) decreases with increasing  $\gamma$  (Fig. 2.4b). Since the bulk skull conductivity was kept constant, increasing  $\gamma$  corresponds to concurrently decreasing  $\sigma_c$  and increasing  $\sigma_s$ . Thus more current is shunted through the skin and spongiosa compartments, leading to less current entering the brain and a lower current density maximum. In the Reference model with  $\gamma = 20$ , 38% of the injected current entered the brain (Fig. 2.4b), confirming that the skull forms a substantial barrier to the current. For both current density measures, the Aniso and IsoR models deviate less than 3% from the Reference (Fig. 2.4).

From the average current density errors in the brain compartment (Fig. 2.5) one observes that: 1) both RDM and MAG errors are higher for the IsoR than the Aniso model and are much higher for the IsoB model, the differences increasing with larger  $\gamma$ ; 2) for the Aniso model,  $\text{RDM} > \text{MAG}$  for all  $\gamma$ ; and 3) for both Iso models  $\text{RDM} < \text{MAG}$  (note the different scales). Combining these observations, it follows that the isotropic and anisotropic approximations deviate more from each other in MAG than in RDM error. This suggests that disregarding anisotropy affects more the magnitude of the error than its distribution.

The current densities in the Reference model were subtracted from the current densities in the Aniso and IsoR models to gain insight into the distribution of the errors resulting from the approximations (Fig. 2.6). In comparison to the Reference model, current density in the Aniso skull compartment is too high in both compacta regions and too low in the spongiosa region (Fig. 2.6a). At the location of the compacta layers, the Aniso model's equivalent isotropic conductivity is higher than the conductivity in the realistic situation ( $\sigma_b > \sigma_c$ ) and vice versa in the spongiosa layer ( $\sigma_b < \sigma_s$ ), which explains the error distribution in the skull, and also the underestimated skin current density. In the brain compartment the distribution of the errors is similar for the Aniso and IsoR models, whereas in the IsoR model the size of the errors is much higher (Fig. 2.6b). Compared to each other, the different skull modeling approaches lead to large discrepancies in the skin and skull, but only a scaling difference in the brain. For each model, the highest errors in the brain are located directly under the electrode, which conventionally is the target area of stimulation.

## Simulation 2

Inspecting the RDM errors in the Aniso model's brain compartment for each combination  $\{\sigma_r, \sigma_t\}$  with respect to the Reference model with  $\gamma = 10$  (Fig. 2.7a) shows

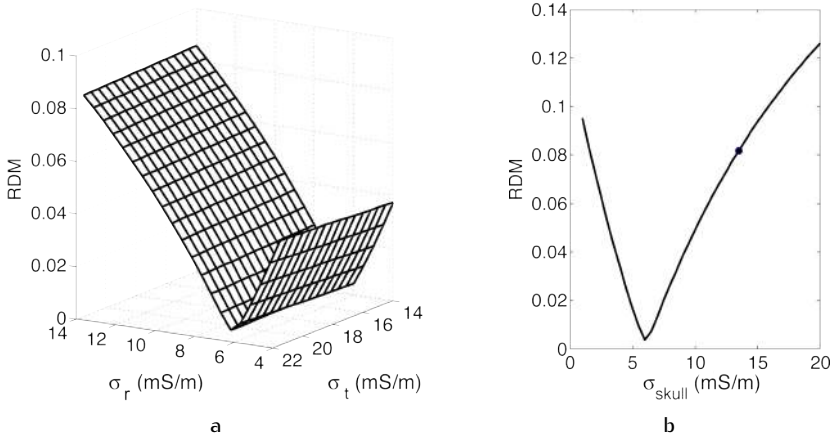


**Figure 2.7** RDM differences between brain current densities in the Reference model and the approximation models for a range of skull conductivities. The Reference model with  $\sigma_c$  and  $\sigma_s$  corresponding to  $\gamma = 10$  (equivalent to  $\sigma_r = 6.5$  mS/m and  $\sigma_t = 19.5$  mS/m in the Aniso model) was compared with a) the Aniso model for a grid of pairs  $\{\sigma_r, \sigma_t\}$  and b) the isotropic model for a range of isotropic conductivity values. The result for  $\sigma_{skull} = \sigma_b$  is indicated with a black dot.

that the value of  $\sigma_r$  has a large influence on the error, whereas the value of  $\sigma_t$  has almost no effect. The minimum RDM of 0.0031 is reached for  $\sigma_r = 6.5$  mS/m. This value is equal to the equivalent radial conductivity of the Reference model as calculated via Eq. 2.1.

The RDM differences between the Reference model with  $\gamma = 10$  and the isotropic one-layer model (Fig. 2.7b) show that the bulk skull conductivity as calculated via Eq. 2.2 (black dot in Fig. 2.7b) is not the optimal value for approximating the skull. The plot has a minimum RDM of 0.0037 at  $\sigma_{skull} = 6$  mS/m, which corresponds closely to the equivalent radial conductivity of the Reference model.

For both the anisotropic and isotropic models, the optimal values are the equivalent values, i.e. the values used in Simulation 1 for the Aniso ( $\sigma_r, \sigma_t$ ) and IsoR ( $\sigma_r$ ) models. Overall, Simulation 2 shows that, independent of the modeling approach,  $\sigma_r$  is by far the dominant factor in determining the conductive properties of the skull and its value should be equal to the equivalent radial conductivity of a three-layer skull model. When modeling with these optimal values, the deviation from the ideal model is small for both methods. Analogous plots presenting the MAG errors (not shown) displayed identical dependencies.

### Electrode configurations

The analyses described above were also performed for models with the electrodes distanced by either 45 or 90 degrees. Comparing current density distributions on the surfaces of the Reference model with a 45-degree (Fig. 2.9) and a 180-degree interelectrode angle (Fig. 2.2) demonstrates that smaller interelectrode angles lead to a shift in the current density distribution with the maxima moving from under the electrodes to centrally in between them. Differences in current density between the approximation models and the Reference arise mainly in the skin and skull compartments in the area between the electrodes (Fig. 2.9). The error distributions are similar to those for the model with a 180-degree interelectrode angle (Fig. 2.6), but errors are approximately ten times bigger for the 45-degree model. For all three geometries the relationship between  $\gamma$  and either the current density maximum, current fraction or average discrepancies (RDM and MAG) was similar. Decreasing the interelectrode distance resulted in a progressive increase in maximum current density within the brain, a decrease in the current fraction that entered the brain and an increase in the average errors.

## 2.4 Discussion

To examine the validity of the methods used in this study, the current density distributions are compared to previous similar work. Miranda et al.<sup>[98]</sup> modeled tDCS with the same head geometry as in this chapter. Using  $\sigma_{\text{skull}} = 6 \text{ mS/m}$  and a 2 mA current, they found a maximum current density in the brain of  $0.145 \text{ A/m}^2$ . The isotropic IsoR model with  $\sigma_{\text{skull}} = 6.1 \text{ mS/m}$ , a 90 degree interelectrode angle and a 2 mA current is the most similar to their approach and resulted in a maximum brain current density of  $0.091 \text{ A/m}^2$ . Considering electrode sizes and conductivities were slightly different, this is in good agreement. Also the distribution of skin current density (Fig. 2.2) and the shift in current density maximum for smaller interelectrode angles (Fig. 2.8) are in agreement with previous studies<sup>[98,97,160,41]</sup>.

According to the models here presented, current flows into the scalp at the perimeter of the anode. The low conductivity of the skull smoothens this pattern into a more homogeneous distribution. Approximating the skull by a single layer resulted in distorted current density distributions within the skin and skull compartments, but in the brain compartment the deviation was mostly reduced to a scaling error. In the brain compartment, differences in current density maximum, penetrating current fraction, and average error with respect to the Reference, were small for both the



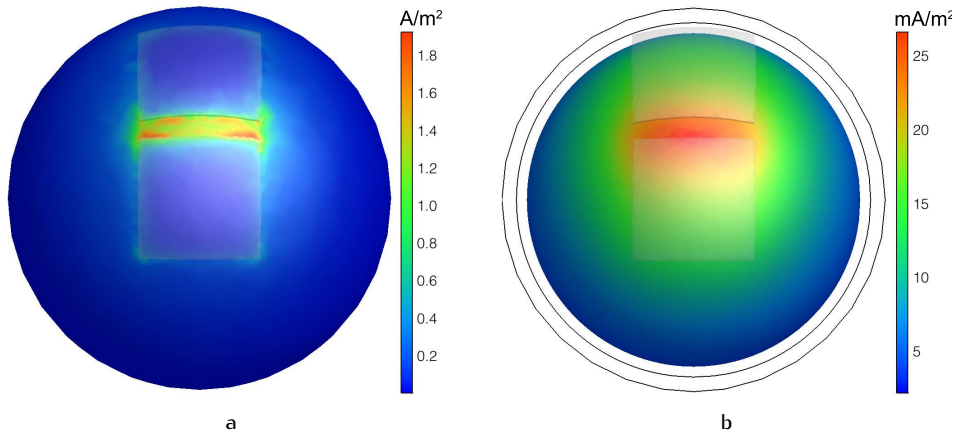


**Figure 2.8** Current density magnitude on the surfaces of the a) skin and b) brain compartments of the Reference model ( $\gamma = 20$ ) with the anode and cathode 45 degrees apart. The view is towards the anode. In the right figure, the anode is transparent and the black lines indicate the perimeters of the skull and skin compartments. This plot is analogous to Fig. 2.2 for the model with a 180-degree interelectrode angle.

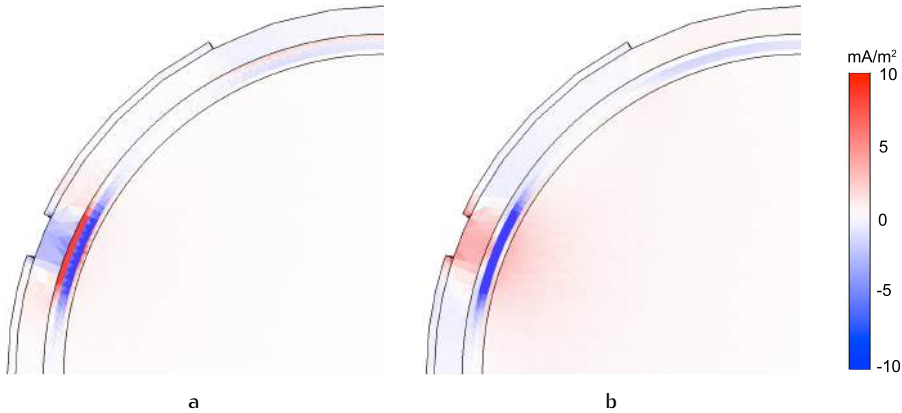


**Figure 2.9** Difference in current densities between the a) Aniso and b) IsoR models and the Reference model ( $\gamma = 20$ ), shown on a plane through the center of the model, for the geometry with a 45-degree angle between the electrodes. This plot is analogous to Fig. 2.6 for the model with a 180-degree interelectrode angle.

Aniso and IsoR models, when the equivalent anisotropic and isotropic conductivities were used. Using values other than the equivalent ones lead to large errors. Thus, when, and only when, using the *equivalent* (as defined in this chapter, p. 29) anisotropic ( $\sigma_r, \sigma_t$ ) and isotropic conductivity ( $\sigma_r$ ) values for the respective approximation models, both models perform well and could be used to model the skull. It should be noted though, that this only holds for the brain compartment. If one wishes to study tDCS-generated current densities in the scalp, for example to examine concurrent scalp muscle stimulation, single-layer approximation models should not be used.

The skull conductivities used in this study were based on a paper by Akhtari et al.<sup>[1]</sup>. At present, this is the only report of compacta and spongiosa conductivity measurements in live human skull. It presented measurements of just four subjects and the results showed a significant variance. Therefore simulations were performed here for multiple conductivity ratios surrounding the reported values. The results were consistent over this range. While there is still much debate on the conductivity value and anisotropy ratio of human skull, the current study's conclusions seem valid for all realistic conductivity values.

The IsoR model, in which the skull conductivity was equal to the radial conductivity of the anisotropic skull, performed well in approximating the three-layered skull. This suggests that the radial conductivity determines most of the conductive properties of the skull, which was confirmed by the second simulation. A dominance of the radial conductivity of the skull was also found in EEG source localization studies<sup>[31,90,157]</sup>. In this chapter it was found that neglecting anisotropy primarily affects the magnification of the current density and less its pattern. A study investigating skull modeling approaches for transcranial electric stimulation also found that different methods mainly lead to changes in magnitude of brain current densities and not topography<sup>[64]</sup>.

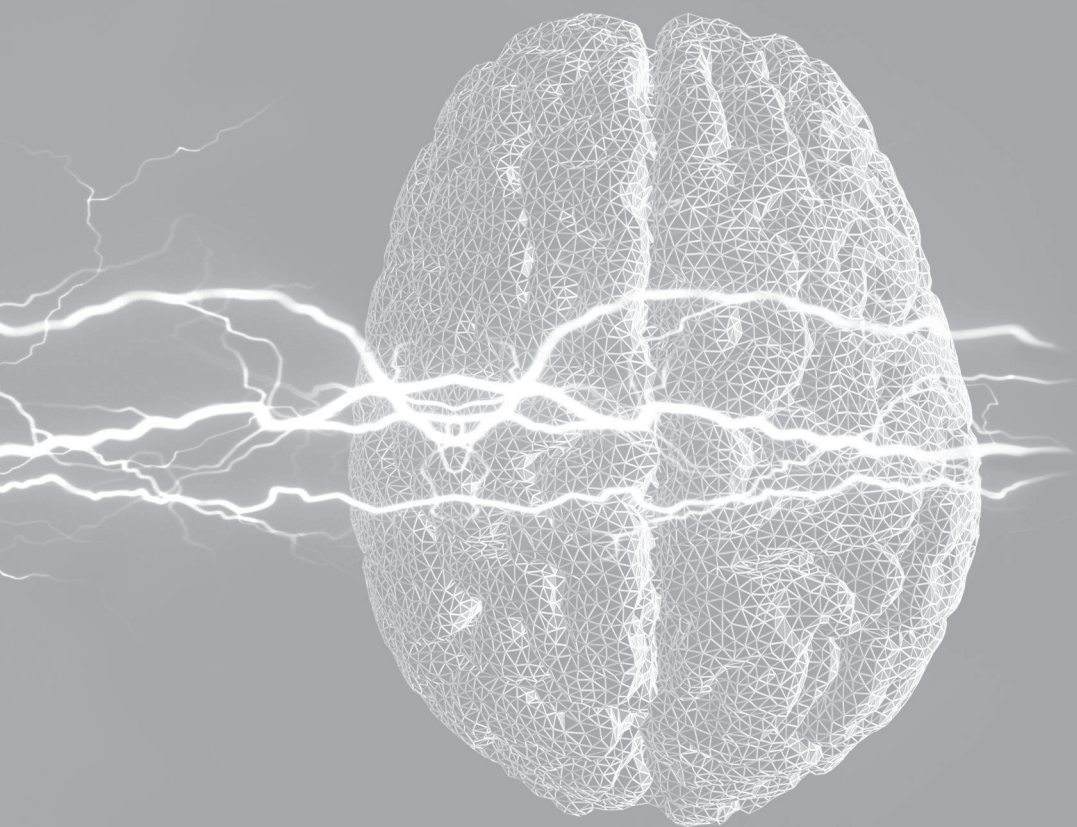
This study used a spherical approximation to a human head. In an EEG source localization study<sup>[90]</sup> it was found that skull anisotropy affects realistically-shaped head models more than spherical models. Other studies concluded that improper modeling of the skull's thickness<sup>[29]</sup>, curvature<sup>[160]</sup> or inhomogeneity<sup>[31]</sup> can lead to large errors in modeling results. Furthermore, the conductivity of the skull depends on the relative amounts of spongy and cancellate bone, a factor which varies throughout the skull, and on the presence of structures like sutures and canals<sup>[78]</sup>. The varying amount of spongiosa in the skull seems to strongly affect its radial conductivity<sup>[151]</sup>, a property which, as was shown here, accounts for the largest part of the skull's anisotropic properties. Because of the importance of these skull properties, appropriate skull modeling should be further investigated in a realistically shaped human head model.

## 2.5 Conclusions

---

In a spherical head model for tDCS, both anisotropic and isotropic one-layer approximations perform well in simulating the skull realistically and it is not necessary to model the three skull layers separately. When using either of these approximations, it is crucial to choose the radial conductivity as close as possible to that of the real skull.









## 3.1 Introduction

---

Over recent years, possibilities for creating realistic volume conduction models of tDCS have increased in both accuracy and efficiency. While the maximum level of detail that can be achieved has increased, the production of such a highly detailed model takes much time and effort. At the same time, the amount of time and effort required for making a basic model has decreased. Creating patient-specific models in order to predict personally optimized stimulation protocols is even becoming a reachable goal. Now the difficulty in creating such models lies in finding the balance between accuracy and fast production. Therefore it is necessary to know which aspects are crucial with respect to accuracy.

Increased realism and accuracy in tDCS modeling can be achieved by improving either the geometrical or conductivity representation of tissue compartments. Previous simulation studies have included a CSF compartment<sup>[160,142,32,113]</sup>, separate skull layers<sup>[64,132]</sup>, a white matter compartment<sup>[160,114,140,142]</sup> and/or WM conductivity anisotropy<sup>[64,111,148,141]</sup>. While each of these studies assisted in gaining insight into tDCS, none have evaluated and compared the effects of including all these model features. The investigations in this chapter start with a basic three-compartment head model, which is then extended step by step to an anisotropic six-compartment model by including each of the five features mentioned above. In this way, each effect can be interpreted individually, enabling a new level of understanding of tDCS volume conduction effects.

The current density distributions induced by tDCS will be investigated by studying high-resolution vector field visualizations and quantifications of field changes in both orientation and magnitude. Realistic predictions of tDCS are presented for two commonly targeted areas: the primary auditory and motor cortices. While simulations of M1 stimulation have been presented<sup>[33,68,142,163]</sup>, these studies did not investigate the direction of the field; simulations of auditory cortex stimulation have not been presented before. A novel type of finite element mesh is used that allows curved boundaries in a hexahedral model. The FE approach was specifically tailored to this geometry-adapted hexahedral mesh, resulting in significantly smaller errors<sup>[159]</sup>. Finally, employing a new nonlinear registration method for the MRI data sets<sup>[139]</sup> allows for the correction of susceptibility artifacts in the DTI data.

The study presented here thus combines aspects that have not been used together in tDCS simulations before. Furthermore, the step-by-step approach has resulted in a series of recommendations for efficient and yet accurate modeling of tDCS.



## 3.2 Methods

---

An MRI-based hexahedral head model was generated and the locations of auditory (A1) and motor (M1) cortices were determined. With this model, a series of tDCS simulations was performed with increasingly complex conductivity properties. The resulting current density distributions were finally compared between each consecutive modeling step.

### 3.2.1 Volume conduction model

MR images were made of a healthy 26-year-old male subject, who gave written informed consent. A realistic head model was built by converting the voxels of the MR scans into a hexahedral mesh, after which the geometry was adapted to better resemble smooth surfaces. Using the geometry of this model, six different models were made with different conductivity properties.

The tDCS FE implementation developed by<sup>[159]</sup> and for the first time presented in more detail in this study, not only has a resolution of over two million FE nodes, but also allows curved boundaries in a hexahedral model. Motivated by a similar approach for EEG source analysis<sup>[165]</sup>, an isoparametric FE approach (i.e. the finite element basis functions are not only used for potential approximation, but additionally for an improved description of the element contours) was developed for tDCS stimulation that is specifically tailored to geometry-adapted hexahedral meshes, resulting in significantly reduced numerical errors<sup>[159]</sup>.

While modeling multiple isotropic tissue compartments in realistic head models segmented from registered T1-weighted (T1w) and T2-weighted (T2w) MR images is becoming a more and more standardized procedure<sup>[163,31,32]</sup>, accurate modeling of WM conductivity anisotropy is still a challenging task. DTI data suffer from geometrical distortions and intensity modulations because of susceptibility artifacts which complicate its fusion with T1w or T2w datasets. Here a new nonlinear registration method was employed that uses a reversed gradient approach based on images acquired in positive and negative phase-encoding direction<sup>[139]</sup>. In this way, smooth and diffeomorphic transformations are computed to correct for susceptibility artifacts enabling an adequate fusion with the T1w and T2w images during the head model setup procedure.

## MRI acquisition

T1-, T2- and diffusion-weighted MRI scans were recorded on a 3T scanner (Gyrosan Intera/Achieva, Philips, Best, the Netherlands). A T1w pulse sequence with water selective excitation and a T2w pulse sequence with minimal water-fat-shift were used, both with cubic voxels of 1.17 mm edge length. This voxel size will determine the final FE mesh resolution. The DW imaging was performed using a Stejskal-Tanner spin-echo EPI sequence with a SENSE parallel imaging scheme in AP direction (acceleration factor = 2, TR = 7546 ms, TE = 67 ms, FOV = 240 x 240 x 131.25 mm, voxel size = 1.875 mm cubic). One volume was acquired with diffusion sensitivity  $b = 0$  s/mm<sup>2</sup> and 20 volumes with  $b = 1000$  s/mm<sup>2</sup> using diffusion weighted gradients in 20 directions, equally distributed on a sphere<sup>[75]</sup>. The pixel bandwidth was 2873 Hz/pixel and the bandwidth in the phase encoding direction was 20.3 Hz/pixel. An additional volume with flat diffusion gradient, i.e.  $b = 0$  s/mm<sup>2</sup>, was acquired with reversed encoding gradients to later use in susceptibility correction.

## Segmentation

The T2w MRI was registered onto the T1w MRI using a rigid registration approach and mutual information<sup>[88]</sup> as a cost-function as implemented in FSL<sup>a</sup>. Brain, inner skull, outer skull and skin masks were obtained from the T1w and T2w images. The gray and white matter were segmented from the T1w image and the CSF from the T2w image, using FSL<sup>[73]</sup>. The segmentation was visually inspected and manually corrected in CURRY<sup>b</sup>. Segmentation of the skull spongiosa was based on the T2w image. The skull was first constrained using the inner and outer skull masks on the T2w MRI and then a one-voxel-erosion was performed on the skull compartment, guaranteeing that inner and outer skull compacta will be at least one voxel thick. Finally, a thresholding based region-growing segmentation constrained to the eroded skull compartment was used to differentiate between spongiosa and compacta, again using CURRY.

## Geometry-adapted hexahedral finite element mesh

A hexahedral finite element mesh was constructed out of the labeled volume using SimBio-VGRID<sup>c</sup>. To increase conformance to the real geometry and to mitigate the

<sup>a</sup>FLIRT (FMRIB's Linear Image Registration Tool) is part of FSL (FMRIB Software Library), which is freely available at <http://www.fmrib.ox.ac.uk>.

<sup>b</sup>CURRY (CURrent Reconstruction and Imaging), Compumedics, Charlotte, NC, USA.

<sup>c</sup>The SimBio-Vgrid mesh generator (<http://www.rheinahrcampus.de/~medsim/vgrid/index.html>) is freely available.

staircase effects of a voxel mesh, a technique was applied to shift nodes on material interfaces<sup>[22,165]</sup>. A node shift factor of 0.33 ensured that interior angles at element vertices remained convex and the Jacobian determinant in the FEM computations remained positive. This procedure resulted in a geometry-adapted hexahedral FE mesh with 2,2M nodes and 2,2M elements.

### Conductivity tensors

The diffusion-weighted MR images were corrected for eddy current (EC) artifacts by affine registration of the directional images to the b0 image using the FSL routine FLIRT. After this procedure, the gradient directions were reoriented using the rotational part of the transformation matrices obtained in the EC correction scheme<sup>[79]</sup>. A new diffeomorphic approach for the correction of susceptibility artifacts using a reversed gradient approach and multiscale nonlinear image registration was then applied to the DW datasets<sup>a[139]</sup>. After EC and susceptibility corrections, the b0 image was rigidly registered to the T2w image using FLIRT and the transformation matrix obtained in this step was used for the registration of the directional images, while taking care that the corresponding gradient directions were also reoriented accordingly. The tensors were then calculated using the FSL routine DTIFIT<sup>[13,73]</sup>. In a last step, white matter conductivity tensors were calculated from the artifact-corrected and registered diffusion tensor images using the effective medium approach<sup>[155]</sup> and embedded in the FE head model. The scaling factor between diffusion and conductivity tensors was selected so that the arithmetic mean of the volume of all white matter conductivity tensors optimally fits the volume of the isotropic approximations in a least squares sense<sup>[136]</sup>.

### Setup of the head models

With the above-described FE mesh, five models with different conductivity properties were made (Table 3.1). The most homogenized model was a classic three-compartment model with skin, skull, and brain compartments<sup>[137,98]</sup>, which is denoted here as *3CI*. The brain compartment consists of the volumes segmented as GM, WM and CSF; the skull is a combination of compacta and spongiosa. The skull conductivity was chosen both to be in the range of the values that best approximates the layered skull<sup>[31]</sup> and to match other tDCS simulation studies<sup>[160,32,36]</sup>. The four-compartment model *4CI* incorporates the actual spongiosa and compacta compartments. Conductivity values were taken from measurements of live human skull

---

<sup>a</sup>This approach is implemented in the FAIR toolbox (Flexible Algorithms for Image Registration), which is freely available at <http://www.siam.org/books/fa06>.

**Table 3.1** Overview of the characteristics of the five models used in this study, showing which compartments each model contains and the conductivities of each tissue type.

Compartment	Conductivity (S/m)	3CI	4CI	5CI	6CI	6CA
skin	0.43 <sup>[31,130]</sup>	✓	✓	✓	✓	✓
skull	0.01 <sup>[31,130]</sup>	✓				
brain	0.33 <sup>[31,130]</sup>	✓	✓	✓		
compacta	0.007 <sup>[1]</sup>		✓	✓	✓	✓
spongiosa	0.025 <sup>[1]</sup>		✓	✓	✓	✓
CSF	1.79 <sup>[12]</sup>			✓	✓	✓
GM	0.33 <sup>[130]</sup>				✓	✓
WM	0.14 <sup>[130]</sup>				✓	
WM	anisotropic					✓

fragments<sup>[1]</sup>. The highly conductive CSF was added to the 4CI model, resulting in model 5CI. Model 6CI distinguishes between brain gray and white matter and model 6CA incorporates white matter conductivity anisotropy as described above.

### 3.2.2 Simulating tDCS

The auditory and motor cortices were located in the volume conduction model and electrodes were constructed onto the model at these locations. After tDCS was simulated with this complete model, several analyses were performed.

#### Electrode locations

The auditory and motor cortices of the subject on which the model was based were localized using 275 channel MEG experiments. For localization of A1, a source analysis was performed of the measured auditory evoked fields (AEF). The dipole solution for the auditory N1 component was calculated from the averaged AEF using CURRY. Another source analysis was performed to localize the somatosensory N20 component in the posterior wall of the central sulcus and, using this landmark, the motor cortex was identified in the nearby anterior wall of the central sulcus.

## Electrode construction

Two tDCS electrodes were modeled as rectangular patches with a commonly used size of 5 x 7 cm (Table 1.1), thickness of 4 mm and the conductivity of saline (1.4 S/m); a total current of 1 mA was applied. To simulate auditory cortex stimulation, the electrodes were positioned symmetrically around the localized auditory cortex above the area of the TP9, TP10, P7, P8, T7, T8, CP5 and CP6 electrodes of the international 10-10 system of standardized electrode placement<sup>[26]</sup> (Fig. 3.1a). The anode was placed over the right hemisphere and the cathode over the left hemisphere. For the M1 stimulation scenario, the anode was placed above the localized left M1 and the cathode above the right supraorbital area<sup>[108]</sup> (Fig. 3.1c).

## Computations

The Laplace equation (Eq. 1.5) was solved with inhomogeneous Neumann boundary conditions at the electrode surfaces and homogeneous Neumann boundary conditions for the remaining model surface<sup>[140]</sup>. Piecewise trilinear basis functions were implemented<sup>[159]</sup> with the geometry-adapted hexahedral finite element mesh. For an efficient solution of the FE equation system, an algebraic multigrid preconditioned conjugate gradient iterative solver method was used. This method is specifically appropriate for inhomogeneous and anisotropic head volume conductor models<sup>[159]</sup> and was validated in multi-layer sphere models where analytical solutions exist<sup>[101]</sup>. Significant error reductions were shown for geometry-adapted compared to regular hexahedral approaches, leading to high numerical accuracies especially for high-resolution meshes<sup>[159]</sup>. The SimBio<sup>a</sup> software toolbox was used for all FEM implementations and computations.

## 3.2.3 Analysis

From the approximated potential at the nodes, the current density was computed in each element of the volume conductor. The current density vector fields will be visualized using size-normalized color-coded cones to represent vector orientations and amplitudes. As the resolution of the mesh is too high to visualize all cones on a whole plane through the head, the resolution of the fields was decreased for most of the visualizations: only the middle cone of each 4 x 4 FE element block was visualized. All visualizations in this study were carried out using SCIRun<sup>b</sup>.

<sup>a</sup>SimBio: A generic environment for bio-numerical simulations, see <http://www.simbio.de/>.

<sup>b</sup>SCIRun (Scientific Computing and Imaging Institute, Salt Lake City, UT, USA) is freely available at <http://www.sci.utah.edu/cibc-software/scirun.html>.

The change in orientation ANG (degree) and amplitude AMP (factor) for each incorporated feature (e.g. difference between model 3CI and 4CI) were calculated and visualized for each element:

$$\text{ANG}(i) = \arccos \frac{\vec{J}_1(i) \cdot \vec{J}_2(i)}{|\vec{J}_1(i)| |\vec{J}_2(i)|} \quad (3.1)$$

$$\text{AMP}(i) = \frac{|\vec{J}_2(i)|}{|\vec{J}_1(i)|} \quad (3.2)$$

with  $\vec{J}_1(i)$  and  $\vec{J}_2(i)$  the current densities in the reference and expanded models in the  $i$ -th element, respectively. As a measure of directional agreement between the fiber directions in the brain and the calculated current densities, the parallelity PAR was calculated:

$$\text{PAR}(i) = \cos(\vec{J}(i) \cdot \vec{v}(i)) \quad (3.3)$$

with  $\vec{v}(i)$  the primary eigenvector of the conductivity tensor in the  $i$ -th element. A value of  $\text{PAR} = 1$  indicates directional similarity, whereas  $\text{PAR} = 0$  represents orthogonality.

## 3.3 Results

The current density distribution in the isotropic three-compartment model will be presented first. Then the model is extended step by step to a more realistic anisotropic six-compartment head model and the changes in current density that occur with each step are delineated. As the results for A1 and M1 stimulation did not essentially differ, most figures are only presented for auditory cortex stimulation. For M1 stimulation, only the main differences with respect to A1 stimulation will be discussed. All current density distributions will be presented on a coronal cut plane of the model at the target location (A1 or M1).

### Isotropic three-compartment model (3CI model)

Peak current densities of 1.2 A/m<sup>2</sup> are found in the skin at the edges of the electrodes (3.1b,d). Most of the current that enters the skin is deflected by the low conductive skull and tangentially channeled along the skin from anode to cathode, while minor currents penetrate the skull with mainly radial orientation. The assumption of an isotropic brain compartment leads to a homogeneous current density distribution inside the interior skull surface. Peak cortical current densities of 0.11 A/m<sup>2</sup> occur

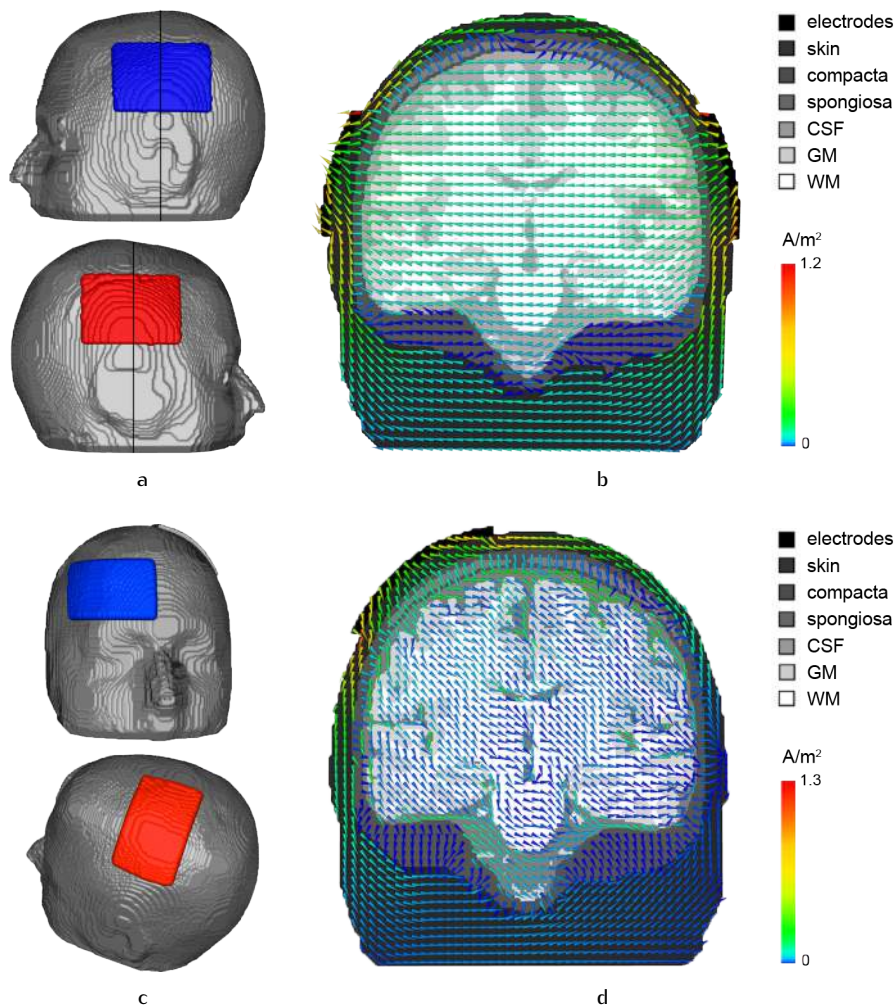


**Figure 3.1** Electrode locations and resulting current density distribution for A1 (top) and M1 (bottom) stimulation. a,c) Electrode locations on the model with the anode displayed in red and the cathode in blue. For the A1 setup, the black lines indicate the location of the cut plane on which all visualizations inside the model are presented (Figs. 3.1a and 3.2). b,d) Size-normalized color-coded cones represent the direction and amplitude of the current densities in the 3CI model for A1 and 6CA model for M1 stimulation. The distribution in the skin was similar for the other models. As this figure is scaled to the full range of values in the complete model – rendering some of the variations in the brain indistinguishable – plots showing only the brain compartment are presented for A1 stimulation in Fig. 3.2.

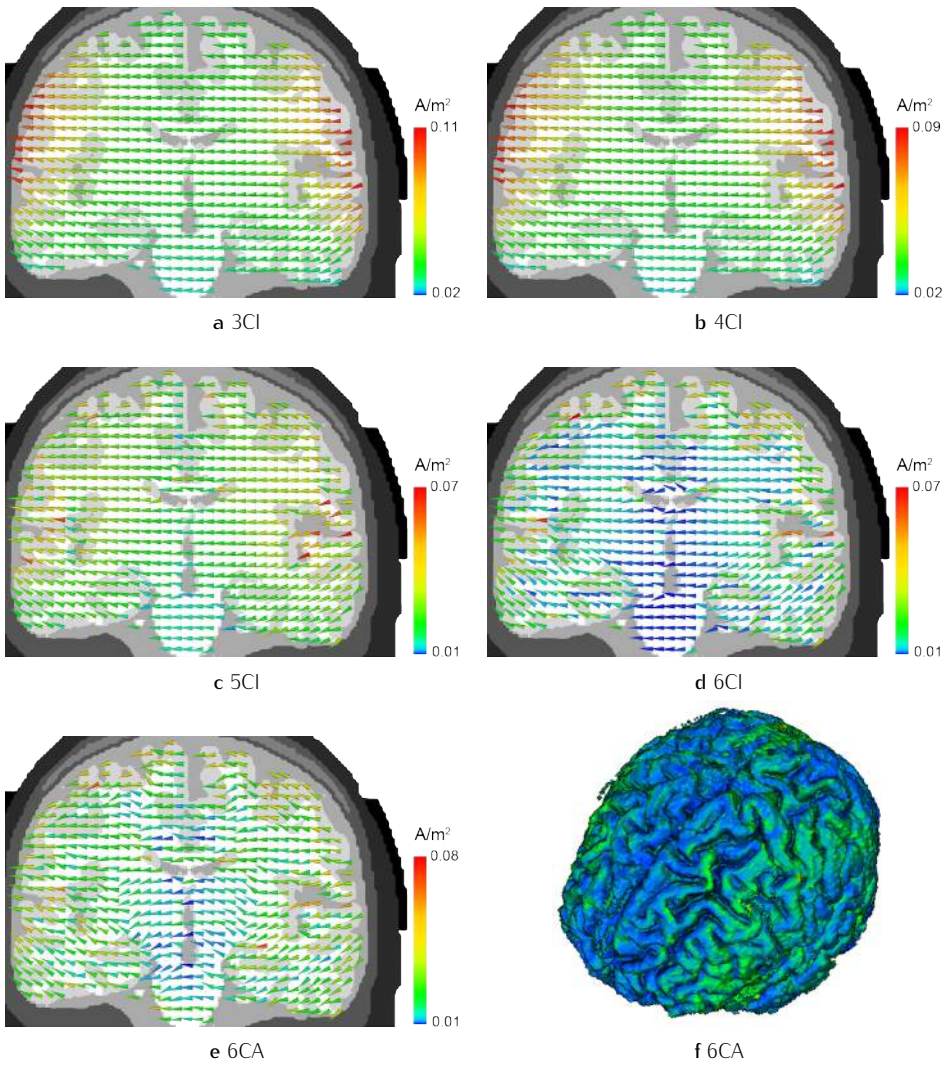


**Figure 3.2** Current density distributions in the brain compartments of five models for auditory cortex stimulation. a-e) Size-normalized color-coded cones represent the direction and amplitude of the current densities in each model on a slice through the center of the electrodes (Fig. 3.1a). f) Current density magnitude on the brain surface of the most realistic model 6CA.



in regions directly underneath the tDCS electrodes (Fig. 3.2a). The distribution of current density within the brain as a function of distance to the electrodes (Fig. 3.4) shows a correlation between distance and decrease in amplitude. That is, the current density in the 3CI model decreases smoothly toward brain regions that are farther away from the electrodes.

### Including the layered skull structure (4CI model)

Adding the distinction between skull compacta and spongiosa to the 3CI model leads to changes in orientation of up to  $64^\circ$  in the skull, while only minor changes are visible in the skin and brain (Fig. 3.3a). Because of the increased conductivity in the spongiosa compartment, orientation changes ( $\leq 9.2^\circ$ ) occur in the cortex, mostly in brain regions underneath spongiosa. This means that for A1 stimulation the target area is hardly affected, while for M1 stimulation the largest orientation changes ( $\leq 12^\circ$ ) were found in the target area (Fig. 3.5a).

The current density decreases ( $AMP < 1$ ) in the whole brain and in most compacta regions (Fig. 3.3b) and increases ( $AMP > 1$ ) in the less resistive spongiosa compartment. For M1 stimulation, current density is decreased in a cortical region underneath a large patch of spongiosa above the motor cortex (Fig. 3.5b). The locations of the peak cortical current density did not shift with respect to the 3CI model for A1 stimulation (Fig. 3.2a,b) and only showed slight changes for M1 stimulation. The correlation between distance and decrease in brain current density is similar to what was seen in the 3CI model (Fig. 3.4).

Looking in detail at a region containing a large amount of spongiosa shows that the current within the spongiosa is oriented mainly radially in the 3CI model (Fig. 3.6a1) and more tangentially in the 4CI model (Fig. 3.6a2) due to the 3.6 times higher conductivity of spongiosa compared to compacta (Table 3.1)<sup>[1]</sup>. When using the highest reported ratio of 1:8.2 from Akhtari et al.<sup>[1]</sup>, a correlation between the conductivity ratio and the tangential behavior of the vectors in the spongiosa layer can be observed (Fig. 3.6a3). To obtain mainly tangential components, a ratio of 1:23 was required (Fig. 3.6a4). The compacta-to-spongiosa conductivity ratio thus influences the direction of the current in the spongiosa, resulting in a tangential channeling effect for high ratios, which in case of M1 stimulation also significantly affected the current density in the target brain area (Fig. 3.5a,b).

### Including the CSF compartment (5CI model)

Incorporating the highly conductive CSF influences the orientation of the current density in the skull, CSF ( $\leq 75^\circ$ ) and brain ( $\leq 44^\circ$ , Fig. 3.3c). In the brain, mod-

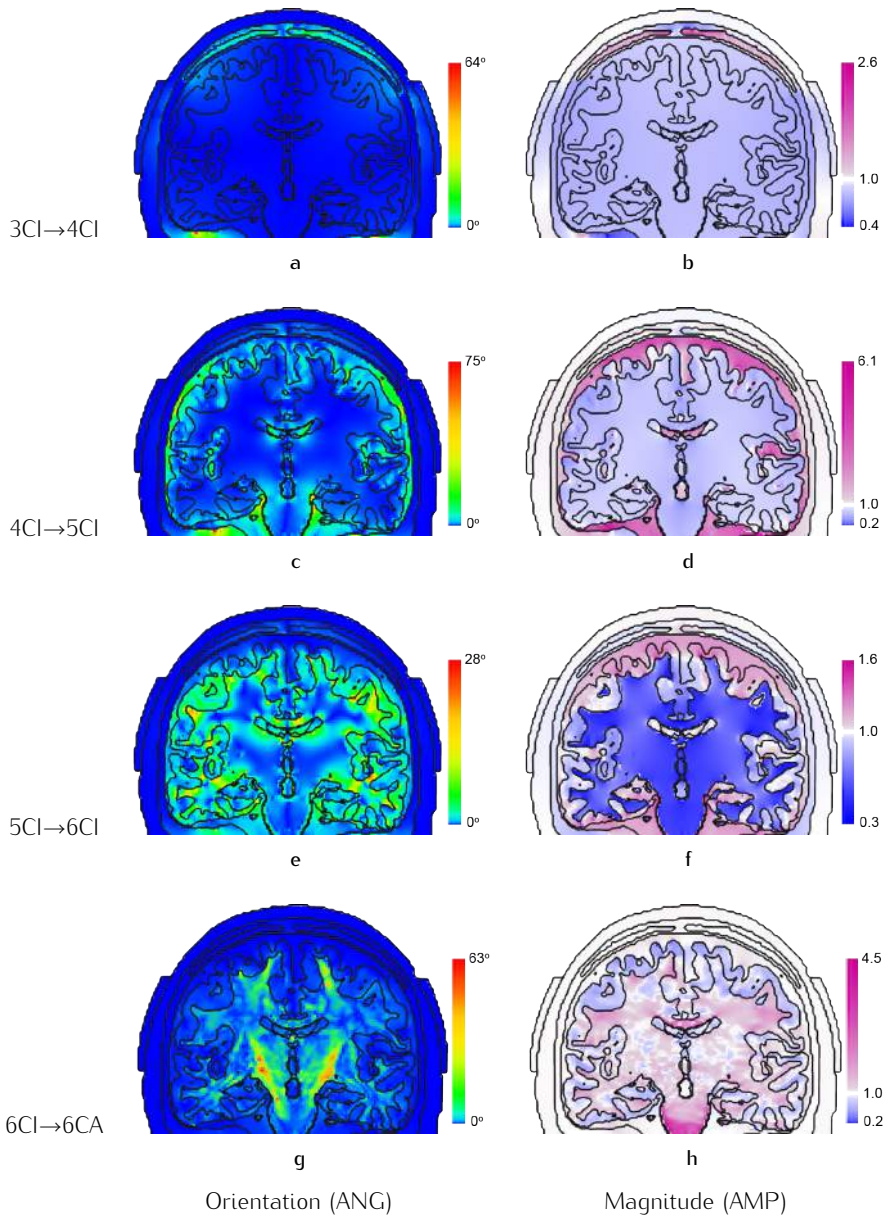


**Figure 3.3** Differences in current density for auditory cortex stimulation, shown on a slice of the model through the center of the electrodes. The left and right columns show the change in orientation (ANG) and magnitude (AMP), respectively, that resulted from adding spongiosa (a,b), CSF (c,d), GM and WM (e,f) and WM anisotropy (g,h). ANG values indicate changes in orientation irrespective of sign. For AMP values, white areas (AMP = 1) reflect no change.

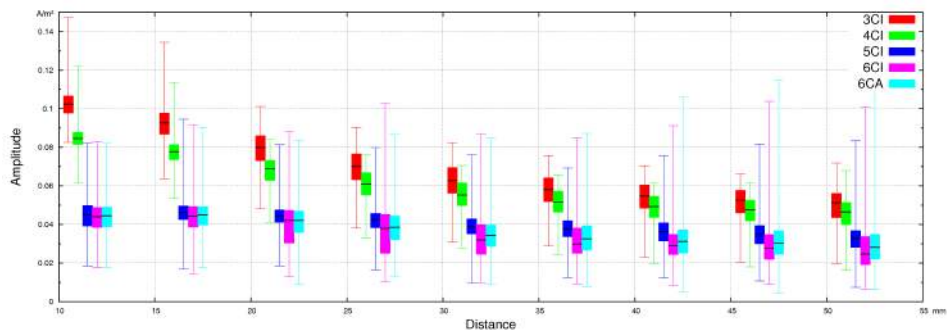


**Figure 3.4** Current density amplitudes in elements of the brain compartments located at a specific distance ( $\pm 2.5$  mm) to the nearest electrode edge are presented in a boxplot for each of the five models with A1 stimulation. The black dash marks the median current density, the box comprises the upper and lower quartile and the error bars show the minimal and maximal current densities.

ifications with regard to orientation are found in most cortical regions bordering CSF.

Due to a significant increase in conductivity, the current density in the CSF compartment increases by a factor of up to 6.1 as compared to the 4CI model (Fig. 3.3d). Current density in white matter and in most cortical regions decreases, especially close to the stimulation site. Smaller changes occur in the skull and the skin compartment is mostly unaffected.

The current density in the 5CI model decreases for an increase in distance, except for the region between distances of 10 and 15 mm to the electrodes, where amplitude increases slightly (Fig. 3.4). Compared to model 4CI, there is a decrease in current density of about 50% in brain areas close to the electrodes and a smaller decrease farther away, along with a significant increase in maximal amplitude in faraway regions.

When comparing a section of the vector field in the 4CI (Fig. 3.6b1) and 5CI (Fig. 3.6b2) models in full resolution, major changes in orientation due to the inclusion of the CSF are visible. A large amount of the current that passed the skull underneath the anode is channeled along the CSF towards more faraway regions. In the areas around gyri, the current travels mainly along and towards the CSF (Fig. 3.6b4), contrary to the homogeneous distribution in the 4CI model (Fig. 3.6b3). These effects lead to higher current density amplitudes in the sulci and an overall more irregular pattern of peak cortical current density (Fig. 3.2c).

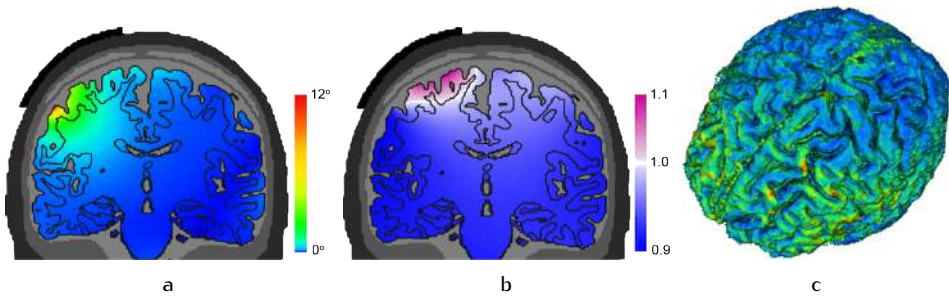


**Figure 3.5** Current density distribution and changes for motor cortex stimulation. The change in orientation (a) and magnitude (b) that resulted from adding spongiosa is shown on a slice of the model through the center of the electrodes. c) Current density magnitude on the brain surface of the most realistic model 6CA.

### Differentiating between gray and white matter (6CI model)

Modeling gray and white matter as separate compartments with distinct conductivities results in orientation changes ( $\leq 28^\circ$ ) mostly near the boundary between gray and white matter and in inferior parts of the CSF (Fig. 3.3e).

The current density increases in the CSF and decreases in the WM compartment (Fig. 3.3f). Within GM, current density decreases slightly close to the site of stimulation and increases farther away. The median current density in the whole brain does not change much close to the electrodes, but decreases farther away (Fig. 3.4).

Inspection of two brain regions around GM/WM boundaries within the 5CI (Fig. 3.6c1,3) and 6CI (Fig. 3.6c2,4) models shows that the vector field in WM tends to be oriented towards the nearest GM region. This effect is not seen farther away from the GM/WM boundaries (Fig. 3.2d).

### Incorporating white matter anisotropy (6CA model)

Adding white matter anisotropy to the 6CI model results in orientation changes of up to  $63^\circ$  in the WM compartment, with the largest changes in central WM areas. In deep areas of the GM compartment, maximal orientation changes are  $15^\circ$ . In superficial cortical areas, with 0 to  $8^\circ$  orientation changes are moderate.

The current density magnitude also changes moderately in superficial cortical areas, while factors between 0.5 and 1.3 can be found in deeper GM areas and changes up to a factor of 4.5 occur in the WM. For the whole brain the median current density decreases with increasing distance to the electrodes (Fig. 3.4). In comparison to the 6CI model, the median increased slightly in farther away areas

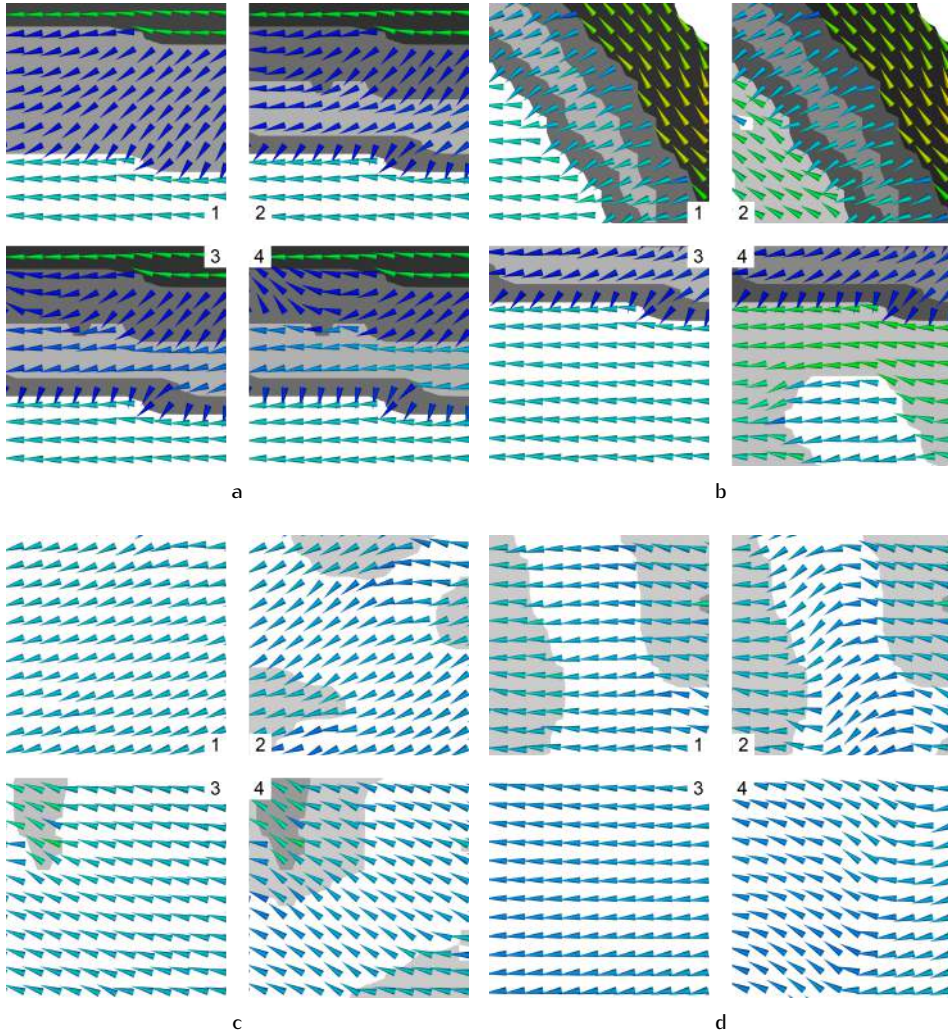


**Figure 3.6** Selected details of the current density vector field in full resolution for A1 stimulation. a) The effect of including skull spongiosa, comparing model 3CI (1) to model 4CI with compacta-to-spongiosa conductivity ratios of 1:3.6 (2), 1:8.2 (3) and 1:23 (4). b) Differences caused by incorporating the CSF compartment, at two locations in the 4CI (1,3) and 5CI (2,4) models. c) Changes caused by including a WM compartment, at two locations in the 5CI (1,3) and 6CI (2,4) models. d) Differences that resulted from including WM anisotropy, at two locations in the 6CI (1,3) and 6CA (2,4) models. The tissue labels in each figure are adapted to the compartments contained in the presented model (for legend see Fig. 3.1). Color-coding of the cones represents their amplitudes (scale identical to Fig. 3.1).



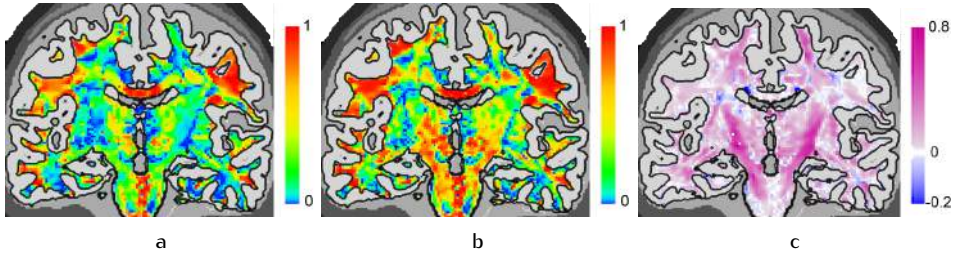


**Figure 3.7** Directional agreement (PAR, Eq. 3.3) between the current density vector in each element, resulting from A1 stimulation, and the primary eigenvector of the conductivity tensor in anisotropic WM, in the 6CI (a) and 6CA (b) models. c) Difference between the two models:  $C = B - A$ .

(distances above 30 mm from the electrodes).

In brain areas where WM anisotropy is large, such as areas containing thalamocortical projection fibers (3.6d1,2) or pyramidal tracts (3.6d3,4), large changes in orientation occur in the 6CA model (3.6d2,4) as compared to the 6CI model (3.6d1,3) in which the current density is mostly homogeneous.

Along the pyramidal tract, the directional agreement (PAR, Eq. 3.3) between the simulated current densities and the main fiber directions is much higher in the 6CA model (Fig. 3.7b) as compared to the 6CI model (Fig. 3.7a). Large differences in parallelity occur in central white matter areas (Fig. 3.7c).

3

## 3.4 Discussion

The volume conduction effects of modeling skull layers, including a CSF compartment, modeling separate GM and WM compartments and incorporating WM anisotropy in tDCS models were isolated in this study by adding and investigating one feature at a time. The results provide information that helps to understand the interaction between stimulation, volume conduction effects and the resulting cortical current density distributions caused by tDCS.

### Modeling of the skull

While previous studies investigating the effects of separate skull layers on simulations of electrical stimulation were performed with two-dimensional<sup>[64]</sup> or spherical models<sup>[132]</sup> (Chapter 2), this study was the first to investigate these effects in a re-

alistic three-dimensional tDCS model. The most basic head model showed mainly radial current flow in the skull because of the low skull conductivity of 0.01 S/m. Including spongiosa in the skull changed this behavior. Currents were tangentially channeled along the better conductive spongiosa, leading to an overall decrease in brain current density and a small effect on the current distribution in the brain. For auditory cortex stimulation, the target area was hardly affected by the presence of the spongiosa, while for motor cortex stimulation the orientation change was largest in the target area. This is due to the placement of the electrodes relative to the location of spongiosa inside the skull. The closer the electrodes are to the spongiosa, the more current is shunted through this compartment and the higher the change in brain current density is. This indicates that realistic modeling of the human skull is important when electrodes are placed over spongiosa areas.

### **Influence of the CSF**

When including CSF, current is channeled away from the target brain area due to a significantly higher (5.4 times) conductivity of CSF compared to the brain tissue. This finding is in agreement with the results of other studies<sup>[32,142,160]</sup>. The CSF leads the current both towards brain regions farther away and into the deeper lying sulci. This changes the current distribution all the way along the CSF/brain boundary and the distribution in the brain becomes less homogeneous. In regions close to the CSF, current densities are relatively high and directed towards the CSF. Within 10 to 15 mm of the electrodes, the median brain current density was increased. This is caused by conduction of currents from the cortical crown to the bottom of sulci underneath the electrodes, in agreement with previous work<sup>[142]</sup>. Of the four model features investigated in this study, the addition of the CSF had by far the largest effect on the relationship between current density and distance to the electrodes. These results show that accurate modeling of the CSF compartment as well as the brain surface is very important in tDCS simulations.

### **Including white matter**

The distinction between gray and white matter increases the resistivity within the WM compartment, leading to a strong overall decrease in WM current density. As the overall brain conductivity is now lower, there is a larger conductivity disparity between CSF and brain tissue as compared to the five-compartment model. Therefore a larger portion of the current flows through the CSF, leading to weaker currents in the brain nearby the stimulation site and stronger cortical current flow in more remote regions. The direction of WM current densities close to the GM tends to

be oriented towards the boundary due to the less resistive pathway offered by the GM. Because this conductivity difference is only slightly bigger than the disparity that was introduced by incorporating the CSF, current flow was only marginally stronger, resulting in a similar pattern of peak cortical current densities. Separate GM and WM compartments were modeled in several other studies<sup>[32,142,160,140]</sup>, but only one described the effects of this distinction<sup>[140]</sup>. They reported that changing the conductivity of the WM compartment led to small changes in current densities in the brain compartment, similar to the results found here. As the distinction between gray and white matter significantly influences the orientation and magnitude of the current flow in the whole brain, a WM compartment should be modeled in tDCS simulations.

### Effects of white matter anisotropy

After adding WM anisotropy, substantial effects on GM current density orientation and magnitude were only found in deeper regions. In contrast, a strong increase in current density was seen in large parts of the WM compartment. Current flow in WM was oriented more parallel to the main direction of the fiber bundles. This effect was clearly visible especially in the pyramidal tract and thalamocortical projection fiber tract regions and is caused by the significant conductivity increase in directions parallel to the fiber bundles. These results are in agreement with the findings of investigations in a 2D<sup>[64]</sup> and a 3D model<sup>[148]</sup> using point electrodes, and a 3D model with patch electrodes<sup>[111]</sup>. While the previous 3D studies used fixed anisotropy ratios of 1:10 longitudinally to transversally to the WM fibers<sup>[111,148]</sup>, the research described in this chapter employed the linear effective medium approach to compute WM anisotropic conductivity. Furthermore, using a geometry-adapted hexahedral FE model with over 2 million nodes, the resolution in the present work was much higher than in previous investigations with  $147 \times 10^3$ <sup>[111]</sup> or  $160 \times 10^3$  nodes<sup>[148]</sup>. Therefore, this study is the first to evaluate WM conductivity anisotropy in a realistic high-resolution 3D scenario for tDCS. The findings presented here suggest that modeling WM anisotropy is important when considering deeper target regions.

### Recommendations for tDCS modeling

By comparing the isolated effects of each additional feature, directions for efficient yet accurate tDCS modeling can be composed. A volume conductor model for tDCS should contain all important tissues located in between the electrodes and the target brain areas. Isotropic representations of the skin, skull, CSF, GM and WM should be included. The skull should be distinguished into its compacta and spongiosa



compartments when there is a significant volume of spongiosa in the area between the electrodes and the target. Modeling WM conductivity anisotropy is important for deeper target areas, while it seems less important for superficial targets where no significant anisotropy exists between electrodes and targets.

### **Auditory and motor cortex stimulation**

Simulations of tDCS targeting auditory cortex have not been reported before. In this study, simulation of auditory tDCS in the most realistic head model leads to highest median current densities in brain regions close to the stimulation site; the bigger the distance towards the nearest electrode node, the smaller the median brain current density. Although the pattern of peak current densities is irregular, brain regions close to the stimulation site receive highest median current densities. It thus seems that for auditory cortex stimulation the here-presented configuration is optimal and that for most subjects the best approach would be to place the electrodes over the auditory cortices. It should be noted that in this case both cortices are stimulated equally strong but with reversed direction. In order to have one of the two effects (excitation or inhibition) dominate over the other, the use of different electrode sizes has been suggested. For example, in order to achieve local excitation a small anode should be placed over the target region and a large return electrode elsewhere, thus minimizing the effect of inhibition<sup>[105]</sup>.

For motor cortex stimulation the conventional configuration did not lead to maximal current densities in the motor cortex (Fig. 3.5c). The results presented here suggest that higher current densities in the target area and bigger experimental effects of tDCS can be achieved with better suited electrode configurations. Conventional and optimized motor cortex tDCS will be further investigated in Chapters 4–6. For both motor and auditory cortex stimulation the locations of the peak cortical current density in the most realistic head model were widely distributed within the brain. Thus, brain regions outside the target area can be unnecessarily influenced by distantly located electrodes. Such unwanted stimulation can possibly be reduced by increasing focality and improving targeting through the use of multiple smaller electrodes<sup>[33,36]</sup>.

### **General discussion**

This study investigated the effects of including separate skull, CSF, GM and WM compartments, as well as WM anisotropy, on tDCS volume conduction. While other authors allude the importance of these features<sup>[160,64,32,114]</sup>, this study is the first that investigates all these aspects and allows a direct comparison of effect sizes.

Also, where other studies only investigated field strengths or current density values, the present study investigated orientation effects as well and clearly indicated the current flow and the influence of important effects by visualizing complete vector fields.

The influence of the current density orientation in tDCS has been demonstrated by polarity-dependent effects on cortical excitability<sup>[108]</sup> and in several other tDCS experiments<sup>[4,77]</sup>. The results in this chapter showed the strong influence of especially the CSF and WM compartments on the orientation component of the brain current density, underpinning the necessity of including these tissue compartments for accurate tDCS modeling. Another obvious aspect of the simulation results is that currents in lower-conducting regions tend to be oriented towards the closest higher conductive region. This effect that arises as a result of less resistive current pathways in the higher conductive regions and has not been mentioned before.

An interesting question, raised in many tDCS experiments, is whether weak direct currents introduced to big electrodes positioned at the head surface can have therapeutic effects<sup>[49]</sup>. It has been demonstrated that an electric field of about 140  $\mu\text{V}/\text{mm}$  is sufficient to enhance the firing rate of neurons<sup>[43]</sup>. The strongest electric fields in the presented coronal slice of the six-compartment head model with white matter anisotropy, indeed, are about 239  $\mu\text{V}/\text{mm}$  and 167  $\mu\text{V}/\text{mm}$  for auditory and motor cortex stimulation, respectively, and therefore above this threshold.

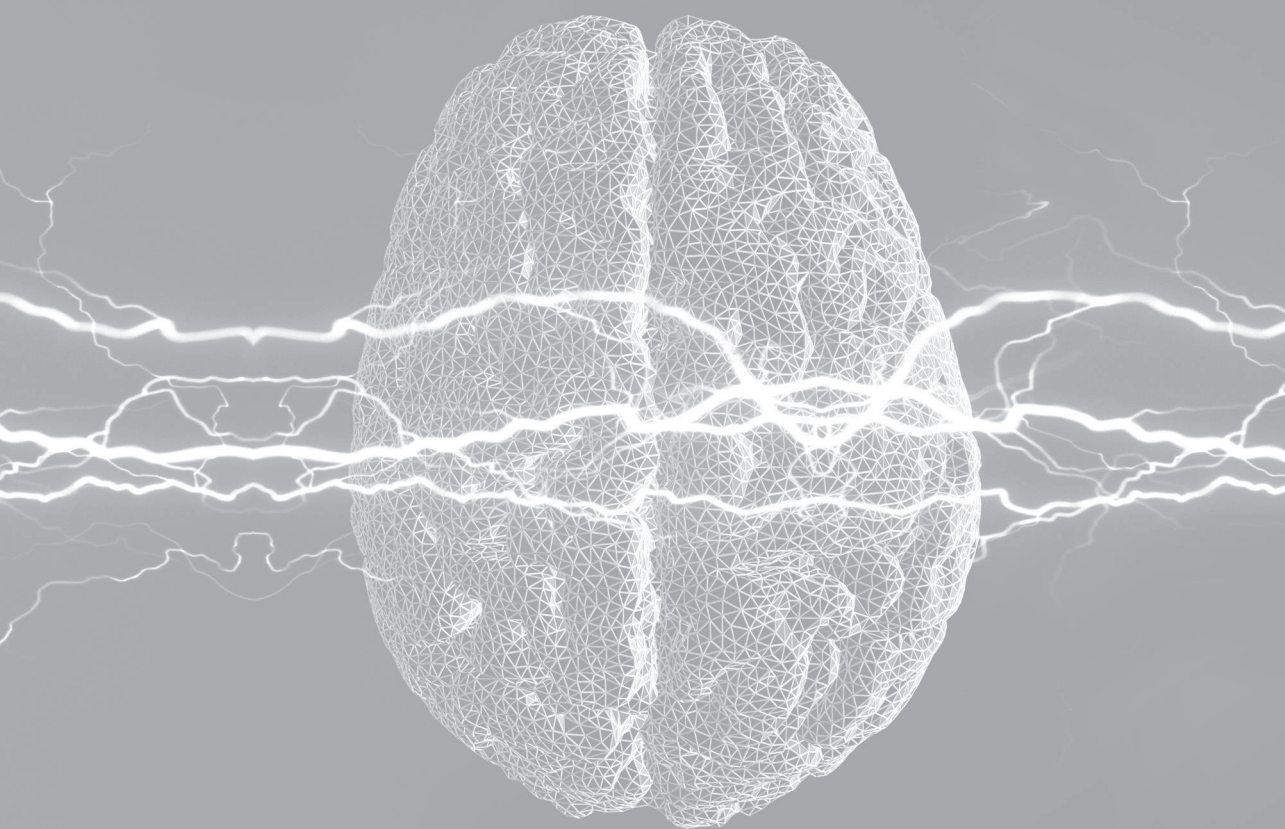
Details in head volume conductor modeling have a significant effect on the predicted tDCS-induced current density distributions. However, interindividual variability of conductivity parameters, as shown for example for the skull tissues<sup>[1]</sup>, might cause significant modeling errors necessitating future empirical direct and indirect validation studies in animal and human subjects. Direct validation might involve combined tDCS stimulation and electric field measurements using depth electrodes in brain target areas. Such combined data might allow to directly validate simulation studies and to adjust interindividually differing tissue conductivity parameters in a way that the simulated brain current flow fits to the measured one. Surface EEG can be used to indirectly validate tDCS simulations<sup>[103]</sup>.

## 3.5 Conclusions

A volume conductor model for tDCS should contain all important tissues located between the electrodes and the target brain areas. While detailed isotropic representations of the skin, skull, CSF, GM and WM compartments are always required for accurate tDCS simulations, dividing the skull into its compacta and spongiosa com-

partments is only necessary when there is a significant volume of spongiosa in the area between the electrodes and the target. Modeling WM conductivity anisotropy is especially important for deeper target areas.





## Chapter 4

# Electric field distributions for six conventional configurations



Based on: *Simulating transcranial direct current stimulation with a detailed anisotropic human head model*, by Sumientra Rampersad, Arno Janssen, Felix Lucka, Ümit Aydin, Benjamin Lanfer, Seok Lew, Carsten Wolters, Dick Stegeman and Thom Oostendorp, published in IEEE Transactions on Neural Systems and Rehabilitation Engineering in 2014.



## 4.1 Introduction

---

In order to better understand the mechanisms behind tDCS and possibly improve the technique, it would be helpful to know the distribution of the electric field in the brain resulting from the conventional electrode configurations. Most modeling studies that investigated these fields have focused on motor cortex stimulation<sup>[33,68,142,163]</sup>. For prefrontal cortex<sup>[113,160]</sup> and occipital cortex<sup>[58,160]</sup> a few modeling studies exist. Realistic simulations of other commonly used electrode configurations have not been published before. Furthermore, the models used in the above-mentioned studies did not include all possibly relevant features that might increase the accuracy of the simulations.

In the study presented here, tDCS was simulated for the six most commonly used configurations in clinical and cognitive research. These configurations are used to target the primary motor cortex (M1), dorsolateral prefrontal cortex (DLPFC), inferior frontal gyrus (IFG), occipital cortex and cerebellum for a wide range of applications (Table 1.1). Both the locations of the electrodes and their shapes were modeled according to the most widely used forms in experimental research.

The accuracy of a volume conduction model is determined by how well it describes the geometry and the conductivity properties of the head. The amount of geometric detail can be increased by decreasing the size of the elements and incorporating more tissue compartments. The accuracy of the conductivity can be further increased by incorporating anisotropic conductivity tensors that represent realistic fiber directions. Currently, tDCS models exist that consist of several million elements representing a multitude of tissue types<sup>[113,141,33,163]</sup>. In some studies the layered structure of the skull was considered<sup>[132,149]</sup> and anisotropic conductivities of white matter<sup>[149,145]</sup> or both gray and white matter<sup>[163]</sup> have been incorporated. All in all, many important details of tDCS volume conduction have been modeled accurately, but no study yet has incorporated all these features into a single model. The model presented here includes all these aspects and will be used to provide the currently most accurate predictions of tDCS in the human brain for six commonly used configurations.

As is common in tDCS modeling studies<sup>[33,113,68]</sup>, resulting electric field strengths will be presented in the complete brain. Additionally, this study introduces a new method to evaluate the results in the target area specifically and also investigates the direction of the field. These analyses will show that for all cerebral targets studied, the currently accepted configurations lead to sub-optimal field strengths, while the conventional configuration for cerebellar tDCS performs relatively well.



## 4.2 Methods

---

A realistic tetrahedral FE model of a human head was constructed for this study and six commonly used tDCS electrode configurations were simulated with this model. The magnitude and direction of the resulting electric fields were analyzed in various ways.

### 4.2.1 Volume conduction model

A detailed anisotropic volume conduction model was constructed based on MR images of the head of a healthy 25-year old male subject. Written informed consent was obtained prior to scanning. T1- and T2-weighted images were used to reconstruct realistic geometries of the skin, skull compacta, skull spongiosa, CSF, cerebral gray (GM) and white matter (WM), cerebellar gray (cGM) and white matter (cWM), brainstem, eyes and neck muscles, in the form of a triangular surface mesh for each tissue type. These surfaces were then combined into one tetrahedral volume mesh. Anisotropic conductivity was included for both gray and white matter of cerebrum and cerebellum. The creation process of the model is visualized schematically in Figure 4.1 and details are provided below. Some important features of the model are shown in Figure 4.2.

#### MRI acquisition

T1-, T2- and diffusion-weighted MR images were measured on a 3T MR scanner (Magnetom Trio, Siemens, Munich, Germany) with a 32-channel head coil. The T1-weighted (T1w) image was acquired with an MP-RAGE pulse sequence (TR = 2300 ms, TE = 3.03 ms, TI = 1100 ms, flip angle = 8 degrees, FOV = 256 x 256 x 192 mm, voxel size = 1 x 1 x 1 mm) with fat suppression and GRAPPA parallel imaging (acceleration factor = 2). The T2-weighted (T2w) image was acquired with an SPC pulse sequence (TR = 2000 ms, TE = 307 ms, FOV = 255 x 255 x 176 mm, voxel size = 0.99 x 1.0 x 1.0 mm interpolated to 0.498 x 0.498 x 1.00 mm). The T2w sequence was adjusted such that it gives a high contrast between the different layers of the skull (Fig. 1.7a). The field of view of both scans captured the complete head and was cut at the chin.

The diffusion-weighted (DW) images were acquired with the standard Siemens pulse sequence ep2d\_diff (TR = 7700 ms, TE = 89 ms, b-value = 1000 s/mm<sup>2</sup>, bandwidth = 2000 Hz/pixel, FOV = 220 x 220 x 141 mm, voxel size = 2.2 x 2.2 x 2.2 mm) in 61 directions equally distributed on a sphere and 7 images were acquired

with flat diffusion gradient (diffusion weighting factor  $b = 0$  ( $b0+$ )). Additionally, seven images with flat diffusion gradient (diffusion weighting factor  $b = 0$  ( $b0-$ )) with reversed phase and frequency encoding gradients were acquired.

## Segmentation

The T2w MRI was registered onto the T1w MRI using a rigid registration approach and mutual information as a cost-function as implemented in FSL<sup>a</sup> ( $\rightarrow 1$ , refers to arrow 1 in Figure 4.1). The compartments skin, skull compacta and skull spongiosa were then segmented from the registered T1w and T2w images using a gray-value based active contour model<sup>[158]</sup> and thresholding techniques ( $\rightarrow 2$ ). These segmentations were carefully checked and corrected manually to ensure the highest possible agreement with the MR images and to make sure the different tissues formed closed surfaces. Eye, muscle and vertebrae segmentations were added manually. The foramen magnum and the two optic canals were modeled as skull openings ( $\rightarrow 3$ ). Exemplary sagittal slices of both the automatic segmentation and manual alterations can be seen in the flowchart in Figure 4.1 after arrow 2 and 3, respectively. The segmentation of GM, WM, cGM, cWM and brainstem was extracted from brain parcellation data of the T1w image created with Freesurfer<sup>b</sup> software ( $\rightarrow 5$ ).

## Triangular surface meshes

CURRY<sup>c</sup> was used for the extraction of high resolution triangular surface meshes of the skin, eyes, compacta, spongiosa and muscles from the voxel-based segmentation volumes ( $\rightarrow 4$ ). The surfaces were smoothed using Taubin smoothing<sup>[152]</sup> to remove the blocky structure which results from the fine surface sampling of the voxels.

Triangular surface meshes of all brain parcellations were made in MATLAB and refined using the iso2mesh package<sup>d[40]</sup>. As Freesurfer produces separate segmentations for each hemisphere, the hemispheres were connected and self-intersections were removed with custom MATLAB code. In the subsequent step of this process – creation of a volume mesh from the surface meshes – the surfaces are not allowed to touch. Therefore, the part of the WM surface that extended out of the GM surface especially in the inferior brain region was identified and corrected using the custom code. To avoid intersections between the gray matter and compacta surfaces, the complete brain was scaled down by 2% and flattened at remaining intersec-

<sup>a</sup>FLIRT (FMRIB's Linear Image Registration Tool) is part of FSL (FMRIB Software Library), which is freely available at <http://www.fmrib.ox.ac.uk>.

<sup>b</sup>Freesurfer is freely available at <http://surfer.nmr.mgh.harvard.edu>.

<sup>c</sup>CURRY (CURrent Reconstruction and Imaging), Compumedics, Charlotte, NC, USA.

<sup>d</sup>The iso2mesh package is freely available at <http://iso2mesh.sourceforge.net/cgi-bin/index.cgi>.

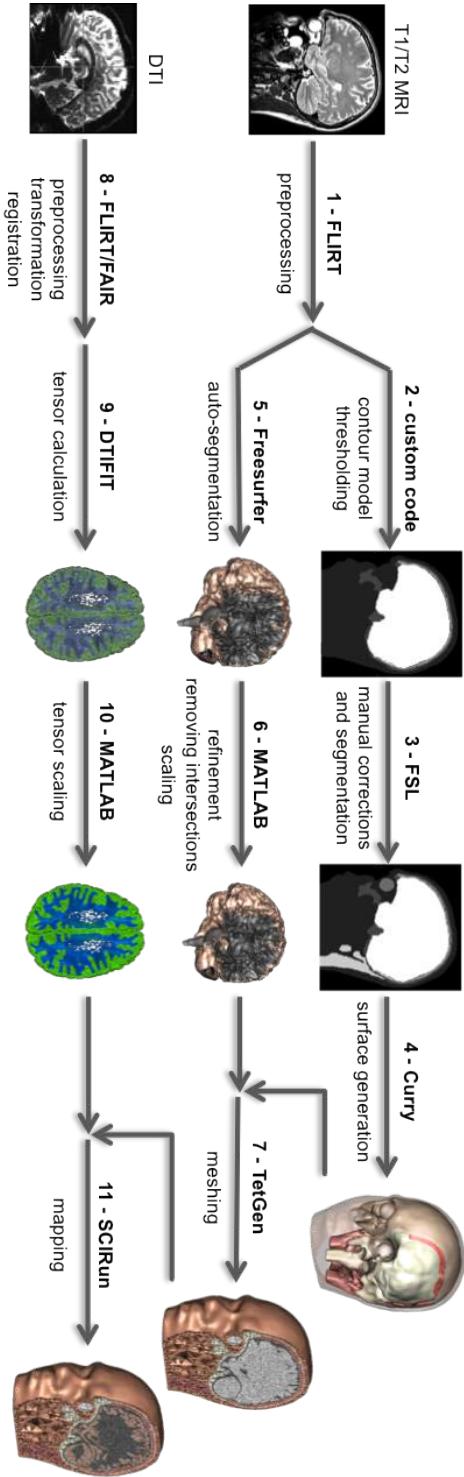


**Figure 4.1** Flowchart showing the creation process of the volume conduction model. T1- and T2-weighted MR images were preprocessed (1) and after automatic (2) and manual segmentations (3), triangular surface meshes were created for the skin, skull compacta and spongiosa, neck muscles and eyes (4). Surfaces for the cerebral and cerebellar gray and white matter and the brainstem were extracted from Freesurfer (5) and refined, made free of intersections and scaled with MATLAB (6). All surfaces were then combined into a tetrahedral volume mesh (7). Diffusion tensor imaging data was preprocessed, transformed and registered to the T1w/T2w scans (8), after which diffusion tensors (9) and conductivity tensors (10) were calculated. Finally, the conductivity tensors were mapped onto the mesh from (7) to result in a detailed tetrahedral mesh with conductivity tensors (11).

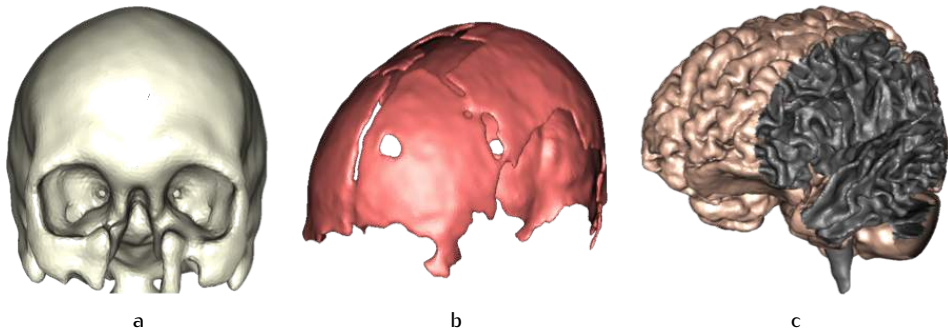


**Figure 4.2** Selected surfaces and details of the volume conduction model. a) Outer skull surface with optic canals, b) spongiosa surface and c) surfaces of the cerebral and cerebellar gray and white matter and the brainstem.

tions ( $\rightarrow 6$ ). Figure 4.2 shows the skull surface with the optic canals, the detailed spongiosa surface and all five brain surfaces.

### Tetrahedral volume meshes

The smoothed surfaces (skin, compacta, spongiosa, GM, WM, cGM, cWM, brainstem, left eye, right eye, muscle) were used to create a high-quality 3D Delaunay triangulation via TetGen<sup>a</sup> ( $\rightarrow 7$ ). This resulted in a mesh consisting of 672k nodes and 4.12M linear tetrahedral elements. The element size in the brain was restricted to  $1 \text{ mm}^3$ . Due to the use of detailed surfaces, the elements of the skull and CSF compartments are very small as well. A tissue index was assigned to all elements in the space between two surfaces, or inside a closed surface. An additional closed skull surface was used to label all elements within this skull surface that are not part of the brain compartments, as CSF.

### Conductivity tensors

All elements of the skin, skull, CSF, eye and muscle compartments were assigned an isotropic conductivity tensor with values taken from the literature (Table 4.1). In the brain compartments, each element received its own anisotropic tensor calculated from the diffusion-weighted MR images. The images were first corrected for eddy current (EC) artifacts by affinely registering each directional image to the average  $b_0+$  image using the FSL routine FLIRT. After EC correction, the gradi-

<sup>a</sup>TetGen (A quality Tetrahedral mesh Generator and a 3D Delaunay triangulator) is freely available at <http://tetgen.org>.

**Table 4.1** Tissues represented in the head model and conductivities used for each compartment. Conductivities denoted with an asterisk are effective conductivities of the volume-normalized tensors of the anisotropically modeled tissues<sup>[112]</sup>.

Tissue	Conductivity (S/m)	Tissue	Conductivity (S/m)
skin	0.465 <sup>[160]</sup>	GM, cGM	0.276* <sup>[160]</sup>
compacta	0.007 <sup>[1]</sup>	WM, cWM	0.126* <sup>[160]</sup>
spongiosa	0.025 <sup>[1]</sup>	brainstem	0.201* (average GM/WM)
muscle	0.4 <sup>[39]</sup>	CSF	1.65 <sup>[160]</sup>
eye	1.5 <sup>[102]</sup>		

ent directions were reoriented by multiplying them with the rotational part of the transformation matrix<sup>[79]</sup>. In order to correct for susceptibility artifacts, a reversed gradient approach was applied that uses the averaged b0+ and b0- images to compute smooth and diffeomorphic geometric transformations using a problem-adapted multiscale nonlinear image registration procedure<sup>a</sup><sup>[139]</sup>. The EC and susceptibility corrections allowed a simple rigid registration of the artifact-corrected averaged b0 image to the T2w image (which was already registered to the T1w image in a previous step) using FLIRT. The transformation matrix obtained in this step was then used to register the directional images to the T2w image (which is in T1 space). The corresponding gradient directions were also reoriented accordingly. From the artifact-corrected and registered DW images (→8) the diffusion tensors were calculated using the FSL routine DTIFIT<sup>[13,73]</sup> (→9). Next, conductivity tensors were calculated from these diffusion tensors using the volume-normalized approach, as described in detail by<sup>[112]</sup> (→10). The normalized eigenvectors were multiplied with the effective conductivities of the tissues for GM, WM and brainstem separately<sup>[112]</sup>. In the last step, the conductivity tensors were mapped from the MRI voxels onto the GM, WM, cGM, cWM and brainstem compartments of the tetrahedral head mesh (→11).

## 4.2.2 Simulating tDCS

The M1, DLPFC, IFG, occipital cortex and cerebellum are commonly targeted with tDCS using a standard set of electrode locations (Table 4.2). This section describes how these locations were identified in the model and how electrodes were built

<sup>a</sup>This approach is implemented in the FAIR toolbox (Flexible Algorithms for Image Registration), which is freely available at <http://www.siam.org/books/fa06>.

onto the model at these locations (Fig. 4.3). After setting the boundary conditions, the problem could be solved.

### Electrode locations

In tDCS experiments targeting M1, the anode is usually placed over the hand area of the motor cortex, which is identified via single-pulse TMS and EMG (Section 1.1.2). These methods were also used for this study: the location of the cerebral representation of the first dorsal interosseus (FDI) muscle of the right hand was experimentally determined in the volunteer on which the model was based. The location on the head that elicited the highest potential in the FDI muscle was accurately determined using neuronavigation software (Localite TMS Navigator<sup>a</sup>) and the T2w MRI data set that was used to create the model. This location in the model was used as the center of the anode; it was placed with its short edge parallel to the midline of the brain (Fig. 4.3a). The cathode was placed over the right supraorbital area (SOA), not crossing the midline. The same location was used for the reference in configurations C and D (Fig. 4.3a,c,d).

For stimulation of the left DLPFC, the reference is either placed over the right SOA or the right DLPFC. Both dorsolateral prefrontal cortices and the left IFG were located on the brain surface of the model based on anatomical knowledge. The electrodes were placed centered over these areas covering the target area completely (Fig. 4.3b,c,d).

The anode for occipital cortex stimulation was placed 4 cm above the inion, a point which was located on the skull surface of the model, and the Cz electrode was centered at the vertex, both with their long edges parallel to the midline of the brain (Fig. 4.3e). For cerebellar stimulation, the square anode was placed with its center 3 cm right of the inion and the cathode was placed on the middle of the right cheek (Fig. 4.3f).

### Electrode construction

The electrodes were modeled as sponges with a thickness of 3 mm and the conductivity of saline (1.4 S/m). The sizes of the electrodes were chosen to match common practice in recent experiments (Table 1.1). For the configurations with cerebral targets, the electrodes were 5 x 7 cm; for cerebellar stimulation, the electrodes were 5 x 5 cm. Straight edges of the electrodes were made by splitting tetrahedrons on the surface of the model with custom C++ code and adding six layers of tetrahedrons on top of the resulting rectangular patch. The nodes in the top layer of the anode

<sup>a</sup>Localite GmbH, Sankt Augustin, Germany.

**Table 4.2** The tDCS electrode configurations that were simulated in this study. These configurations are commonly used for a wide range of applications (Table 1.1, p. 10). The electrode placement described here is used for excitative stimulation; reversing the polarity would induce inhibition.

	Target area	Anode	Cathode
A	motor cortex (M1) hand area	left M1 FDI <sup>(a)</sup>	right SOA <sup>(b)</sup>
B	dorsolateral prefrontal cortex (DLPFC)	left DLPFC	right DLPFC
C	dorsolateral prefrontal cortex	left DLPFC	right SOA
D	inferior frontal gyrus (IFG)	left IFG	right SOA
E	occipital cortex	occipital cortex	vertex
F	cerebellum	right cerebellum	right cheek

<sup>(a)</sup>Cortical representation of the right first dorsal interosseus muscle.

<sup>(b)</sup>Supraorbital area.

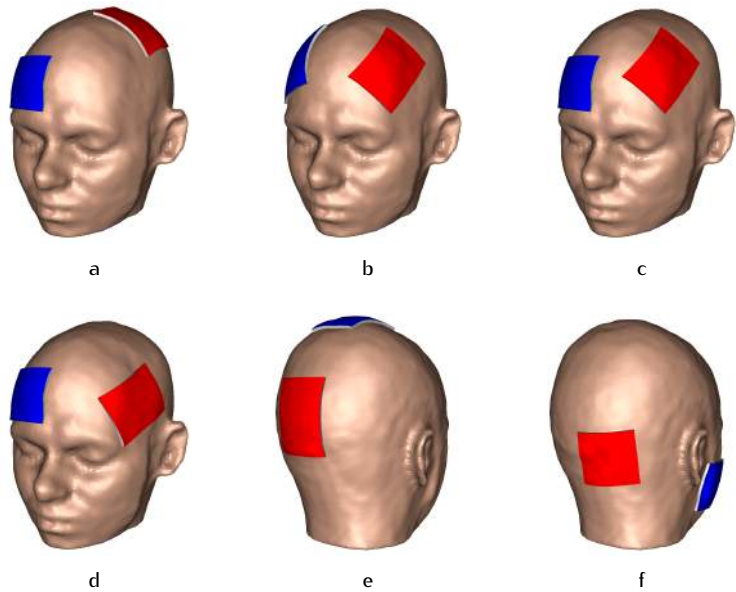


**Figure 4.3** The six conventional tDCS configurations simulated in this study, targeting a) M1, b,c) DLPFC, d) IFG, e) occipital cortex and f) cerebellum. The red surfaces indicate simulation of a positive potential  $+\phi_0$  (anode) and the blue surfaces indicate simulation of a negative potential  $-\phi_0$  (cathode).

were assigned a potential  $+\phi_0$  and the top layer of the cathode was assigned  $-\phi_0$ , with  $\phi_0$  chosen such that the total current entering the skin is equal to 1 mA.

### Computations

Laplace's equation (Eq. 1.5) was solved on the finite element mesh described above with Neumann boundary conditions at the skin surface outside the electrodes and Dirichlet boundary conditions on the surfaces of the electrodes (Eq. 1.6). The system of equations was solved with the FEM solving package SCIRun 4.6<sup>a</sup> using a conjugent gradient solver and Jacobi preconditioner with a maximal residual of  $10^{-10}$ . These calculations resulted in a potential  $\phi$  at each node of the finite element mesh. From the potential  $\phi$  at the nodes and the conductivity tensors  $\sigma$  at the elements, the electric field  $\vec{E} = -\nabla\phi$  and the current density  $\vec{J} = \sigma\vec{E}$  were calculated in each element.

### 4.2.3 Analysis

The resulting electric field distribution was investigated 1) on the brain surface, 2) in the complete brain volume, and 3) in a small target volume. In the following text, for cerebral stimulation (configurations A-E) interchange *brain* with *cerebrum* and for cerebellar stimulation (configuration F) interchange *brain* with *cerebellum*.

#### Surface

At each target location, a  $1 \text{ cm}^2$  circular patch was built into the GM surface mesh to find the current entering the GM exactly at the target location ( $I^T$ ). Next, the maximum electric field strength over the GM surface ( $|\vec{E}|_{\text{mx}}^S$ ) was determined, where the maximum was defined as the median of the 0.01% highest values. As a measure of focality, the surface area ( $A_{75}$ ) at which the field strength is above 75% of  $|\vec{E}|_{\text{mx}}^S$  was calculated.

#### Volume

The maximum electric field strength in the complete brain volume ( $|\vec{E}|_{\text{mx}}^V$ , where the maximum was again defined as the median of the 0.01% highest values) was determined. As the curved cortex leads to multiple areas where the electric field is (near-) maximal, it is not possible to indicate *the* location of maximum electric field strength. Therefore, histograms will be provided of the electric field strength values

<sup>a</sup>SCIRun (Scientific Computing and Imaging Institute, Salt Lake City, UT, USA) is freely available at <http://www.sci.utah.edu/cibc-software/scirun.html>.



in the complete brain volume. In order to understand the distribution of the electric field both close to the target and in the complete brain, all brain elements were divided into subsets based on the distance of their centers from the target (Fig. 4.7c). For each subset, a histogram of the electric field strengths in the elements will be displayed, expressed in volume fractions (sum of volumes of elements in a bin divided by total volume of subset).

### Target volume

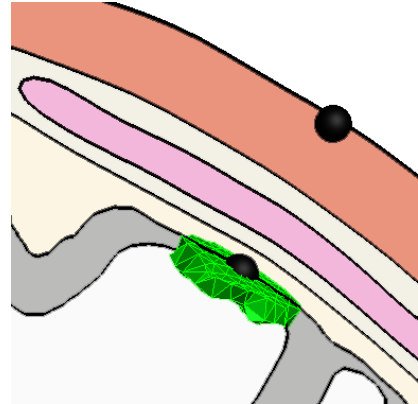
To provide a measure of the effects of tDCS exactly in the targeted region, a target volume was constructed at each target location in the brain. Exactly underneath the center of the anode, a  $1 \text{ cm}^2 \times 4 \text{ mm}$  cylindrical mesh was placed inside the GM with its axis perpendicular to the GM surface (Fig. 4.4). All GM elements within this cylinder were selected as the target volume at this location. The resulting target volume is thus a  $1 \text{ cm}^2$  slab of cortex. Different dimensions of the target area were investigated and, as expected, led to slightly different values (e.g. a thinner layer leads to higher average field strength, because deeper elements have lower field strengths), but the trend in the results was consistent. The mean ( $|\vec{E}|_{mn}^T$ ) and maximum ( $|\vec{E}|_{mx}^T$ ) field strength in each target volume were used here as estimates of the effect of tDCS in the target area.

Several studies have reported that effects of electrical stimulation are highest when the electric field is directed parallel to the fibers<sup>[138,127]</sup>. As pyramidal neurons lie perpendicular to the GM surface<sup>[62]</sup>, the electric field strength normal to the GM surface can be expected to be the most effective. Therefore this value was calculated for each element in a GM target volume: the scalar product of the electric field vector ( $\vec{E}$ ) with the normal vector to the closest GM surface triangle ( $\hat{n}$ ) was determined. The normal to the GM surface was defined as pointing inward, so that positive values of  $\vec{E} \cdot \hat{n}$  indicate an inward directed field and thus current flowing inward. The mean value within the volume ( $\vec{E} \cdot \hat{n}_{mn}^T$ ) will be provided.

## 4.3 Results

The results of 1 mA tDCS on the GM surface, in the complete brain volume and in the target volume are presented for six configurations. As tDCS volume conduction is a linear process, the results described here can be scaled to any input current by multiplying the electric field strengths with the desired current in mA. The results can also be extrapolated to cathodal stimulation; this reverses the polarity of the

**Figure 4.4** The M1 FDI target volume. The figure shows the skin, skull and brain compartments on a slice through the model. The black spheres indicate the location of the FDI target on the skin and the projected location on the GM surface. Centered on this location, a target volume of GM elements was selected (shown in green) between the GM and WM boundaries with a surface area of approximately 1 cm<sup>2</sup>. For each target area, a target volume was constructed following this approach.



field but does not affect the magnitude.

### Surface

On the skin surface the simulated electric field is high under the edges of both electrodes with peaks at the corners (Fig. 4.5a). The highest values are found at the corners closest to the other electrode. On the surface of the skull the highest values remain under the electrodes, but the distribution is more homogeneous (Fig. 4.5b). Field strengths on the skin and skull surfaces showed similar patterns for all configurations. On the brain surface this distribution of high electric field strengths under both electrodes has merged into one more central area (Fig. 4.6b). For all five cerebral targets the peak electric field locations have shifted away from the electrodes and the maximum result of stimulation is found in between the two electrodes (Fig. 4.6). A large area of (near-)maximal electric field is spread over multiple gyri on both hemispheres, roughly centered on the midline, with the highest values closer to the anode. For M1 stimulation this area is stretched along the coronal plane; for the prefrontal configurations it lies along the sagittal plane; for IFG and occipital cortex stimulation the maximally stimulated areas are more circular. The simulations of cerebellum stimulation show a large patch of high electric field strength on the inferior surface of the right cerebellar hemisphere, covering the target area. In addition, an area of maximal field strength is found more inferior and medial on a highly concave surface area.

Maximum electric field strengths ( $|\vec{E}|_{mx}^S$ ) range from 2.4 to 3.2 mV/cm for the cerebral targets, while in the cerebellum a much lower maximum value of 1.1 mV/cm is reached (Table 4.3). The values for the two DLPFC configurations hardly differ, but the surface area where at least 75% of this value is reached ( $A_{75}$ ) is much larger for the dual DLPFC configuration, showing that this configuration is less focal. The

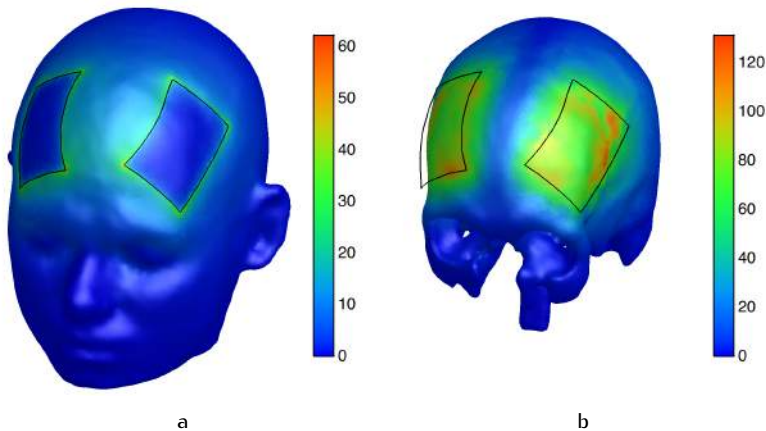


**Figure 4.5** Electric field strength  $|\vec{E}|$  (mV/cm) on the surfaces of the a) skin and b) skull for dual DLPFC stimulation (configuration B). The black outlines indicate the positions of the electrodes on the skin. Distributions for the other targets showed similar patterns.

**Table 4.3** Quantitative results of simulating 1 mA tDCS for six configurations.

Target area		$ \vec{E} _{\text{mx}}^{\text{S (a)}}$ (mV/cm)	$A_{75}^{\text{(b)}}$ (cm <sup>2</sup> )	$I^{\text{T (c)}}$ (μA)	$ \vec{E} _{\text{mx}}^{\text{V (d)}}$ (mV/cm)	$ \vec{E} _{\text{mx}}^{\text{T (e)}}$ (mV/cm)	$ \vec{E} _{\text{mn}}^{\text{T (f)}}$ (mV/cm)	$\vec{E} \cdot \hat{n}_{\text{mn}}^{\text{T (g)}}$ (mV/cm)
A	M1	2.9	7.3	3.0	2.9	2.1	1.4	1.2
B	DLPFC	2.7	10	2.4	3.3	1.7	1.3	0.87
C	DLPFC	2.8	5.7	2.4	3.1	1.7	1.2	0.86
D	IFG	2.4	6.7	2.6	2.7	1.7	1.1	0.86
E	occipital cortex	3.2	1.9	1.5	3.4	1.5	0.85	0.55
F	cerebellum	1.1	1.5	1.9	1.2	0.88	0.75	0.71

<sup>(a)</sup>Maximum electric field strength on the brain surface.

<sup>(b)</sup>Surface area where 75% of the maximum surface value is reached.

<sup>(c)</sup>Current entering the brain surface at the target location.

<sup>(d)</sup>Maximum electric field strength in the brain volume.

<sup>(e)</sup>Maximum electric field strength in the target volume.

<sup>(f)</sup>Mean electric field strength in the target volume.

<sup>(g)</sup>Mean electric field strength perpendicular to the GM surface.

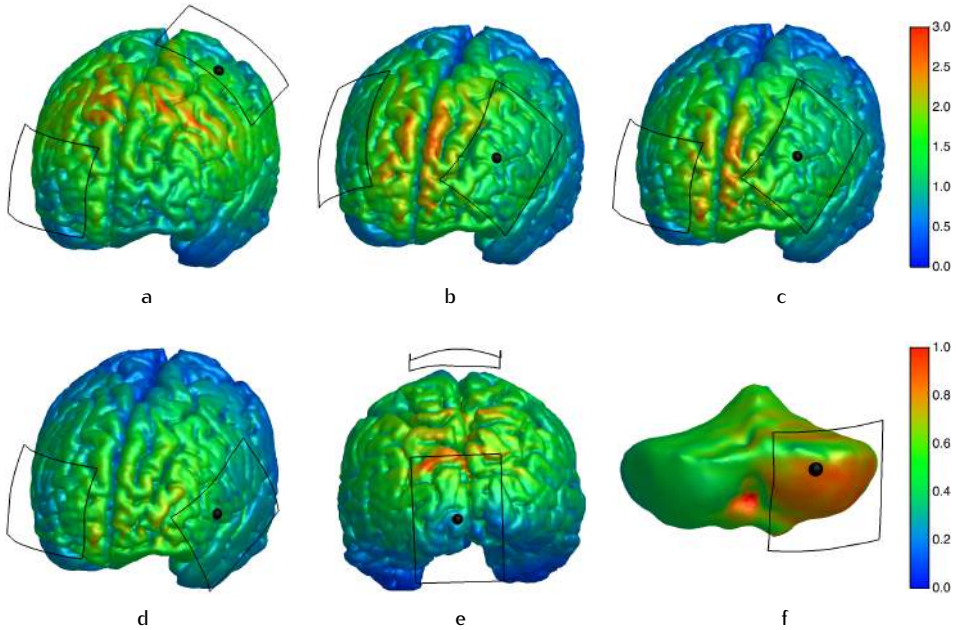


**Figure 4.6** Electric field strength  $|\vec{E}|$  (mV/cm) on the surface of the GM for a) M1, b) dual DLPFC, c) DLPFC, d) IFG and e) occipital cortex stimulation, and on the surface of the cerebellum (f). Scales are adjusted (same scale for figures a-e, shown at top right); actual maxima can be found in Table 4.3. The electrode-skin interfaces are outlined in black and the stimulation targets are indicated by black dots. The occipital anode and target (e) were centered on the midline of the head, but due to the asymmetry in the subjects brain, the target lies on the left hemisphere of the GM surface.

occipital cortex configuration leads to the largest maximum value and the smallest area receiving this field strength, showing a spatially sharp development of the high peak current. This configuration also leads to the smallest amount of current entering the GM at the target location ( $I^T$ ).

### Volume

For the cerebral targets, maximum electric field strengths ( $|\vec{E}|_{\text{mx}}^V$ ) between 2.7 and 3.4 mV/cm are reached in the brain (Table 4.3). The maximum field strength reached in the cerebellum is 1.2 mV/cm.

Electric field strength distributions for separate distance ranges to the target were constructed for the brain (Fig. 4.7a) for configurations A-E and for the cerebellum for configuration F (Fig. 4.7b). For all frontal and motor targets (configurations A-D) distributions were relatively similar: closest to the target (first ribbon in Fig. 4.7a)

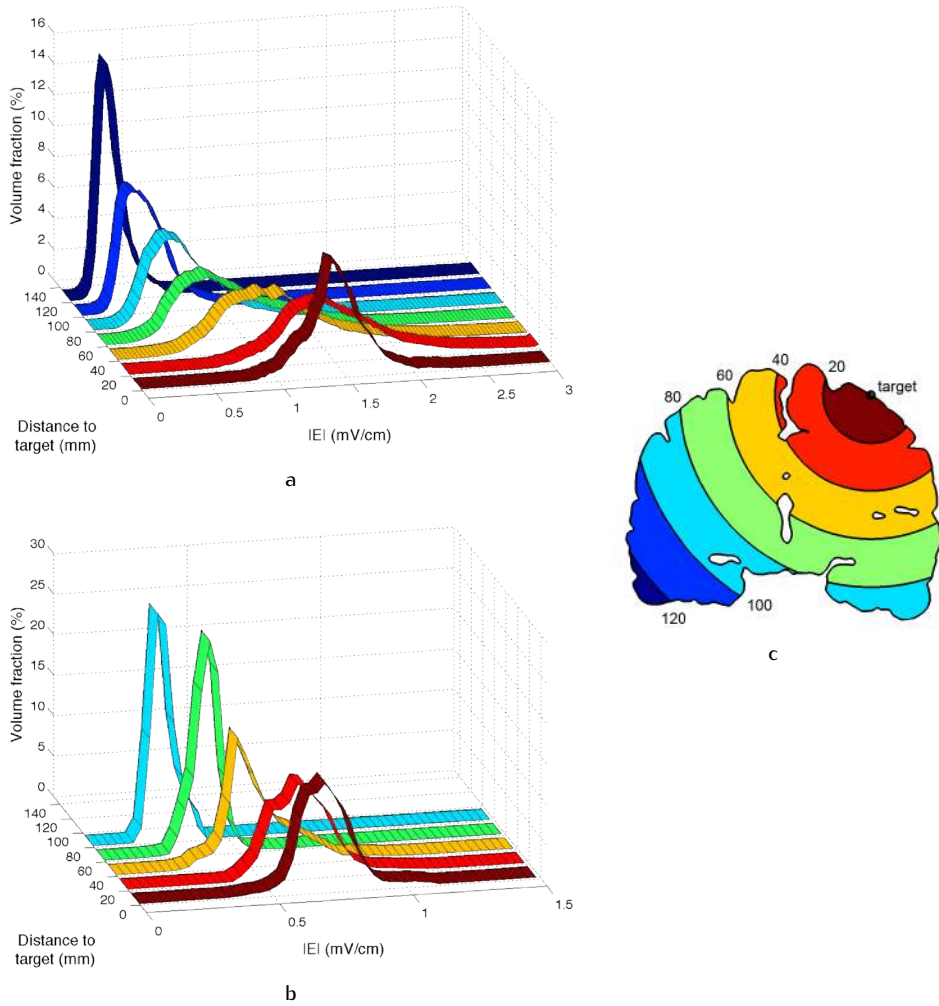


**Figure 4.7** Distribution of electric field strengths  $|\vec{E}|$  (mV/cm) at various distances to the target. a) Cerebral fields for DLPFC-SOA stimulation. Results for other cerebral targets were similar. b) Cerebellar fields for cerebellum-cheek stimulation. c) Schematic of the analysis. All elements in the brain (a) or cerebellum (b) were divided into subsets based on the distance of their centers to the target (shown in millimeters) and a histogram was made of the electric field strengths in each subset. The volumes of the elements were used to scale the distributions. Each histogram (per distance range) sums to 100%. The colors in the schematic correspond to the colors in the histograms.

there is a sharp peak of high electric field strengths; further away from the target the distributions become broader and the peaks lie at lower values of  $|\vec{E}|$ . At the largest distance to the brain (last ribbon in Fig. 4.7a) a sharp peak can be seen at low  $|\vec{E}|$  values. Thus, close to the target mostly high values are found, far away mostly low values are found, and in between there is a wide range in the electric field strength. For all frontal and motor targets, the highest field strengths are found at 20–40 mm from the target (note how the second ribbon spreads to higher values than all others do).

For occipital cortex stimulation the peaks of the distributions at all distances are similar, except for a sharp peak at the largest distance. In the cerebellum the distributions are much narrower than for the cerebral targets and the peaks lie closer together and at lower values (Fig. 4.7b). This is due to the cerebellum being a much smaller and smoother structure than the brain. Highest electric field strengths are found closest to the target (0–20 mm).

Similar analyses were performed for gray and white matter separately, showing that for M1 and occipital cortex stimulation the peaks of the distributions lie at higher  $|\vec{E}|$  values in white matter than in gray matter. For all other configurations the locations of the peaks do not differ greatly between gray and white matter.

### Target volume

The maximum field strength ( $|\vec{E}|_{\text{mx}}^T$ ) is 0.88 mV/cm in the cerebellar target volume, while in the cerebral target volumes  $|\vec{E}|_{\text{mx}}^T$  ranges from 1.5 mV/cm for occipital cortex to 2.1 mV/cm for M1 stimulation (Table 4.3). For the two DLPFC configurations the maximum values reached in the target volume are 54–55% of the maximum value in the complete brain. For M1, IFG and cerebellum these values are 70%, 62% and 76%, respectively; for the occipital cortex configuration it is only 45%. The average electric field strength in the target volumes ( $|\vec{E}|_{\text{mn}}^T$ ) ranges from 0.75 mV/cm for cerebellum to 1.4 mV/cm for M1 stimulation. The average electric field strength perpendicular to the GM surface ( $\vec{E} \cdot \hat{n}_{\text{mn}}^T$ ) ranges from 0.55 mV/cm for occipital cortex to 1.2 mV/cm for M1 stimulation. While cerebellar stimulation resulted in relatively low values in several other analyses, the result for  $\vec{E} \cdot \hat{n}_{\text{mn}}^T$  is similar to that for the other configurations. The simulated electric field in the cerebellar target volume is mainly directed perpendicular to the GM surface, leading to a high  $\vec{E} \cdot \hat{n}_{\text{mn}}^T$ .

## 4.4 Discussion

---

The study in this chapter presented simulations of 1 mA tDCS in a highly detailed volume conduction model for six commonly used electrode configurations.

### General results

Highest electric field values in the skin were found along the rim of the electrodes, as was reported in other studies<sup>[98,160]</sup>, but here it was also shown that the electric field distribution on the skull surface is high under the complete area of both electrodes and that a shift of the maximum away from the electrodes occurs only at brain level. As the current follows the path of least resistance, it is understandable that most current flows from the stimulator towards the edges of the electrodes to the skin instead of radially through the poorly conducting skull. A large part of the current goes from anode to cathode through the skin without passing the skull and thus never enters the brain. The current that does enter the skull spreads itself over its surface under the electrodes. When the current enters the CSF, it is transported through this highly conductive fluid away from the anode, leading to a wide distribution of the electric field on the brain surface. As there was only one area of maximal stimulation on the brain surface instead of one under each electrode, this relieves possible worries for unwanted stimulation effects at the cathode. The results suggest that the dimensions of the area of maximum field strength are determined by the length of the electrode edges that are facing each other. It thus seems possible to increase focality without changing the electrode size, simply by placing the electrodes with the short sides facing each other.

### Cerebral targets

Five configurations were simulated for four cerebral targets: left motor cortex, left dorsolateral prefrontal cortex, left inferior frontal gyrus and occipital cortex. For all cerebral targets large areas of near-maximal field strength were found far away from the targets. Highest values were found 20–40 mm from the target, in between the anode and the cathode. Electric field strengths of more than twice the maximum value in the target volume are found in other brain areas. Not only is the target area not stimulated maximally, also other cerebral areas are stimulated much more strongly. Similar modeling results have been presented for M1 stimulation<sup>[33,68]</sup> and for occipital cortex stimulation in a stroke patient<sup>[58]</sup> using isotropic models. The results from the anisotropic model presented here agree with these findings and

show that also the conventional configurations for DLPFC and IFG do not maximally stimulate their respective targets. Moreover, these results suggest that the common practice of placing electrodes over the target area leads to suboptimal field strengths.

Both DLPFC configurations lead to very similar results, not only at the targeted DLPFC, but also in the complete brain volume. Only the surface area  $A_{75}$  shows a large difference. The similar results for the two DLPFC configurations show that a small displacement of the return electrode for this target does not have a large influence on the resulting electric field.

In modeling studies it is common to report the value and surface area of maximum field strength. The results in this chapter indicate that in most cases these measures are not useful to determine effectivity and focality of a configuration. For example, the occipital cortex configuration produced the highest field strengths and the most focal stimulation, while its effects in the targeted area were the smallest. For future modeling studies, it is therefore more useful to evaluate the electric field in a target volume.

## Cerebellum

The configuration for cerebellum stimulation tested in this study resulted to be the only configuration that achieves relatively high electric field values at its target site. The actual maximum lies elsewhere, due to high local curvature, nevertheless the configuration seems near-optimal. The maximum of the electric field at the cerebellar surface is much lower than for the cerebral targets. This is probably due to large currents ducking inferiorly under the skull and flowing through the skin to the cheek. The occipital cortex configuration also leads to low values in its target volume and a low inward current, while high values are achieved elsewhere. These results suggest that placing an electrode on the back of the head generally leads to large amounts of shunting. To achieve comparable field strengths in the cerebellum as reached with the other configurations, the input current for cerebellar stimulation should be doubled. In practical applications, most studies do use 2 mA tDCS for cerebellar stimulation<sup>[54,71,60]</sup>.

## Direction of the electric field

The above discussion focuses on areas of highest field strength, as is common in tDCS modeling studies<sup>[33,113,68]</sup>. In practice, the effects of stimulation might actually be higher in a different area, because the orientation of the field might have more significant effects than does the strength. The possible importance of field direction



is already obvious from the fact that experiments have shown opposite effects of anodal versus cathodal tDCS (Section 1.1.3). For this reason, a measure of field directionality was analyzed in this study.

It was found here that the conventional configurations lead to maxima in field strength outside the target area. However, experimentally all these configurations have been shown to affect their targets. This could mean two things. As described above, if field strength is the most important parameter, then other areas are stimulated more strongly than the target is. One would expect this to result in significant side-effects, something that has not been reported for tDCS. The other possibility is that electric field strength is not the parameter of interest. It was shown here that for the conventional configurations a large part of the field is directed perpendicularly inward with respect to the GM surface. The perpendicular field strength was analyzed in the areas of maximal absolute field strength (results not shown) and in these areas (i.e. the red areas in Fig. 4.6) the perpendicular field strength is much smaller than under the electrodes. The results for perpendicular field strength thus agree better with the experimental findings than the results for absolute field strength. Therefore, the direction of the field should be taken into account in future modeling studies. In order to better evaluate tDCS models, more knowledge on the effects of the fields direction versus its strength is needed.

### Realistic modeling

In modeling tDCS, and other stimulation modalities in general, the ultimate goal would be to efficiently create individualized FE models with the highest amount of accuracy. Due to the complicated nature of creating realistic tetrahedral anisotropic head models, this process is too time-consuming to create individual models. Simply converting an MRI scan directly into an isotropic hexahedral model is a fast method that does allow for individualized models, but as these models do not have smooth tissue boundaries nor include tissue anisotropy, detail is sacrificed for the sake of time. The goal of this study was to provide for one model the most accurate predictions possible. The detailed description of the model creation process presented in this chapter, a scheme that consists almost completely out of freely available software, can guide other investigators in creating similar models and extend the current knowledge base.

Although the model presented here contains much detail, shortcomings do surely exist. To prevent gray matter and skull surfaces intersecting, the brain of the model had to be slightly scaled down, leading to a slightly enlarged CSF volume. Also, the model does not include air compartments. The rather large pockets of nonconducting air formed by the frontal sinuses could alter the results for configurations with

an electrode over the supraorbital area. Because the sinuses were modeled as highly resistive compacta, the conductivity was relatively close to the real value. Also, as current from a large electrode mostly flow through the corners closest to the other electrode, the main current flow occurs above and not over the sinuses for the configurations studied here. Therefore it is not expected that including air compartments would have significantly affected the results.

Simplifications were made in areas that were not expected to affect the results. The mouth and jaws were modeled as skin and thus in a real head these areas have a lower conductivity. As both electrodes are far away from this area for all configurations aimed at cerebral targets, this should not significantly alter the current flow in areas of interest. This assumption was tested by making the mouth area of the model non-conductive and repeating the simulations. For M1 stimulation, this resulted in a 1% increase in field strength both in the target area and in the complete brain. Even for cerebellar stimulation, where one electrode is located near the mouth, the differences were small: 1% in the target area and 2% in the cerebellum overall. These results show that a lack of detail in the mouth area does not significantly affect simulation results.

Models exist that explicitly represent small structures like eye sclera and blood vessels<sup>[113,141]</sup>. As it is nearly impossible to create closed surface meshes of such small structures, using a tetrahedral model almost automatically excludes them. This immediately leads to the question if such small structures could actually significantly affect simulations. This hypothesis was tested by using a change in the conductivity of the smallest structure in the model as a representation of adding an even smaller structure with a different conductivity. Changing the conductivity of the eyes from 0.4 S/m<sup>[32,58]</sup> to 1.5 S/m<sup>[102]</sup> for M1 stimulation leads to a change in the electric field strength of 0.6% in the target volume and 0.6% in the brain overall. This shows that the influence of small structures is only marginal and negligible compared to other unavoidable small modeling errors.

Most tDCS models do not include the neck muscles. Because cerebellar stimulation might be affected by these muscles, they were included in the model presented here. Unfortunately, there is a large spread in the muscle conductivity values reported in literature, especially when the anisotropic nature of muscle tissue is taken into account<sup>[52,53,39]</sup>. To test the influence of these differences, simulations with the cerebellar configuration were compared using muscle conductivities at the edges of this range. Using a muscle conductivity of 0.16 S/m leads to an increase of 11% in the mean field strength in the target volume and 10% in the cerebellum overall, as compared to using 0.4 S/m. This shows that simulations of cerebellar tDCS could be improved by acquiring more knowledge on the conductivity of muscle tissue.

### Improved electrode placement

Based on the combined findings of all targets in this study, the hypothesis was established that an electrode pair should be centered around the targeted area for optimal field strength. By developing and simulating new configurations based on this notion, several were found that perform better than the conventional configurations do (results not shown). Next efforts are towards more precise substantiation of this hypothesis through optimization. The findings in this chapter also suggest that field strength perpendicular to the GM surface should be optimized as well. In this study the concept of a meshed target volume was introduced to provide quantitative measures for the effectivity of stimulation and these analyses were successful in expressing a configurations ability to stimulate the target. Because these analyses allow for objective evaluation without the need for visual inspection, these methods are especially valuable for comparing large numbers of configurations for optimization purposes. The effectiveness of such theoretically improved configurations could then be tested by comparing them with their respective conventional configurations in an area-specific task or through measurements of cortical excitability.

## 4.5 Conclusions

---

From the results of this study it can be concluded that 1) based on field strength, all five cerebral stimulation configurations studied here are not suited for their targets, 2) the commonly used configuration for cerebellum stimulation performs relatively well, 3) cerebellum stimulation needs higher input currents than does cerebral stimulation and 4) the direction of the field should be considered in future studies. These results suggest space for improvement in the application and outcomes of tDCS and an important role for modeling in achieving these goals.





## Chapter 5

# Optimization of electrode placement



Based on: *Model-based optimization of bipolar tDCS electrode placement*, by Sumientra Rampersad, Dick Stegeman and Thom Oostendorp, submitted for publication.



## 5.1 Introduction

---

Though positive results of tDCS are numerous and promising, the effects are sometimes rather small or short-lived and striving for improvement is indicated. Modeling studies have shown that with the commonly used configurations for motor and occipital cortex stimulation, maximal electric field strengths are reached in areas other than the target<sup>[33,68,58]</sup>. In the previous chapter, tDCS simulations were presented for six conventional configurations targeting five brain areas. For all cortical targets the maximal electric field strength was found roughly midway between the electrodes instead of in the target area. These results suggest that the effects of tDCS might be improved by better targeting of the current using new configurations.

Several studies have described approaches to find improved configurations for tDCS. These studies optimized the resulting electric field using small circular electrodes<sup>[67,116,36]</sup> and/or multi-channel stimulation patterns<sup>[36,141]</sup> for 1–3 target areas in the brain. An improved configuration of two large electrodes, the most widely available setup of tDCS in practice, has only been provided for one cortical target<sup>[141]</sup>. Brain anisotropy was only included in one model<sup>[141]</sup> and one study investigated the direction of the field<sup>[36]</sup>. Electrodes below the ears were not considered.

This chapter presents optimizations of tDCS with two large electrodes based both on the resulting field strength and on the field direction for six common target areas. This was achieved by calculating the electric field for a large set of bipolar configurations covering the complete head; the results were evaluated in target volumes in the brain and compared for all configurations. Through this method, bipolar configurations were found that lead to a maximal field strength in the M1, DLPFC, IFG, occipital cortex and cerebellum, the areas most commonly targeted in tDCS research for a wide range of applications (Table 1.1). In addition, the prospect that only the component of the electric field directed parallel to the neuronal fibers is of influence<sup>[138,127]</sup> was considered. The configurations that maximized this property in the target area were found as well.

Instead of providing *the* optimal configuration for each target area, clusters of optimal configurations will be presented through visual representations. In this way, more configurations are provided that, though sub-maximal, still perform much better than the conventional configurations do and might be practically favorable for certain applications. More importantly, these visual representations show patterns in the results that allowed the deduction of general recommendations for electrode placement.



## 5.2 Methods

---

After a realistic FE head model had been constructed (Section 4.2), a grid of points was placed on its surface based on the international 10-10 system of standardized electrode placement<sup>[26]</sup>. For every combination of two points, electrodes were built onto the model surface and tDCS was simulated. The resulting electric fields of all simulations were evaluated and compared in a target volume in the brain for each of six target areas. The configurations resulting in the highest absolute field strength, or highest optimally directed field strength, in each target area were selected. Finally, the performance of the optimized configurations was compared with the results of the conventional configurations.

### Target areas

Six brain areas were selected for optimization based on recent literature (Table 5.1). Additional to the five target areas researched in Chapter 4, tDCS was optimized for the leg area of the primary motor cortex. The M1 leg area is a less common target for tDCS, but was selected because of its location on the interior section of the motor cortex. As the other cerebral targets all lie on gyri close to the skull, a target area inside the medial longitudinal fissure will diversify the set of targets.

The target areas were located on the GM surface of the model for analysis and comparison of the results. The left M1 leg area, DLPFC and IFG were identified in the model using anatomical landmarks. The target for occipital stimulation was placed in the occipital cortex approximately 1 cm left of the longitudinal fissure. The locations of the M1 hand area and cerebellar target were obtained by projecting the corresponding locations on the scalp of the model (described below) onto their respective GM surfaces.

The conventional configurations for these brain areas were simulated so that their performance could be compared to that of the optimized configurations. Because the optimization process was based on the international 10-10 system, the conventional tDCS electrode locations were converted to this system where possible (Table 5.1). The remaining locations were identified on the model by other means. The location of the cerebral representation of FDI muscle of the right hand was experimentally determined on the scalp of the volunteer on which the model was based via TMS and EMG (Section 4.2.2). The electrode location for IFG stimulation was obtained by projecting the GM target onto the skin surface. For cerebellar stimulation, the target electrode was placed with its center 3 cm right of theinion and the cathode

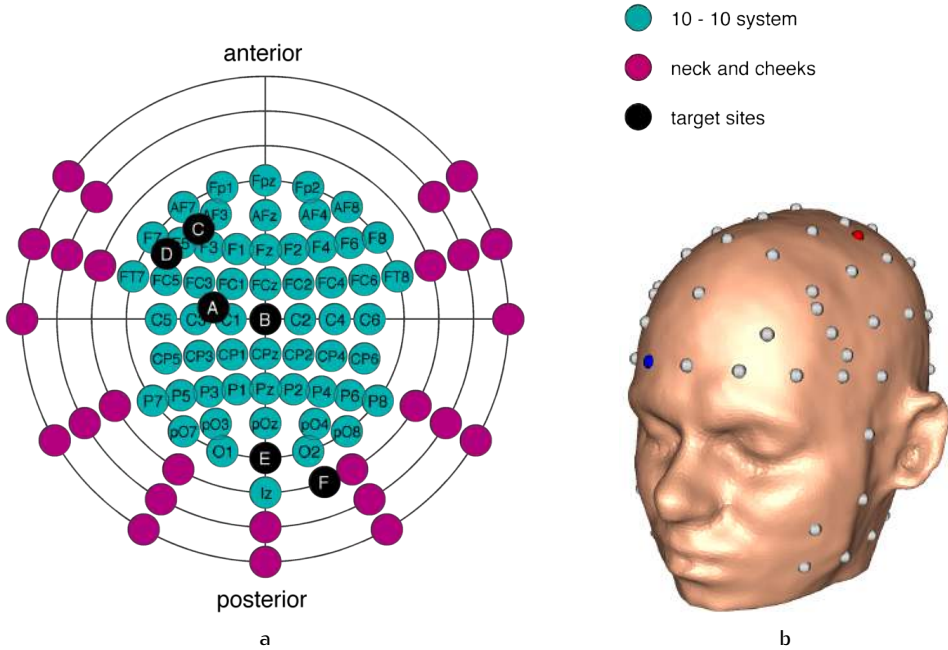


**Figure 5.1** Grid of electrode center locations. (a) Schematic representation created for displaying the results. (b) Points on the head model. The green points were placed according to the international 10-10 system for standardized electrode placement. Points were added to cover the neck and cheeks (pink) and for the target locations (black). A: M1 hand; C: DLPFC; D: IFG; F: cerebellum. The targets for the M1 leg area (B) and the occipital cortex (E) correspond to the Cz and Oz locations, respectively.

was placed on the middle of the right cheek.

### Simulated configurations

The locations of the international 10-10 system of standardized electrode placement on the head model were calculated using custom code. As these points were to be used as centers of 25 cm<sup>2</sup> electrodes, all points that would lead to electrodes partly covering the face or ears were removed, resulting in a set of 58 points (Fig. 5.1b, green spheres). A schematic representation of the 10-10 system was adapted to represent the electrode grid used in this study (Fig. 5.1a).

The cheeks and neck of the model were covered with 26 approximately equally-spaced points in line with the points from the 10-10 system (Fig. 5.1, pink spheres). The resulting total set of 84 points covers the complete head. Taking into account the size of the electrodes and the low focality of tDCS, this set includes all relevant

electrode center locations on a complete head (i.e. adding more points would be oversampling). Lastly, the conventional electrode locations that were not yet part of the grid were added.

The complete grid of electrode locations thus contained 88 points. Each point served as the center of a 5 x 5 cm electrode. This size was chosen because it is a commonly available electrode and it is the closest to the also often-used size of 5 x 7 cm with minimal orientation ambiguity. The electrodes were placed parallel to the bottom of the model (examples in Figure 5.1). Any combination of two points from the grid was a possible configuration. In case two electrodes touched, they were rotated to reduce overlap. If overlap was inevitable, the combination was discarded. This resulted in a total of 3561 unique configurations. For each configuration, the anode and cathode were assigned randomly. As tDCS simulation is a linear process, the configuration with reversed polarity does not have to be modeled explicitly; the resulting electric field can be produced by flipping the vectors of its counterpart.

## Computations

For each configuration, two electrodes were built onto the head mesh as rectangular patches with a height of 3 mm and the conductivity of saline (1.4 S/m) (Figure 5.1c). The nodes in the top layer of the anode were assigned a potential of  $+\phi_0$  and those in the top layer of the cathode  $-\phi_0$ , with  $\phi_0$  chosen such that the total current entering the skin was equal to 1 mA. Laplace's equation (Eq. 1.5) with Neumann boundary conditions at the skin surface outside the electrodes and Dirichlet boundary conditions on the surfaces of the electrodes (Eq. 1.6) was solved with SCIRun 4.6<sup>a</sup> using a conjugent gradient solver and Jacobi preconditioner with a maximal residual of  $10^{-10}$ . These calculations resulted in a potential  $\phi$  at each node of the mesh, from which the electric field  $\vec{E} = -\nabla\phi$  was calculated in each element. For one configuration, the complete process took approximately 6 minutes on a Mac Pro computer with 16 GB RAM, of which 1 minute was used by the solver and the remainder for the construction of the electrodes onto the base model and other calculations.

## Analysis

In order to evaluate and compare the effects of different configurations in the targeted area, an evaluation brain volume was selected at each target location (Fig. 4.4). A cylindrical mesh with a 1 cm<sup>2</sup> base and 4 mm height was placed at the target location adjacent to the gray matter surface, with its axis perpendicular to it. All GM

---

<sup>a</sup>Scientific Computing and Imaging Institute, Salt Lake City, UT, USA.

**Table 5.1** The target areas in the brain for which tDCS was optimized in this study and their conventional electrode configurations. These configurations are commonly used for a wide range of applications (Table 1.1, p. 10). The electrode locations are expressed as points of the conventionalized 10–10 system for electrode placement, where possible. For excitative stimulation the target electrode is given a positive potential with respect to the reference; reversing the polarity would induce inhibition.

	Target area	Target electrode	Reference electrode
A	motor cortex (M1) hand area	left M1 FDI <sup>(a)</sup>	Fp2
B	motor cortex leg area	Cz <sup>(b)</sup>	Fp2
C	dorsolateral prefrontal cortex (DLPFC)	F3	Fp2
D	inferior frontal gyrus (IFG)	left IFG	Fp2
E	occipital cortex	Oz	Cz
F	cerebellum	right cerebellum	right cheek

<sup>(a)</sup>Cortical representation of the right first dorsal interosseus muscle.

<sup>(b)</sup>The cortical representation of the tibialis anterior muscle is also often used and is close to Cz.

**Table 5.2** Maximal absolute field strength ( $E_a^{\text{mx}}$ ) and maximal field strength in the preferred direction ( $E_n^{\text{mx}}$ ) reached in six target volumes by optimization. The results for the conventional configurations,  $E_a^c$  and  $E_n^c$ , and the relative change (as  $(E^{\text{mx}} - E^c)/E^c \cdot 100$ ) are presented as well.

Target	$E_a^{\text{mx}}$ (mV/cm)	$E_a^c$ (mV/cm)	Change (%)	$E_n^{\text{mx}}$ (mV/cm)	$E_n^c$ (mV/cm)	Change (%)
A M1 hand	2.9	1.4	105	1.5	1.2	19
B M1 leg	2.0	1.2	74	0.98	0.21	375
C DLPFC	2.8	1.3	119	1.1	0.99	14
D IFG	2.4	1.1	110	1.2	0.91	35
E occipital cortex	2.2	1.0	115	0.80	0.69	16
F cerebellum	1.9	0.84	126	0.96	0.80	21

elements within this cylinder were selected as the target volume at this location. It is common in tDCS modeling to use the absolute electric field strength  $|\vec{E}|$  as output variable. The mean field strength in the target volume<sup>a</sup> is defined here as  $E_a$ . This value was calculated for all simulated configurations and the maximum value of  $E_a$  among all configurations ( $E_a^{\text{mx}}$ ) was found for each target. All configurations with  $E_a > 90\%E_a^{\text{mx}}$  will be considered.

A second analysis method was devised in order to optimize the field strength in the most effective direction. Assuming that the effect of stimulation is highest if the electric field is directed parallel to the fibers<sup>[138,127]</sup> and that GM neurons lie perpendicular to its surface<sup>[62]</sup>, the mean electric field strength normal to the GM surface was calculated. For each element in a GM target volume, the scalar product of the electric field vector ( $\vec{E}$ ) with the vector normal to the closest GM surface triangle ( $\hat{n}$ ) was calculated. The mean value of  $\vec{E} \cdot \hat{n}$  within the target volume<sup>b</sup> is defined here as  $E_n$ . As the normal to the GM surface was defined as pointing inward, this value represents the mean electric field strength in the presumably most effective direction for excitative stimulation in the target volume. This direction will from here on be called the *preferred* direction. For each target, the maximum value of  $E_n$  among all configurations ( $E_n^{\text{mx}}$ ) was found and all configurations with  $E_n > 90\%E_n^{\text{mx}}$  will be presented. Optimization of field strength in the preferred direction will from here on be referred to as *direction-based* optimization.

## 5.3 Results

The optimal tDCS electrode configurations for six target areas in the brain are presented here for strength- and direction-based optimization separately.

### Strength-based optimization

For the M1 hand area the highest mean field strength achieved in the target area ( $E_a^{\text{mx}}$ ) was 2.9 mV/cm (Table 5.2). With respect to the conventional configuration ( $E_a^c$ ), this corresponds to an improvement of 105%  $((E_a^{\text{mx}} - E_a^c)/E_a^c * 100)$ , meaning that field strength in the target area was more than doubled through optimization. While the field strength distribution on the GM surface has its maximum in between the electrodes for the conventional configuration (Fig. 5.2a), optimization clearly leads to a maximum in field strength at the target location (Fig. 5.2b). Also, the maximum field

<sup>a</sup>This value was defined as  $|\vec{E}|_{\text{mn}}$  in Chapter 4.

<sup>b</sup>This value was defined as  $\vec{E} \cdot \hat{n}_{\text{mn}}$  in Chapter 4.

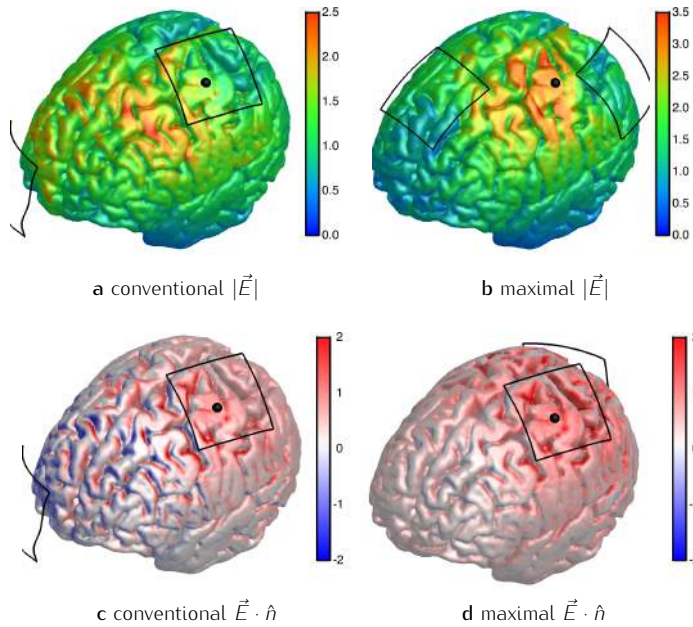


**Figure 5.2** Electric field distributions on the GM surface for hand motor cortex stimulation. The figures on the top show electric field strength ( $|\vec{E}|$ ) and the figures on the bottom electric field strength perpendicular to the GM surface ( $\vec{E} \cdot \hat{n}$ ), both in mV/cm. The figures on the left show the results for the conventional configuration (FDI-Fp2). On the right configurations are shown that lead to maximal field strength (b: CP3-Fz) or maximal field strength in the preferred direction (d: FDI-pO4) in the target area. In the bottom plots, red indicates that the electric field is directed in the preferred direction for excitative stimulation, i.e. perpendicularly into the GM surface, and blue indicates that the field is pointing in the opposite direction.

strength is higher. For all superficial targets (i.e. all but M1 leg), the field strength in the target volume can at least be doubled by optimization: the improvement from the conventional configurations is 105-126% (Table 5.2). For the leg area of M1 the maximal increase is 74%.

The results for strength-based optimization are presented graphically in Figure 5.3 using a schematic of the electrode locations (Fig. 5.1). Each line connecting two circles represents a configuration of two electrodes. The red lines represent the conventional configurations (Table 5.1) and the large red circles the locations of the targets. The blue lines represent the sets of optimal configurations. Configurations that produced results above 90%, 95% or 99% of  $E_a^{\text{mx}}$  are displayed with increasingly bolder and darker blue lines. The corresponding values of  $E_a$  for each set can be found using the  $E_a^{\text{mx}}$  values in Table 5.2. As the direction of the field is not taken into account in strength-based optimization, a distinction between anode and cathode

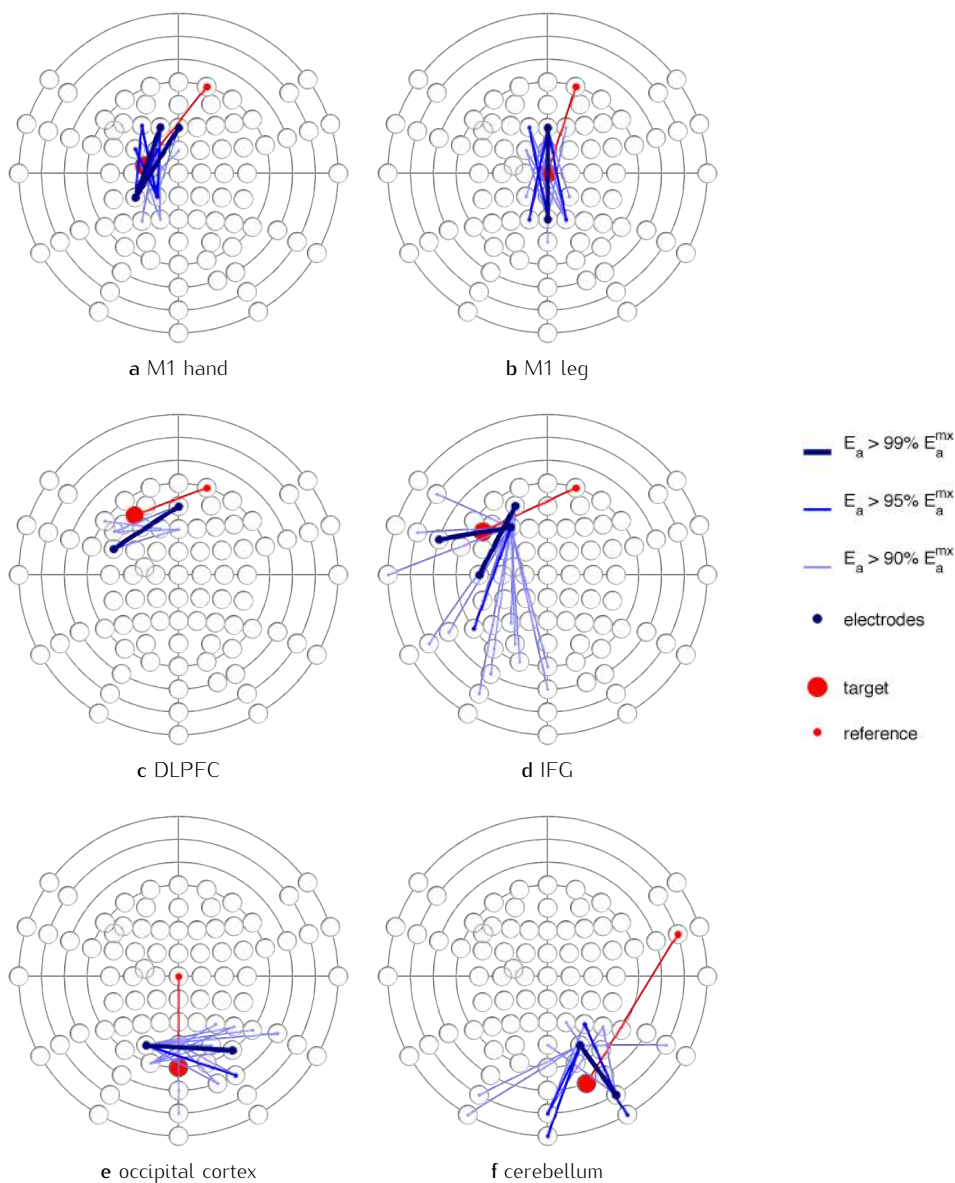


**Figure 5.3** Optimal tDCS electrode configurations for maximal absolute electric field strength in the target volume ( $E_a$ ). Configurations producing results above 90%, 95% and 99% of the highest value of  $E_a$  found among all configurations ( $E_a^{mx}$ ) are represented by increasingly bolder and darker blue lines on a schematic representation of the electrode grid (for details on this grid, see Fig. 5.1). The conventional configurations (Table 5.1) are shown in red.

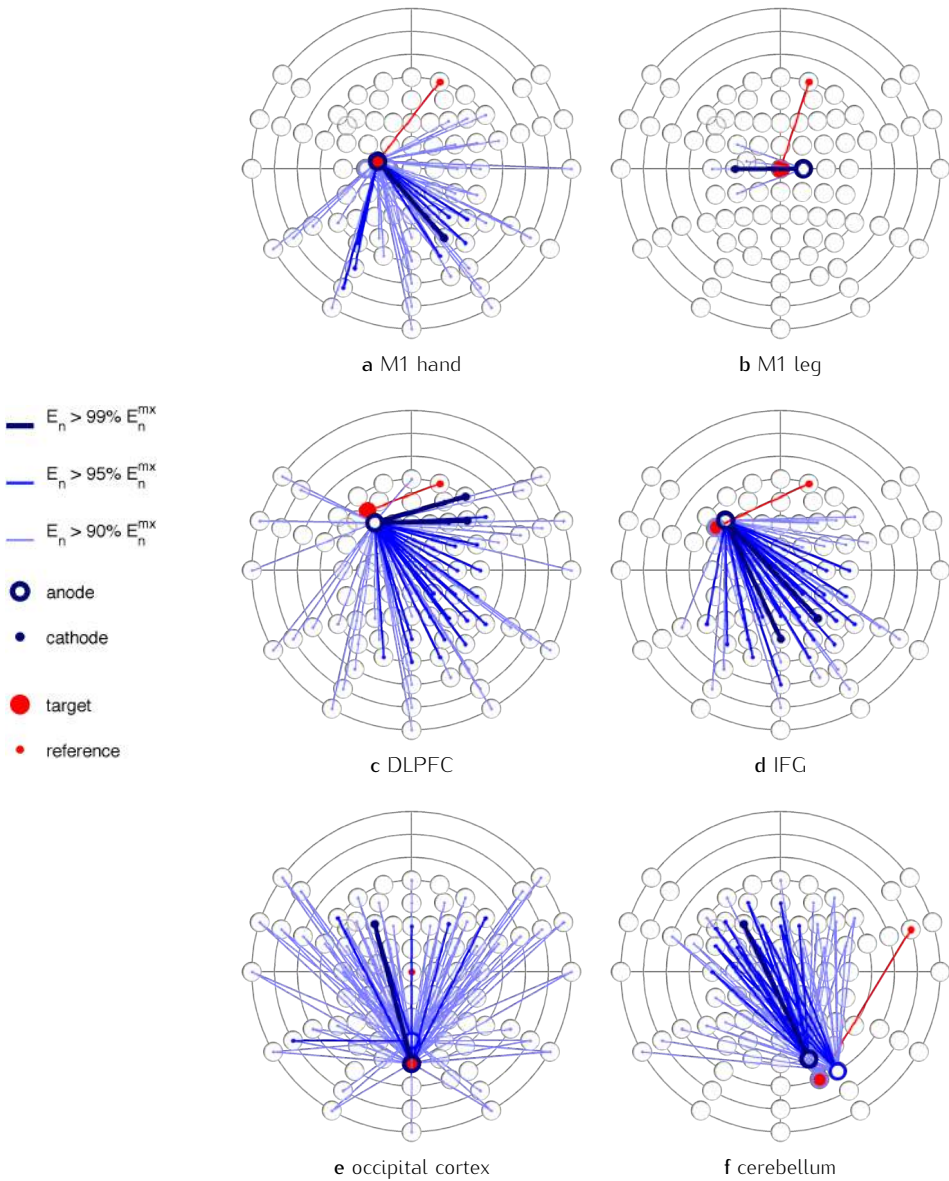


**Figure 5.4** Optimal tDCS electrode configurations for maximal field strength in the preferred direction in the target volume ( $E_n$ ). Configurations producing results above 90%, 95% and 99% of the highest value of  $E_n$  found among all configurations ( $E_n^{\text{mx}}$ ) are represented by increasingly bolder and darker blue lines on a schematic representation of the electrode grid (for details on this grid, see Fig. 5.1). The conventional configurations (Table 5.1) are shown in red.



cannot be made here.

For all targets the configurations with  $E_a > 99\%E_a^{\text{mx}}$  consist of electrodes close to the target area and on opposite sides (Fig. 5.3). The few configurations with  $E_a > 95\%E_a^{\text{mx}}$  strongly resemble the first set. The sets with  $E_a > 90\%E_a^{\text{mx}}$  are larger (i.e. more configurations) and mostly similar. Almost all configurations have one electrode in common with a configuration of the first set. For the M1, DLPFC and occipital target areas all configurations are similar, while for the IFG and cerebellum the possible electrode locations spread out more for lower intensities. By visualizing more sets with decreasing results (e.g.  $E_a > 85\%E_a^{\text{mx}}$ ; not shown for clarity) the same pattern was found for all targets: the distance of the electrodes to the target area increases for lower limits of  $E_a$  and the range of angles between the configuration lines increases as well. The latter is not true for the leg area of M1: all configuration lines are directed approximately along the midline even for  $E_a > 80\%E_a^{\text{mx}}$ .

### Direction-based optimization

The maximal improvement in optimally directed field strength in the target area with respect to the conventional configuration was 19% for the M1 hand area (Table 5.2). The electric field strength in the preferred direction is presented as  $\vec{E} \cdot \hat{n}$  on the GM surface for the conventional M1 configuration (Fig. 5.2c) and the configuration that produced the maximal  $E_n$  (Fig. 5.2d). As we are optimizing excitative stimulation and thus maximizing the inward-directed field, optimal values should be maximally positive (bright red). The optimal configuration indeed leads to a slightly better directed electric field at the target location than does the conventional configuration. The improvement in field strength in the preferred direction is 14–35% for all superficial targets (Table 5.2). For the M1 leg area  $\vec{E} \cdot \hat{n}$  is relatively low for the conventional configuration. After optimization, similar values as compared to the other targets are reached and consequently a large relative improvement (375%).

The results for direction-based optimization are presented graphically in Figure 5.4, with the anodes represented by circles and the cathodes by dots. The configurations shown here are optimized for excitative stimulation; for inhibitive stimulation, the polarity of the electrodes should be reversed. For all superficial targets the configurations with  $E_n > 99\%E_n^{\text{mx}}$  consist of an anode on or close to the target site and a cathode further away. Decreasing the limit for  $E_n$  adds large numbers of similar configurations with only a few possible anode positions and the cathode at an increasing number of possible locations at increasing distance and different directions from the target. The results are different for the leg area of M1: only a few configurations lead to high values of  $E_n$ . Each of these configurations has its anode to the right of the target and its cathode to the left.

## 5.4 Discussion

An extensive modeling approach was used to find optimal bipolar configurations for transcranial direct current stimulation of six commonly targeted areas in the brain. Optimizations were performed based on two criteria: electric field strength and field strength in a preferred direction. Sets of optimal configurations for both conditions were provided and compared to the conventional configurations. Visual judgement of the electric field distribution on the brain confirmed that these optimal configurations indeed have their maximum at the intended target. The data set produced for this study can be used to optimize tDCS for any target area in the complete brain. However, as will be discussed below, the demonstrated patterns and the related findings of this study allow for a generalization to other cortical target areas and, more importantly, to other brain morphologies.

### Strength-based optimization

A general trend in the results was seen for all targets. From this a conclusion follows: in order to reach maximal electric field strength in the target area, the electrodes should be placed on opposite sides close to the target. High field strengths can be achieved with a multitude of similar configurations. Placing the electrodes further apart will decrease the target field strength, while the direction of the interelectrode line is less important. As this approach is very different from the conventional method of electrode placement, it is obvious that the conventional configurations were not among the optimal configurations. Also the large improvements achieved here (74–126%) are not surprising considering that most conventional configurations lead to maxima far from their targets (Chapter 4).

The conclusion described in the previous paragraph is valid for all target areas. For some specific cases, there are additional restrictions to the direction of the interelectrode line. The different cases are summarized schematically in Figure 5.5 (left side). Of the six targets studied here, exact placement of the electrodes was crucial only for the leg area of M1: high field strength values were exclusively reached with the electrodes roughly along the midline. With these setups, the highly conductive CSF within the medial longitudinal fissure can conduct large currents to deeper lying areas within the fissure such as the leg area. If electrodes are placed perpendicular to the midline, most of the current flows over the interhemispheric fissure. Therefore, for targets within the interhemispheric fissure (green areas in Figure 5.5), the electrodes should be placed on opposite sides close to the target

*along the midline.*

Similar effects as found for the interhemispheric fissure might occur for target areas that lie within a sulcus. As all targets studied here are located on gyri, this effect could not be demonstrated with these targets. Therefore two additional target areas were created in the walls of different sulci and strength-based optimizations were performed for these areas (results not shown). For both areas, maximal field strengths were found for configurations that line up with the sulcus. The wider and deeper a sulcus is, the stronger is the effect (i.e. persisting for lower limits of  $E_a$ ). From these results a recommendation follows: for sulcul target areas (purple areas in Figure 5.5) place the electrodes on opposite sides close to the target *over the sulcus*. For areas on a gyrus, maximal effects are reached with configurations perpendicular to the sulcus, but this effect is less strong.

### Direction-based optimization

The direction-based optimization results were equivalent for all target areas except for the leg area of M1. This is due to the different orientation of the GM surface with respect to the skull. All superficial targets investigated here are located on a gyrus close to the skull. The GM surface in these areas is tangential to the skull and thus the preferred direction of the field is perpendicular to the skull. The results of this study show that with one electrode over or near the target area, a large part of the resulting electric field is directed perpendicularly inward in the underlying gyrus. As this placement is similar to the conventional method, the improvements achieved were rather small (16–35%), even though for all targets the conventional configurations were not among the optimal sets.

Contrary to the superficial targets, the leg area of M1 lies on a gyrus that is located inside the medial longitudinal fissure. In this case, the GM surface is perpendicular to the skull and the preferred direction of the field tangential. To produce an electric field in this direction, the electrodes need to be placed on opposite sides of the target. It is then understandable that there are only a few near-optimal configurations and that they have a right-left direction. When investigators started stimulating the leg area of M1, they based the configuration on the conventional placement for superficial targets. This results in a similarly inward-directed current that, in this case, is oriented almost perpendicular to the intended direction. For this reason, the  $E_n$  value for the conventional configuration was extremely low and the achieved improvement extremely high.

Based on these findings, one would expect the results for targets lying in a sulcus close to the skull to resemble the results for the leg area, as the GM surface in both locations has the same orientation with respect to the skull (compare pink areas

in Figure 5.5). This hypothesis was tested by performing additional direction-based optimizations for two target volumes in different sulcal walls (results not shown). Indeed, only a few optimal configurations were found for both areas and these consisted of electrodes on opposite sides of the target with the interelectrode line perpendicular to the sulcus.

These results have been condensed into general recommendations for optimal electrode placement that are visualized in Figure 5.5 (right side). In order to maximize field strength perpendicular to the GM surface for targets on a gyrus near the skull, or in the inferior wall of a sulcus in the interhemispheric fissure (pink areas in Figure 5.5), one should place the anode (/cathode) over the target to achieve excitation (/inhibition). The second electrode should be placed at a moderate distance; its exact placement is not very important. For targets in the superior wall of a sulcus in the interhemispheric fissure (brown areas in Figure 5.5), one should place the cathode (/anode) over the target for excitation (/inhibition). For targets in a sulcus near the skull or on a gyrus in the interhemispheric fissure (blue areas in Figure 5.5), the electrodes should be placed close to the target on opposite sides with the interelectrode line perpendicular to the fissure. To achieve excitation (/inhibition), the cathode (/anode) should be placed on the side of the fissure where the target is located and the anode on the opposite side.

### Combined results

By combining the optimization results of several target areas distributed over the gray matter, it was possible to find general patterns and understand how they arise. Optimization was performed for five areas on gyri, two areas in sulci and one in the interhemispheric fissure. The obvious consistency in the results among similar areas, and the distinct contrasts with differently located areas, showed that it is not the absolute location of a target area that determines the optimal current flow. The relative location with respect to the skull and to the interhemispheric fissure, and the local GM curvature determine in a comprehensible way which bipolar configurations are optimal for stimulating a certain brain area. Although the curvature of the brain is spatially inconsistent within an individual, and highly different amongst individuals, each brain consists of gyri, sulci and fissures, and therefore the optimal field for each cortical target area on an individual MRI can be easily understood. The overview presented in Figure 5.5 reduces the infinite number of target areas to a discrete set with distinct criteria that can be applied to any brain. To find the optimal configuration for a specific individual, one would need to determine the location of the area of interest on a personal MR image using either anatomical landmarks or functional imaging. This image and localization can then be related

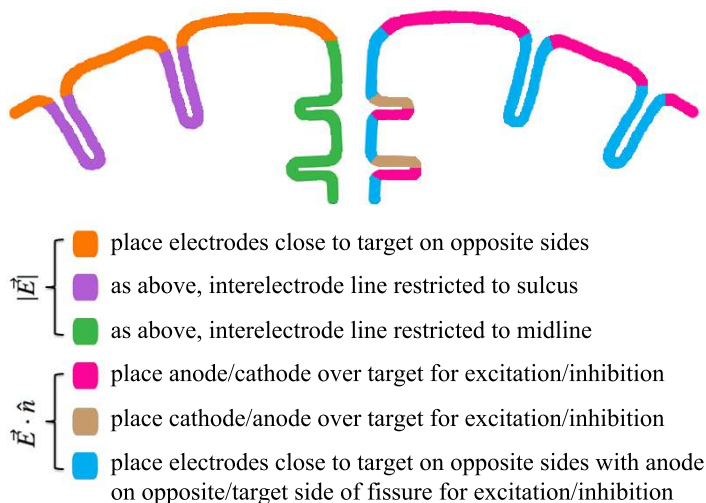


**Figure 5.5** Electrode placement recommendations for achieving maximal field strength (left) or maximal field strength in the preferred direction (right) in the targeted brain area, for both excitative and inhibitive tDCS. A schematic representation of the top part of a coronal slice is used to visualize how the location of the target area determines the optimal electrode placement.

to Figure 5.5 to select a suitable configuration. It should be noted that these results are only valid for targets in the gray matter of healthy subjects. For targets in deep brain structures, optimal configurations can be found using the dataset produced for this study. For patients with brain or skull defects, other models should be used.

Optimizations based on field strength and direction resulted in completely different optimal configurations and often contradictory advice. Unfortunately, the mechanisms behind the effects of tDCS are not understood well enough to know which factor is more relevant. From experimental studies showing opposite effects by reversing stimulation polarity<sup>[108]</sup> it is known that the direction of the field plays a role in the effects of tDCS. Also, the conventional configurations that have been shown effective in many studies (Table 5.1) resemble the direction-based and not the strength-based optimization results. It thus seems that direction is a determining factor. Comparing the effects of the here-presented strength- and direction-based optimal configurations in an experimental paradigm might show which setup is the most effective and thus which factor is more important. This information is valuable for optimization and future modeling efforts, but also for understanding the effects of tDCS.

## Relation to other studies

Previous optimization efforts have been reported. In a methodological study<sup>[67]</sup>, an optimization approach was described using a three-compartment model with two point electrodes. The same model was later used to optimize current injection through 24 circular electrodes (4 cm radius) in an anterior-posterior setup<sup>[116]</sup>. Optimized multichannel stimulation patterns were also calculated for 64 cylindrical electrodes (1.2 cm radius) using a 5-compartment model<sup>[36]</sup> and for 19 rectangular electrodes ( $\sim 22 \text{ cm}^2$ ) using a 10-compartment model with WM anisotropy<sup>[141]</sup>. Because different conductivities were used in these studies and the dimensions and locations of target areas were not always clearly described, it is not straightforward to compare the results of these studies to the results in this chapter.

Dmochowski et al.<sup>[36]</sup> optimized field strength either radial or tangential to the skull for 'a cortical target' and found that, with 64 available electrodes, the optimal configuration in both cases was a bipolar configuration. A maximal radial field strength of 3.1 mV/cm (with 2 mA input current) was reached, equal to an improvement of 37% compared to an approximated conventional configuration (5 circular electrodes), which is comparable to the results presented here. Also the electrode placement in their optimal configuration of small circular electrodes is similar to what was found here. Sadleir et al.<sup>[141]</sup> optimized absolute current density in the left IFG. The optimal configuration of 19 electrodes lead to a 56% decrease compared to the conventional configuration. Taking only the two electrodes with the highest weights (F3-P3) resulted in an improvement of 14%. As the approach used in this chapter resulted in a 110% improvement in the left IFG, it is possible that their iterative approach may have ended up in a local minimum.

The above-described results<sup>[36,141]</sup> showed, for both large and small electrodes, that with multiple electrodes available, maximal field strengths were reached by using only two. From this it can be concluded that for maximal electric field strength in the target area, also in a specific direction, one should use a bipolar configuration. Selecting an appropriate configuration can then be done using the results in this chapter. If there are additional constraints, like maximizing focality<sup>[36]</sup> or selectively avoiding other brain areas<sup>[141]</sup>, multi-electrode setups might be favorable.

For this study, over 3000 configurations were simulated. One might suggest that optimization could have been performed more efficiently by simulating each electrode site once with a common reference electrode and taking linear combinations to produce other configurations. However, such an approach can only be performed for point electrodes or by assuming a constant current density over the surfaces of the electrodes. As tDCS with large electrodes leads to large areas of constant potential, each configuration was modeled explicitly in order to get exact results.

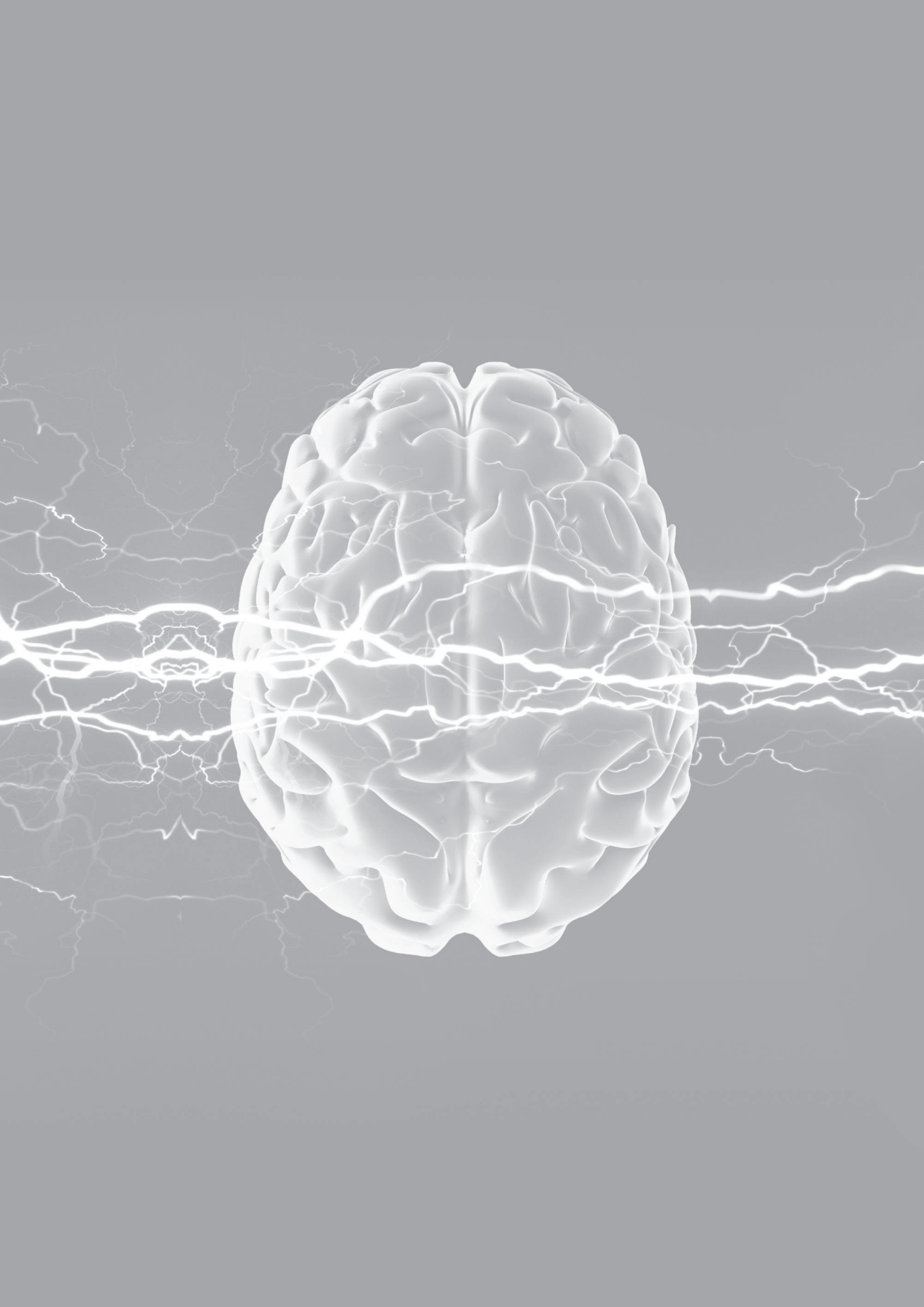
## 5.5 Conclusions

---

The location of a target brain area relative to the skull and with respect to the interhemispheric fissure, and the local GM curvature, determine in a comprehensible way which bipolar configurations are optimal for stimulating a certain area. Maximal electric field strength in the target area can be achieved by placing the electrodes on opposite sides close to the target. In order to maximize field strength perpendicular to the GM surface, the conventional method of electrode placement (anode over the target area to achieve excitation and cathode further away) should be used for superficial targets on gyri. Additional guidelines apply for more uncommon targets.

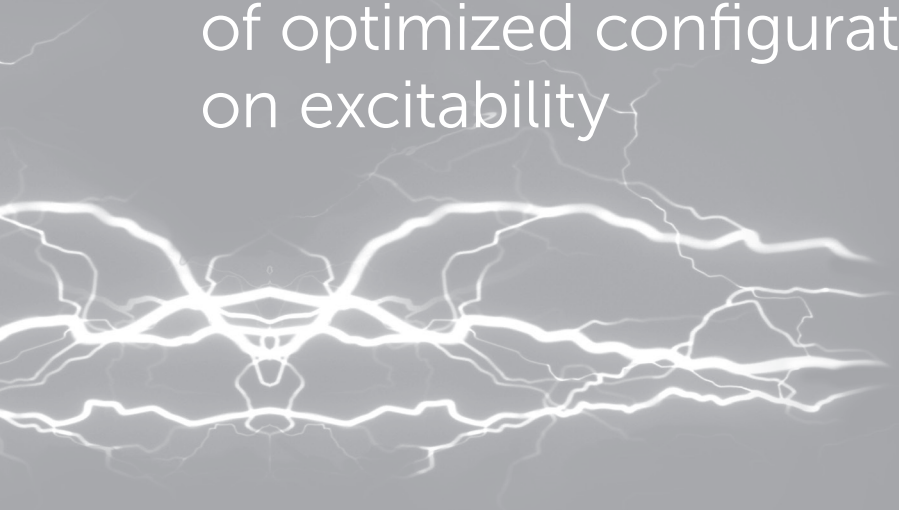






## Chapter 6

# Measuring the effects of optimized configurations on excitability



Based on: *Evaluating the effects of model-based optimal bipolar tDCS configurations on cortical excitability*, by Sumientra Rampersad, Vincent Jansen, Edwin van Asseldonk and Dick Stegeman, submitted for publication.



## 6.1 Introduction

Volume conduction modeling has emerged as a promising tool to better understand and possibly improve the effects of tDCS. Simulations with a highly detailed model have shown consistently for five of the most-used conventional configurations that the areas of highest field strength are located midway between the electrodes, instead of at the intended target site (Chapter 4). These results suggest that increased effects of tDCS could be achieved by better targeting the electric current with adapted configurations.

Some investigators have suggested novel configurations that produced more appropriate simulated electric fields than the conventional configurations do<sup>[33,116,36,141]</sup>. However, experimental validations are scarce. Only Datta et al.<sup>[33]</sup> experimentally tested their setup, which consisted of five small circular electrodes around the target area. Compared to the conventional configuration for motor cortex stimulation, their setup resulted in stronger and longer-lasting effects on corticospinal excitability<sup>[76]</sup>. This first experimental validation of a model-based configuration seems promising. Nonetheless, this and other suggested novel configurations use multiple, often small circular electrodes and multi-channel stimulation patterns. As such setups are not available in most labs, it would be more valuable in practice if increased effects could be reached with optimized placement of a common bipolar setup.

Chapter 5 presented an extensive modeling study performed to optimize tDCS configurations of two large square electrodes. For each of six target sites, optimizations were performed by maximizing either the *electric field strength* ( $|\vec{E}|$ ) or the *field strength in the most effective direction* in the cortical target area. The most effective direction of the field was assumed to be along the axons of pyramidal cells<sup>[138,127]</sup>, so perpendicular to the cortical surface<sup>[62]</sup>. This was quantified as  $\vec{E} \cdot \hat{n}$  with  $\vec{E}$  the electric field vector and  $\hat{n}$  the normal vector to the cortical surface. The configurations with the highest values for  $|\vec{E}|$  or  $\vec{E} \cdot \hat{n}$  in the target area were selected as the optimal configurations for *strength-based* and *direction-based optimization*, respectively. For most target sites, optimal configurations were found with field strengths in the target area twice as high as for the conventional configurations (Table 5.2). The improvements in  $\vec{E} \cdot \hat{n}$  were smaller.

The aim of the current study was to experimentally compare the strength- and direction-based optimal configurations from the above-described study with the conventional configuration for tDCS of the M1 hand area. The three configurations were assessed on their effects on neural excitability using single-pulse TMS and EMG.

## 6.2 Methods

---

This study was performed as a crossover design with each subject receiving three sessions of tDCS with different configurations in randomized order. The sessions were separated by at least one week and performed consistently at the same time of day. The effects of tDCS on corticospinal excitability were evaluated via measurements of motor-evoked potentials using single-pulse TMS.

### Subjects

Twenty healthy right-handed adults (7 male, age  $23.6 \pm 3.8$  years) participated in the experiment. The volunteers were free of medication and had no history of neurological illness. They were not allowed any stimulants before the measurements. None had ever received tDCS or TMS. All participants gave written informed consent. The study was approved by the medical ethical research committee of the Radboud University Medical Centre and conformed to the Declaration of Helsinki.

### Experimental procedure

Subjects were seated on a comfortable chair with their hands reposed on a pillow. Surface EMG of the right FDI muscle was continuously monitored by the investigator; if activity was detected in the signal, subjects were instructed to relax their hand. Using single-pulse TMS with neuronavigation, the cortical representation of the right FDI muscle was identified as the location that resulted in the highest MEPs (*hotspot*). Next, a stimulator intensity was established that resulted in consistent MEPs at this location. The location and intensity were re-evaluated preceding each subsequent session. Before the start of the experiment, subjects were instructed to move or speak as little as possible without getting uncomfortable and to keep their eyes open. Each experiment consisted of a 5 minute baseline excitability measurement (pulse interval:  $10 \pm 2$  s, 30 pulses total), 15 minutes tDCS, and a 25 minute post-stimulation excitability measurement (pulse interval:  $10 \pm 2$  s, 150 pulses total).

### Application of tDCS

In the theoretical model (Chapter 5), the electrodes were perfect  $5 \times 5$  cm<sup>2</sup> square patches of homogeneous conductivity. This setup was reproduced here as closely as possible. At both electrode locations, a  $5 \times 5$  cm<sup>2</sup> area of skin was cleaned with

**Table 6.1** Characteristics of the three configurations used in this study to stimulate the left motor cortex. The two configurations that were compared to the conventional configuration were based on a modeling study that produced configurations optimized for either field strength ( $|\vec{E}|$ ) or field strength perpendicular to the GM surface ( $\vec{E} \cdot \hat{n}$ ) in a small GM volume centered on the FDI target site (Chapter 5).

	$C_C$	$C_S$	$C_D$
configuration	conventional	optimal $ \vec{E} $	optimal $\vec{E} \cdot \hat{n}$
anode location	left M1 FDI <sup>(a)</sup>	CP3 <sup>(b)</sup>	left M1 FDI
cathode location	Fp2 <sup>(b)</sup>	Fz <sup>(b)</sup>	O2 <sup>(b)</sup>
$ \vec{E} ^{(c)}$ (mV/cm)	1.4	2.9	1.5
$\vec{E} \cdot \hat{n}^{(c)}$ (mV/cm)	1.2	-0.6	1.4

<sup>(a)</sup>TMS hotspot of the right FDI muscle.

<sup>(b)</sup>As determined in the 10-10 system for electrode placement.

<sup>(c)</sup>Mean value in the cortical target volume of the theoretical model.

alcohol and abrasive gel. Conductive paste<sup>a</sup> was applied homogeneously to the skin and to a pair of 5 x 5 cm<sup>2</sup> carbon rubber surface electrodes, before pressing them onto the skin. The paste fixates the electrodes to the head without movement. This method maximizes homogeneous current density over the entire surface of the electrodes. A current of 2 mA was delivered by a constant current stimulator<sup>b</sup> for 15 minutes with fade in and out periods of 10 seconds.

## Electrode configurations

The conventional configuration for motor cortex tDCS was compared with two theoretically optimal configurations (Chapter 5). The characteristics of the three configurations tested in this study are summarized in Tables 6.1 and Figure 6.1.

The conventional configuration ( $C_C$ ) for facilitative stimulation of the motor cortex consists of an anode over M1 and a cathode over the contralateral supraorbital area<sup>[108]</sup>. As in Chapter 5, the M1 location used in this study was the cortical representation of the right FDI, located in the left M1 as the TMS hotspot (black spheres in Fig. 6.1). In the experimental sessions, each subject's individual hotspot was used to position the anode. The cathode was placed at the Fp2 location of the standardized 10-10 system (Fig. 6.1a). Simulations of  $C_C$  result in highly suboptimal field strengths (Fig. 6.1b), while the distribution of  $\vec{E} \cdot \hat{n}$  on the GM surface seems ap-

<sup>a</sup>Ten20, Weaver and Company, Aurora, Colorado, USA.

<sup>b</sup>eldith DC-stimulator, neuroConn GmbH, Illmenau, Germany.

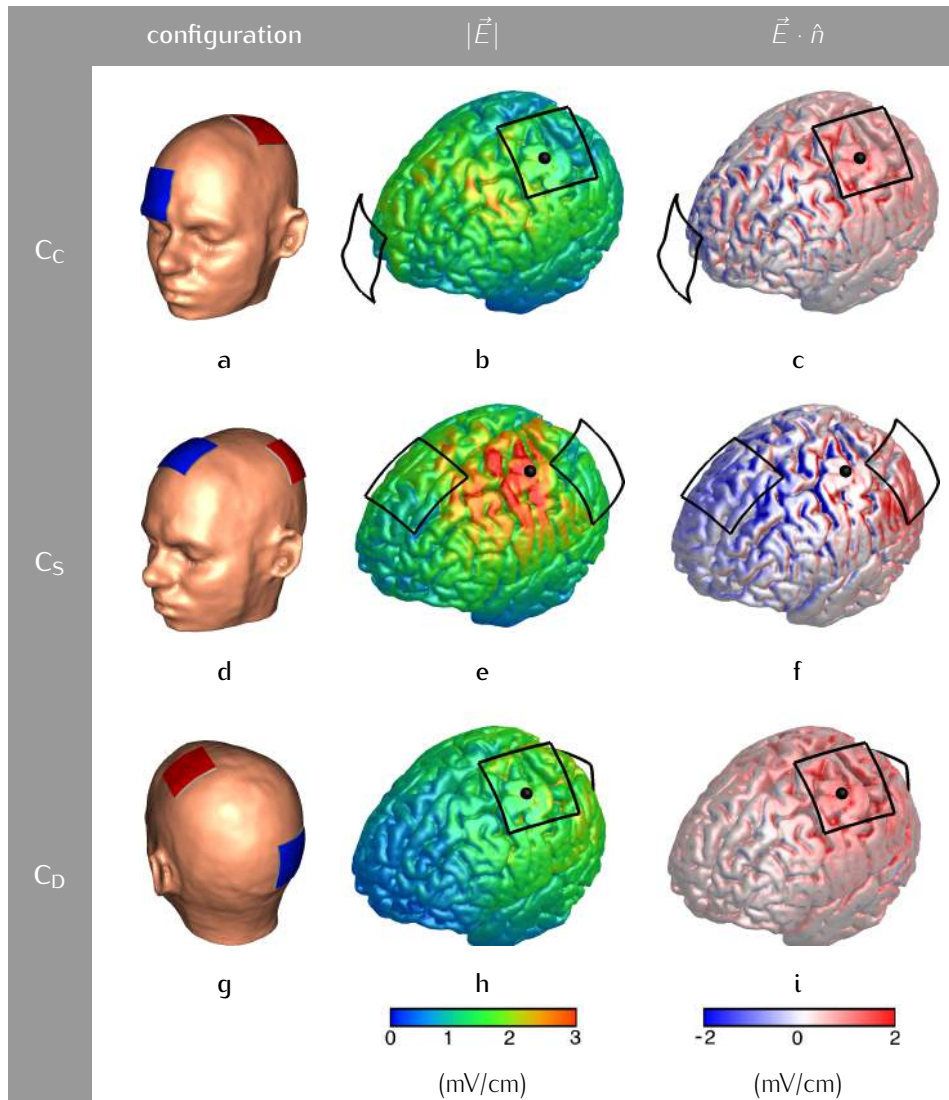


**Figure 6.1** The three configurations investigated in this study and their simulated electric field distributions on the GM surface. In the first column, the location of the electrodes on the head is illustrated (red for anode, blue for cathode). a) M1 – Fp2, d) CP3 – Fz, g) M1 – O2. The figures in the second column display electric field strength ( $|\vec{E}|$ ). The electrode outlines on the skin are drawn in black and the target location (FDI hotspot) is marked by a black sphere. The figures in the third column display the field strength perpendicular to the GM surface ( $\vec{E} \cdot \hat{n}$ ). Red indicates that the electric field is directed in the preferred direction for excitative stimulation, i.e. perpendicularly into the GM surface, blue indicates the opposite direction and white means that the field is perpendicular to optimal.

proprate (Fig. 6.1c; for facilitative stimulation, dark red values are expected to be optimal).

The strength-based optimal configuration ( $C_S$ ) consists of an anode over CP3 and a cathode over Fz (Fig. 6.1d). The resulting electric field is maximal around the target area (Fig. 6.1e) and the theoretical improvement in target field strength compared to  $C_C$  is 105% (Table 6.1). The direction of the field, however, is almost perpendicular to what is expected to be optimal (Fig. 6.1f, Table 6.1).

For the direction-based optimal configuration ( $C_D$ ) the anode was placed over the FDI hotspot and the cathode over O2 (Fig. 6.1g). This was not the configuration resulting in maximal target  $\vec{E} \cdot \hat{n}$ , but it was near-maximal<sup>c</sup> and could be measured on subjects' heads more consistently. The maximum of the resulting  $\vec{E} \cdot \hat{n}$  distribution is centered around the target area (Fig. 6.1i). Because  $C_C$  performed relatively well regarding  $\vec{E} \cdot \hat{n}$ , the improvement in the target area is only 17% (Table 6.1). Regarding absolute field strength,  $C_D$  is highly suboptimal (Fig. 6.1h, Table 6.1).

In summary:  $C_S \gg C_C \approx C_D$  for  $|\vec{E}|$ . For field strength in the most effective direction the situation is almost reversed:  $C_D > C_C \gg C_S$  for  $\vec{E} \cdot \hat{n}$ .

## Measurements of corticospinal excitability

Single-pulse TMS was used to find the FDI hotspot and to evaluate neuronal excitability at this location (Section 1.1.1). TMS pulses were induced with a figure-of-8 coil by a MagPro X100 stimulator<sup>d</sup>. The coil was held tangentially to the skull, with the handle pointing 45° clockwise from the midline<sup>[96]</sup>. The location of the FDI representation on the skin was recorded using stereotaxy<sup>e</sup>. During the experiment, the error between the recorded location and the current coil position was used for on-line visual feedback and registered for analysis purposes. MEPs were acquired from the right FDI muscle using EMG. After cleaning the skin with alcohol, two surface electrodes were placed in a belly-tendon montage. The EMG signals were amplified (250x) and filtered (band-pass: 10–500 Hz) via an EMG amplifier<sup>f</sup>.

## Analysis

As muscle activation can facilitate motor responses<sup>[63]</sup>, MEPs preceded by a root-mean-square EMG signal greater than 20  $\mu$ V in the 200 ms before the response were excluded from analysis. TMS pulses with a neuronavigation error greater than 2 mm were excluded as well. This amounted to less than 1% of all MEPs. Finally, the first

<sup>c</sup> $E_n > 95\%E_n^{\text{mx}}$  (Fig. 5.4a).

<sup>d</sup>MagVenture, Tonika Elektronik, Farum, Denmark.

<sup>e</sup>BrainSight, Rogue Research, Montreal, Canada.

<sup>f</sup>Ekida GmbH, Denzlingen, Germany.



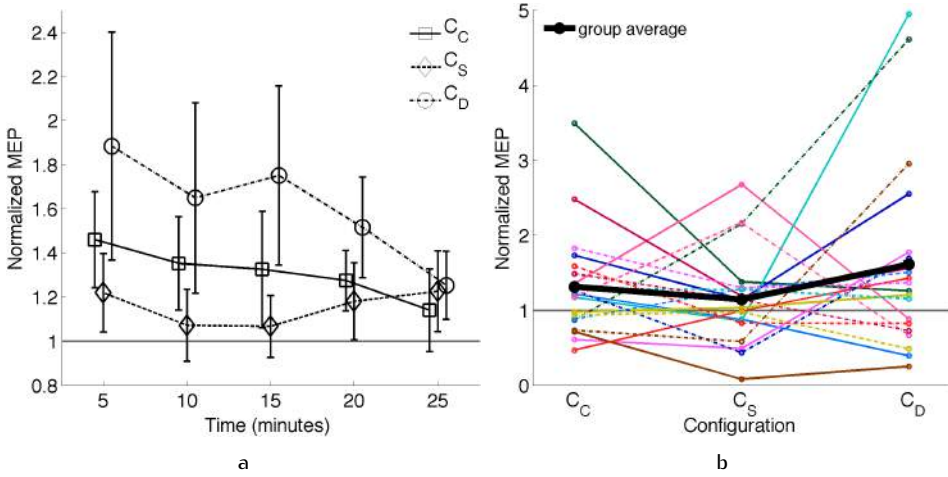


**Figure 6.2** Normalized MEP responses to three tDCS configurations for hand motor cortex stimulation. The horizontal gray line indicates the baseline value. (a) Group-averaged results, showing the progression of the effect in time bins of five minutes. Error bars represent one standard error of the mean. (b) Time-averaged results, showing the average effect per configuration for each subject separately (colored lines) and the group-averaged total effects (black line).

fifteen MEPs of each baseline measurement and each post-stimulation measurement were excluded, because an initial transient state of physiological origin can influence measures of excitability<sup>[143]</sup>. The peak-to-peak amplitude of the remaining MEPs was calculated.

The post-stimulation-measured MEPs were subdivided into 5 successive bins of 5 minutes. As the MEPs in each bin were not normally distributed (Kolmogorov-Smirnov test with  $p < 0.001$ ), medians were used to report and analyze the data. For each session, the median of the baseline MEPs,  $M_0$ , was used to normalize the bin medians of that session:  $M_i^* = M_i/M_0$  for  $i=1:5$ . The  $M_i^*$  values were analyzed as a dependent variable in a linear mixed model with fixed effects *Configuration* ( $C_C$ ,  $C_S$ ,  $C_D$ ) and *Time* ( $t_1$ – $t_5$ ). To account for the correlation between the repeated measurements within a subject, different intercepts were allowed for each subject by including the factor subject as a random factor. Because of the spread in baseline values between sessions, the  $M_0$  values were incorporated into the analysis as a covariate.

## 6.3 Results

Most subjects reported a slight burning sensation under the anode (23% of sessions), cathode (25%) or both (40%); itching and stinging were also reported. These sensations were similar for all three configurations and are not different from what is commonly reported. Stimulation impedances for the new configurations were also similar to that for the conventional setup ( $C_C$ :  $2.5 \pm 0.5$  k $\Omega$ ,  $C_S$ :  $2.7 \pm 0.5$  k $\Omega$ ,  $C_D$ :  $2.5 \pm 0.7$  k $\Omega$ ).

The group-averaged  $M_i^*$  values (Fig. 6.2a) show an increase in MEP responses after stimulation for all three configurations, with  $C_D > C_C > C_S$ , and the effects of  $C_D$  and  $C_C$  decrease over time. The linear mixed model did not reveal a significant effect for Time ( $F(4, 262) = 0.65, p = 0.63$ ) or for the interaction effect Configuration  $\times$  Time ( $F(8, 262) = 0.31, p = 0.96$ ). The covariate  $M_0$  was significantly related to the MEP responses  $M_i^*$  ( $F(1, 228) = 8.55, p < 0.01$ ). Despite this partial explanation of the variance, the effect of Configuration was significant ( $F(2, 263) = 3.28, p = 0.04$ ). Pairwise comparisons revealed a significant difference between  $C_S$  and  $C_D$  ( $p = 0.04$ ), but not for the other combinations.

As there was no significant effect of Time, the  $M_i^*$  for each subject were averaged over time to provide a quantification of the individual total effects for each configuration  $\bar{M}^*$  (Fig. 6.2b). In the individual results, all possible outcomes occur (e.g.  $C_D > C_S > C_C$  and  $C_C > C_S > C_D$ , etc.). None of the three configurations performs consistently better than one of the others. Also, for all three configurations, some subjects show a decreased instead of the expected increased response. The group-averaged total effects (black line in Fig. 6.2b) reveal an overall increase of 31%, 14% and 61% for  $C_C$ ,  $C_S$  and  $C_D$ , respectively.

## 6.4 Discussion

Two theoretically optimized configurations for field strength or field strength perpendicular to the GM were experimentally compared to the conventional configuration for motor cortex stimulation. Changes in corticospinal excitability were evaluated in twenty healthy subjects. While the group-level results fit the hypothesis that one of the optimized configurations would perform better than the conventional configuration, individual results differed strongly.

## Group-level results

The direction-optimized configuration resulted in significantly larger group-level effects than the strength-optimized configuration. As the calculated field strength in the targeted area with  $C_S$  is twice as high as it is with  $C_D$ , these results suggest that absolute field strength is a subordinate factor in the effects of tDCS. Field strength perpendicular to the GM does seem to be a relevant factor. As the difference between the results of  $C_C$  and  $C_D$  was not significant and the variability in the results was large, it cannot be concluded that  $C_D$  is more effective than  $C_C$ , but large effects do appear to be more probable using  $C_D$ . Furthermore, these results show that increased excitability can be achieved with bipolar configurations other than the conventional one. This leaves room for a choice of configuration convenient for the specific experimental setting. With the anode placed over the motor cortex, the cathode can have many locations that lead to (near-)optimal electric fields in simulations (Fig. 5.4).

Only one study compared different bipolar tDCS electrode placements for their effects on excitability. In the first study to evaluate the effects of tDCS using TMS measurements of excitability, Nitsche & Paulus<sup>[108]</sup> tested six different configurations to stimulate the hand motor cortex (Fig. 1.4). Of these configurations, the ‘motor cortex – forehead’, ‘area anterior to motor cortex – occipital cortex’ and ‘motor cortex – occipital cortex’ setups are similar to  $C_C$ ,  $C_S$  and  $C_D$ , respectively. Although the occipital electrode was over the left hemisphere in these setups and over the right hemisphere in  $C_D$ , according to the findings in the previous chapter these configurations should be effectively equivalent (Fig. 5.4). Nitsche & Paulus<sup>[108]</sup> found only the ‘motor cortex – forehead’ configuration to be effective, while in the present study an overall effect was reported for all three. This discrepancy in results can possibly be explained by the difference in stimulation duration – 4 seconds versus 15 minutes – and the fact that they measured MEPs just before the end of stimulation, while in this study aftereffects were measured. The finding that at least 3 minutes of stimulation were needed to induce aftereffects<sup>[108]</sup> supports this explanation. Also, different mechanisms have been suggested for the direct and aftereffects of tDCS<sup>[147]</sup>.

The ‘motor cortex – forehead’ setup soon became the conventional motor cortex configuration used by many researchers; the configurations that produced no results were no longer considered. The current findings suggest that configurations that are ineffective during short stimulation (4 s) can produce aftereffects with long stimulation (15 minutes). Therefore effective configurations for different stimulation parameters might not be interchangeable. As the electric fields do not depend on stimulation parameters other than configuration, different mechanisms must be at work, which is in agreement with<sup>[147]</sup>.

## Variability

Excitability changes for the conventional configuration were similar in size to what has been reported in other studies<sup>[108,105,76]</sup>. However, standard errors reported here were 2–4 times larger, even though the number of subjects was higher (20 versus 10–14). The data showed considerable variation in baseline values. Although this could explain part of the variability in the results (covariate  $M_0$  was significantly related to  $M_i^*$ ), substantial unexplained variability remained.

A cause for this large variability could not be found in the experimental setup, as many precautions were taken to minimize variability. Because motor activity during<sup>[99]</sup> and after tDCS<sup>[72]</sup> can decrease its results, subjects were not allowed to move during the complete experiment, hand activity was strictly monitored and MEPs with pre-activation were excluded. As cognitive tasks can also affect the results of tDCS<sup>[6]</sup>, sensory influences were minimized by placing the subject in a silent room in front of a grey screen. Subjects were not allowed any stimulants preceding the experiment and all three sessions were performed around the same time of day. All subjects were right-handed. Consistent TMS stimulation was ensured by using neuronavigation and only including pulses with minimal location errors. By using conductive paste, common tDCS problems<sup>[65]</sup> were avoided. No other study has reported applying such stringent measures, yet variability in the present study was higher.

One possible cause of variation could be subject's thoughts<sup>[6,126]</sup>. Also, after the experiment subjects often reported boredom and difficulty to stay focused. A complete absence of visual and auditory stimuli in the lab might therefore not be optimal. Instead, it might be beneficial to develop an environment or task for tDCS studies that gives a better balance in the amount of sensory input in order to maintain a more constant state of mind.

Horvath et al.<sup>[65]</sup> recently reviewed all studies that measured excitability changes induced by motor cortex tDCS. The review describes large variability *between* studies that report small variability. As possible causes for inconsistent results, they mention several shortcomings in the experimental setup, most of which have been corrected for here, as described above. What remains are differences within the subjects themselves. These include subject-specific differences in neurophysiology, anatomy and psychology, but also session-specific influences like circadian, metabolic and hormonal cycles.

## Individual results

In light of the large variance in the results of this study, individual effects were investigated. The time-averaged responses for  $C_C$  (Fig. 6.2b) show overall facilitation ( $\bar{M}^* > 1.1$ ) for 12 subjects, inhibition ( $\bar{M}^* < 0.9$ ) for 6 subjects and no excitability change ( $0.9 \leq \bar{M}^* \leq 1.1$ ) for 4 subjects. Individual  $M^*$  time courses for  $C_C$  (not shown) were also highly variable between subjects. Most time courses showed several fluctuations; the average response to  $C_C$  reported in most studies – including the current one – of an immediate increase after tDCS followed by a continuous decrease back to baseline, was only seen in one individual case. These findings explain the absence of a time effect and the high SEs in the group-averaged results.

For the two new configurations, individual time courses were also highly varying and the ratios of facilitated to inhibited subjects were similar to the conventional case (10:7 for  $C_S$  and 13:7 for  $C_D$ ). As  $C_D$  results in the largest excitability changes and these changes are bidirectional, this leads to the largest SEs for this configuration (Fig. 6.2a).

Two recent studies evaluated excitability after tDCS with the conventional motor cortex configuration in 53<sup>[162]</sup> and 56<sup>[85]</sup> healthy volunteers, by far the largest study populations yet. Wiethoff et al.<sup>[162]</sup> reported no effect of time on the group-averaged results for 30 minutes post-stimulation and individual time courses were highly variable. López-Alonso et al.<sup>[85]</sup> found no significant effect on MEP amplitude over a time period of 60 minutes. Both studies included a two-step cluster analysis to discover possible subpopulations with similar response patterns. Both analyses resulted in two clusters of ‘responders’ and ‘nonresponders’ in which the responders, 47%<sup>[162]</sup> and 45%<sup>[85]</sup> of subjects, did show a significant effect for most time points. The nonresponders of Wiethoff et al.<sup>[162]</sup> showed a slight non-significant increase, while the non-responders of López-Alonso et al.<sup>[85]</sup> showed a slight decrease that was significant at some time points. Time-averaged results showed facilitation ( $\bar{M}^* > 1$ ) in 74%<sup>[162]</sup> and 50%<sup>[85]</sup> of subjects. In the current study,  $C_C$  resulted in  $\bar{M}^* > 1$  for 60% of subjects.

These results break with the view that anodal tDCS is exclusively facilitative stimulation. Instead, anodal tDCS can induce either facilitation, inhibition or no effect in individuals. The above studies suggest that the natural incidence of these predispositions in a representative subject population will result in an average with a high variance. As the results in this chapter agree well with these extensive investigations, it seems that the tested subject group was a good representation of the population. Studies reporting small SEs suggest a large proportion of responders in the subject group. It is therefore recommended to use larger subject groups for tDCS studies in order to avoid undersampling. With a sufficiently large sample size,

a cluster analysis can be performed to group (non)responders. Characteristics of both groups can be studied to gain insight into the mechanisms behind tDCS.

### Field strength and direction

The commonly reported polarity-specific results of tDCS suggest that the direction of the current determines the direction of the effect. The largest effects for anodal tDCS would then assumably be reached by currents directed inward along the pyramidal neurons, a notion that inspired the optimization study (Chapter 5) on which the present investigation was based. The group-averaged results presented here agree with this hypothesis, but the individual results do not.

If indeed the direction of the current were to dominate the (individual) tDCS-induced effects, it would be impossible to have some subjects increase and some decrease their excitability with the same configuration, as their respective neurons would have to be in opposite directions. Bidirectional results were nevertheless found for all three configurations tested here, and also in previous studies for both anodal and cathodal stimulation with  $C_C$  [162,85].

Also when comparing the responses to the three configurations within one individual, the results do sometimes not agree with the above assumption. Some subjects show highly diverging and even opposite results to  $C_C$  and  $C_D$  (Fig. 6.2b), while the predicted direction of the field in the target area only differs by 17% (Table 6.1). Other subjects show similar results for  $C_S$  and  $C_D$  (Fig. 6.2b), while the electric fields are close to perpendicular (Table 6.1, Fig. 6.1f,i).

It follows from the above that neither the strength nor the direction of the electric field can explain the effects of tDCS on an individual level. Judging from the group-averaged results, the field strength directed into the brain is of influence, but other factors dominate individual results. Instead of a fixed predisposition to (not) respond to tDCS, the state of the brain at the time of stimulation might determine the size and direction of the effects. The Bienenstock-Cooper-Munro (BCM) model of homeostatic plasticity<sup>[14]</sup> could govern such a state-dependent process. Following this theory, excitability of the brain is kept within a natural range: stimulation will lead to a decrease in excitability if the pre-stimulation level was high and to an increase if the pre-stimulation level was low. If excitability were indeed a homeostatic process, anodal tDCS could result in either facilitation, inhibition or no effect. This is fitting to the results in this chapter. Fricke et al.<sup>[51]</sup> tested the BCM theory in relation to tDCS, by applying two consecutive periods of anodal tDCS with 3 minutes in between. Like they hypothesized, the first period induced facilitation on a group level and the second period of identical stimulation induced inhibition.

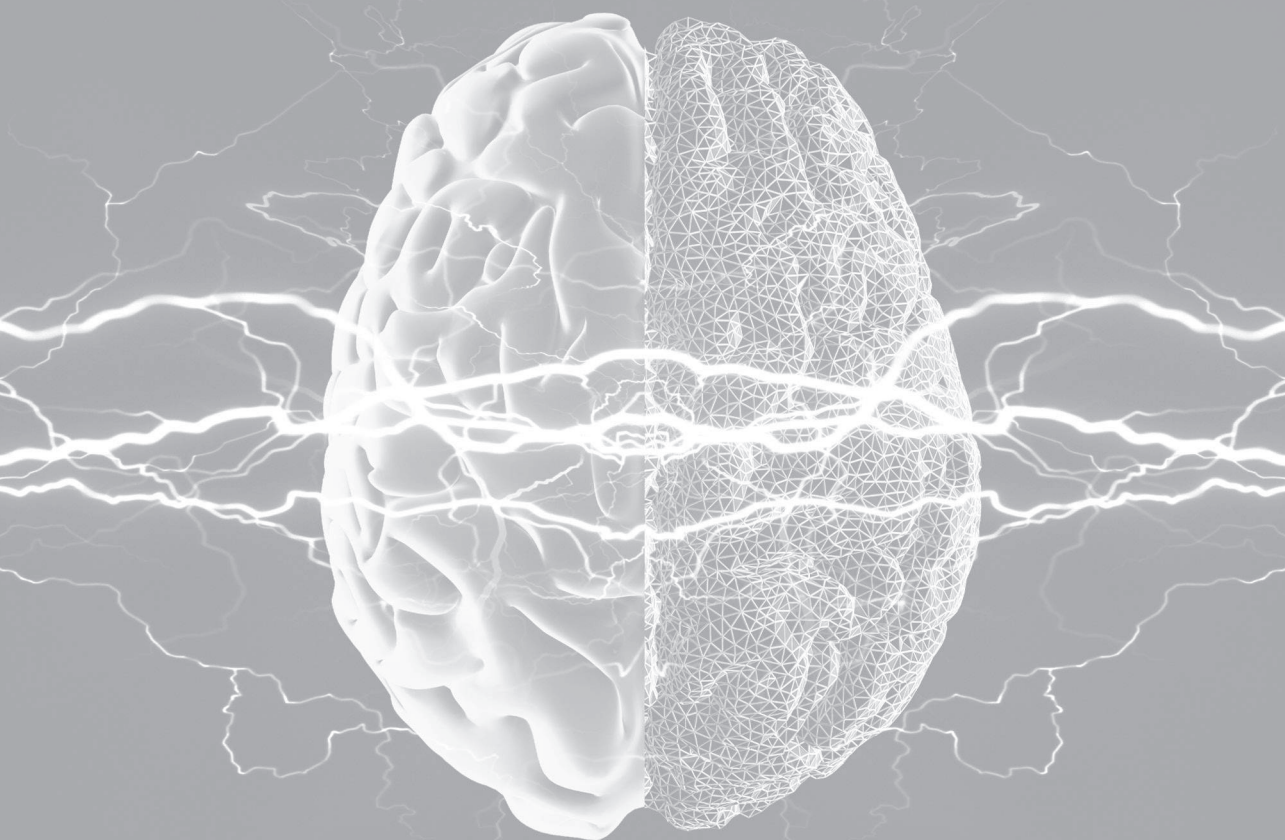
## 6.5 Conclusions

---

Comparing the experimental results in this chapter to the model-based predictions suggests that optimally directed field strength has more influence on the effects of tDCS than absolute field strength. Furthermore, the direction-optimized configuration for motor studies (M1 – O2) appears to be more probable to result in large excitability changes than the conventional configuration. The direction of the field should therefore be taken into account in future studies. Despite indications that optimal field direction is important, subject- and session-specific influences dominate the effects of tDCS on an individual level. Therefore, large subject groups are recommended in experimental studies to allow clustering of subjects. This study investigated motor corticospinal excitability; suggested optimized configurations for other targets<sup>[131]</sup> (Chapter 5) should also be investigated, as results might be different for various behavioral tasks.







Chapter 7

Conclusion





## 7.1 Summary

---

In this thesis, titled *Simulation of stimulation: On modeling and measuring the effects of transcranial direct current stimulation on the human brain*, four computational studies and one experimental study are presented that together aimed to explore and improve the effects of tDCS. A detailed abstract of each study can be found at the start of each chapter. Below the complete thesis will be summarized succinctly, followed by a discussion of the results in the next section.

### Stimulation and simulation

Electric brain stimulation has been used for centuries in attempts to treat depression and headaches, but it was only after the effects were demonstrated objectively through measurements of corticospinal excitability, that tDCS became a popular neuroscientific technique. By applying weak currents to two large electrodes attached to the head, certain neuronal properties can be influenced during and after stimulation. When applied to the primary motorische cortex (M1), the resulting changes in neuronal excitability can be quantified using TMS and EMG. Applying tDCS to other cortical areas can affect motor or cognitive functioning or result in symptomatic improvement in patients suffering from neuropathological conditions. Although tDCS is a promising technique, its effects are often small or short-lived and its working mechanisms are largely unknown. Computer simulations of the tDCS-induced electric field in the brain can provide valuable knowledge to help understand and improve the technique. As computational and imaging capabilities have grown over recent years, so have the possibilities in volume conduction modeling. Highly detailed and realistic models can be made, increasing the accuracy but also the costs of simulations. These models can be used to investigate electric field strengths in the brain and also field direction with respect to the neuronal fibers.

### Modeling: Improving accuracy and efficiency of tDCS modeling

The first part of this thesis describes studies that investigated the effects of various tissue types in tDCS volume conduction models on the simulation results in order to improve the efficiency and accuracy of such models.

In Chapter 2 a spherical three-compartment model was used to investigate the influence of different skull modeling approaches. The layered structure of the skull was explicitly modeled and compared with three common approximation methods for a range of conductivities. Approximating the skull as a single isotropic layer with

an equivalent bulk conductivity resulted in large errors compared to the reference model, while both anisotropic and isotropic single-layer approximations with appropriate conductivity values could approximate the properties of real skull well. The radial component of the conductivity tensor was shown to be highly influential to the results.

Chapter 3 describes the creation of a realistic hexahedral head model. By including different tissue types and conductivity properties, six different models were created from the basis model. The effects of including each additional feature were investigated step by step. Accurate skull modeling proved to be important if the electrodes are placed over areas containing a substantial amount of spongiosa, while an accurate representation of the CSF, and therewith the brain surface, is always important. Modeling gray and white matter as separate compartments significantly changes the resulting fields, while WM anisotropy is only essential in deeper target areas.

## Modeling: Investigating and improving tDCS-induced electric fields

The thesis continues with a description of the creation process of the currently most detailed volume conduction model for tDCS. This model was used to simulate the conventional configurations for five target areas. As it was observed that the stimulation strength at the target area was not optimal for these conventional configurations, the model was subsequently used to optimize electrode placement.

When using large electrodes, currents mainly cross the skin at the perimeters of both electrodes, while on the brain surface the current density maxima have converged into one central area. For stimulation of the motorische cortex, DLPFC, IFG and occipital cortex, the conventional configurations produced electric field strength distributions with a maximum roughly midway between the electrodes. The standard cerebellum configuration results in a maximum at the targeted location but with half the intensity as for the cerebral targets. The electric field in the presumably most effective direction, i.e. perpendicular to the GM surface, was analyzed as well and seemed a factor to take into account in future work.

Optimization was performed by simulating a large number of unique configurations and selecting the best-performing ones for each target site. Field strength in the target areas could be at least doubled for all superficially located target areas, while improvements for field strength in the presumably most effective direction were much smaller. Results were markedly different for cortical areas that lie deeper within the brain. Due to the similarities and differences between optimization results for several target areas, general guidelines for electrode placement could be extracted based on local brain geometry.

## Measuring: Conventional versus optimized tDCS

The investigations were concluded by testing the efficacy of the model-based optimal configurations experimentally. The conventional and optimized configurations for M1 stimulation were compared by measuring corticospinal excitability before and after tDCS in healthy subjects. The theoretically optimal configuration for maximal field strength in the presumably most effective direction resulted in larger group-averaged effects than the conventional configuration; the configuration optimized for field strength was barely effective. However, individual results showed large differences that could not be explained by the model or differences in brain geometry. Subject- and session-specific influences on tDCS results should therefore be investigated further.

## 7.2 Discussion

---

In this section, the main findings of the studies presented in this thesis are discussed in relation to one another and put in a broader perspective, leading to indications for future research.

### Skull representation

Due to its low conductivity the skull strongly influences tDCS-induced current distributions. The skull was therefore realistically represented in all models in this thesis and its volume conduction effects were investigated in two studies. The hard and highly resistive human skull encompasses a layer of spongy tissue that conducts currents 3–4 times better on average<sup>[1]</sup>. As the spongiosa layer is very hard to visualize on an MR image, difficult to segment and to form closed surfaces of, most investigators have not included it in their models. Its anisotropic effect on the conductivity of the skull as a whole was instead ignored or approximated using anisotropic tensors. This thesis presented both a realistic geometry-adapted hexahedral (Chapter 3) and tetrahedral (Chapter 4) head model that contained an MRI-derived spongiosa layer, showing that with currently available techniques and a tailored MR sequence it is possible to realistically represent the spongiosa, regardless of the FE type. Obviously this is much easier for a hexahedral model.

As incorporating spongiosa into a model is still a time-consuming process, it is worthwhile to investigate whether this additional layer strongly affects the resulting field distribution. This thesis employed both a spherical (Chapter 2) and an

MRI-derived model (Chapter 3) to investigate these effects. Both models showed that ignoring or misrepresenting the spongiosa layer leads to a uniform decrease in current density in the brain when the electrodes are far apart (180-degree interelectrode angle in Chapter 2 and A1 stimulation in Chapter 3), while effects are more local for smaller distances (90-degree interelectrode angle in Chapter 2 and M1 stimulation in Chapter 3).

Having uniform layers throughout, a spherical model allows for adjustments of the conductivity values of the layers in such a way that equivalent values can be calculated and effects can be compared. Using this model it was found that, for all conductivity values tested, the influence of the layered structure was minimal when, and only when, using the equivalent anisotropic or isotropic conductivity values.

The real spongiosa layer varies in thickness throughout the skull and is absent in areas where the skull is thin. This inhomogeneity, which was shown to have a large influence in EEG forward modeling<sup>[31]</sup>, was not present in the spherical model. Simulations with an MRI-derived model with a realistically shaped spongiosa compartment showed that the effect of the spongiosa being present depends on the location of the target area and electrodes. It was concluded that it is important to model the skull realistically when the electrodes are placed over areas with a thick spongy layer.

Combining the findings of both studies, a final recommendation for skull modeling can be given. A separate spongiosa compartment should be included if the electrodes are placed over areas containing a substantial amount of spongiosa. The spongiosa can be segmented from MR or CT images. A more efficient and possibly only slightly less accurate method would be to create an approximated spongiosa compartment by eroding the skull surface by several voxels or millimeters. This approach was shown to work well in an EEG source localization study<sup>[156]</sup>, but its validity should be verified for tDCS simulations. If an electrode is placed over or near the top of the head this method should not be used, because there is quite a large hole in the spongiosa layer near the top of the skull (see Fig. 4.2). If creation of a spongiosa compartment is not feasible, a homogeneous isotropic representation with the equivalent radial conductivity value can be used. This equivalent value can be calculated from the average conductivities and thicknesses of the layers reported by Akhtari et al.<sup>[1]</sup>. It should be noted that this is only the best approach if the electrodes are placed over areas containing a considerable amount of spongiosa. Over areas without spongiosa, the skull conductivity is better represented by the conductivity of compact tissue. This inhomogeneity of the spongiosa can be included and investigated by giving each skull element in a layered skull model an equivalent conductivity value based on the local layer thicknesses. This approach was tested for

EEG source modeling<sup>[31]</sup>, but not yet for simulations of tDCS. If the layer thicknesses are not available throughout the model, but can be extracted from an MR image locally, it is recommended to use the value measured underneath the center of the stimulating electrode as the global value. As the measurements of Akhtari et al.<sup>[1]</sup> are still the only published measurements of the properties of the separate skull layers, only four subjects were measured and variability was high, more measurements are needed.

## Creating accurate yet efficient models

Additional to the representation of the skull, which was discussed above, the effects of including various other tissue compartments were investigated. The results in Chapter 3 showed that accurate modeling of the CSF, and therewith the brain surface, is very important in tDCS modeling. The distinction between gray and white matter significantly influences the orientation and magnitude of the current flow in the whole brain, but effects are smaller than for the CSF compartment. Representing WM anisotropy is important when considering deeper target regions, while it seems less important for superficial targets where no significant anisotropy exists between electrodes and targets. Simulations in Chapter 4 showed the influence of small structures like the eyes to be only marginal and negligible compared to other unavoidable small modeling errors. The conductivity of the muscle compartment did influence the results for cerebellar tDCS. It was not expected that including air-filled compartments representing the sinuses would have significantly affected the results.

A volume conductor model for tDCS should contain all important tissues located in between the electrodes and the target brain areas. Realistic isotropic representations of the skin, skull, CSF and GM are indispensable. Including a WM compartment is recommended as well. With the currently available software<sup>a</sup>, the segmentation of these compartments can be performed mostly automatically and should therefore not be a problem with regard to efficiency. For tetrahedral models, creating a closed WM surface that does not intersect with itself or the GM surface is quite a challenge. However, when fast model creation is an essential factor, such as when aiming for individualized models, one can assume that hexahedral models are preferred. As the brain areas most often targeted with tDCS lie on gyral crowns, WM anisotropy does not need to be included. Whether this also holds for the M1 leg area, which lies on a gyral crown within the interhemispheric fissure, needs further investigation. Cerebellar tDCS was not considered in the studies in Chapter 3. Because the investigations in Chapter 4 suggested that with cerebellar stimulation most of the

<sup>a</sup>See Chapters 3 and 4 for suggestions for hexahedral and tetrahedral models, respectively.



current is shunted around the brain, and there is no spongiosa in the area between the electrodes, both realistic WM and skull modeling seem unnecessary for this target region. As the conductivity values used here for skin ( $0.465 \text{ S/m}^{[160]}$ ) and muscle ( $0.4 \text{ S/m}^{[39]}$ ) lie close together, the neck muscles can be included into the skin compartment. Simulations of cerebellar tDCS could be improved by acquiring more knowledge on the conductivity of muscle tissue.

## Finite element model type

The first part of this thesis dealt with investigations of accuracy versus efficiency in creating volume conduction models for simulations of tDCS. Two extensive modeling studies considered including or ignoring certain tissue compartments and how to represent anisotropically conducting tissues. Another basic choice in creating a finite element model – deciding on the element type – was not considered in these studies. Two highly detailed realistic models were created for the work in this thesis: a geometry-adapted hexahedral (Chapter 3) and a tetrahedral (Chapter 4) model. Hexahedral models are by far the easiest to produce based on MR images and geometry-adapted hexahedral models can also be made fairly easily using the software described in Chapter 3, while building the tetrahedral model used here required much time and effort. However, currently pipelines exist in which a complete tetrahedral model can be built automatically from an MR data set<sup>[30]</sup>. Of course, such automated pipelines cannot include every detail, e.g. a spongiosa compartment is not modeled. As described above, alternative methods can be used for more appropriate skull representation. Nevertheless, tetrahedral models cannot (easily) include all structures, while hexahedral models can represent each tissue that can be segmented. The benefits of a tetrahedral model lie in the decreased computational requirement due to the smaller number of elements, and the more realistic and smooth surfaces as compared to hexahedral models. Surfaces in a hexahedral model are greatly improved using geometry adaptation, but are still less realistic than in a tetrahedral model (compare Fig. 3.1a with 4.3 for skin and 3.2f with 4.5 for GM). The question that arises is whether this difference in geometric accuracy does significantly affect the accuracy of the results. This can be investigated by comparing the results of a hexahedral model and a tetrahedral model of the same subject, which has not been done so far. Unfortunately the two models used in this thesis were based on different subjects. Future work should include a comparison on accuracy and efficiency for a hexahedral, geometry-adapted hexahedral and a tetrahedral model of the same subject.

## Conventional configurations

The electric field distributions resulting from the conventional tDCS configurations for auditory cortex (Chapter 3), the hand area of M1 (Chapters 3 and 4), the leg area of M1 (Chapter 5) and DLPFC, IFG and cerebellum (Chapter 4) were investigated in the various studies presented in this thesis. All configurations for superficial cortical target areas produced a single area of maximum field strength about halfway between the electrodes, except for the A1 setup. This configuration produced high current densities near both electrodes. It is not expected that this is due to the A1 configuration being symmetric, because the symmetric DLPFC setup produced dissimilar results. For the spherical model in Chapter 2 it was shown that smaller interelectrode angles lead to a shift in the current density distribution with the maxima moving from under the electrodes to halfway between them. It seems that this finding is consistent with the results for the realistic models. The A1 setup has approximately a  $180^\circ$  interelectrode angle, which produces two maxima under the electrodes. The other configurations all have electrodes with at most  $90^\circ$  between them, resulting in one central maximum. It is therefore expected that configurations with a large interelectrode angle (close to  $180^\circ$ ) in general do produce fields with maxima in the target area(s). As Chapter 5 showed that configurations with an electrode over the target area are (near-)optimal with regard to field direction, these  $180^\circ$  setups are actually optimal for both parameters.

Stimulation of the cerebellum and occipital cortex resulted in low field strengths in the target area. It seems that placing an electrode on the back of the head generally leads to large amounts of shunting. Dependent on the locations of the electrodes, currents are shunted through the interhemispheric fissure or through the muscle and skin on the side of the head. For both the occipital and cerebellar targets, optimally directed field strength was achieved by configurations with one electrode over the target and the other frontal and off-center. For target areas on the back of the head it is therefore recommended to place the reference electrode frontal and away from the midline to achieve maximal field strength in the presumably most effective direction.

## Low-frequency stimulation

The quasi-static approximation to Maxwell's equations is justified for modeling in the low-frequency regime (Section 1.2.1). Logothetis et al.<sup>[83]</sup> showed with in vivo direct measurements of the cortical impedance spectrum in monkey primary visual cortex that impedance is independent of frequency, is homogeneous and tangentially isotropic within gray matter, and can theoretically be predicted assuming a

pure-resistive conductor. Bossetti et al.<sup>[20]</sup> were able to demonstrate that the quasi-static approximation is fairly good even for rapid stimulation pulses using higher frequencies (above 1 kHz). They concluded that the modeling errors were much more dependent on the conductivity than on the permittivity of the medium. Therefore, it should be possible to generalize the findings in this thesis to at least low-frequency (e.g. below 100 Hz) transcranial alternating current stimulation (tACS). Changing the polarity of the tDCS electrodes results in identical spatial distributions with the vector directions flipped by  $180^\circ$ <sup>[160]</sup>. Since the problem is linear, results can be scaled to any desired input current simply by multiplying the current densities with the new current strength. Therefore, the current densities or electric fields during one half cycle of tACS can be derived from tDCS by scaling and for the other half cycle by scaling and flipping the orientation by  $180^\circ$ .

## 7.3 Future perspectives

---

Simulations of tDCS can provide information that is difficult or impossible to acquire otherwise. Assumptions that had been accepted by the experimental community have been proven wrong through modeling. For example it had been assumed, and still is by many experimenters, that the current distribution in the skin under the electrodes is uniform. This thesis and other simulation studies have shown that currents enter the skin at the perimeters of the electrodes (e.g. Fig. 2.2a and 4.5a). This can have consequences for the maximum allowable current strength in order to prevent possible skin damage. It had also been assumed that the conventional configurations produce maximal field strengths under the electrodes and therefore in the target areas. In this thesis it was shown consistently that for the most commonly targeted brain areas this is not at all the case.

As possible experimental variations in tDCS parameters are endless, simulations provide an efficient way to investigate new protocols and optimize stimulation. In this thesis, electrode placement was optimized for achieving maximal field strength in the target area or maximal field strength in the presumably most effective direction. The results of the optimization suggest that optimal configurations can be determined from MR images and that individualized simulations and optimization are not necessary. This is not the case when anatomical pathological perturbations are present, such as tumors, brain injuries or holes in the skull, and might not be the case for other optimization parameters. Future work can include optimization with multi-electrode setups to predict the optimal placement, number and shape of electrodes. Optimization can also include maximizing focality or avoiding unwanted

stimulation in non-targeted brain regions.

Highly realistic simulations and optimizations can currently be performed. However, in order to achieve maximal experimental effects, one needs to know what to optimize. As long as the working mechanisms behind the effects of tDCS are not fully understood, the practical implications of optimizations may be limited. On the other hand, the studies in this thesis have shown that by coupling models and measurements, information on the foundations of tDCS can be gained that could not have been acquired with experiments alone. Field strength and direction could not explain the individual experimental results, demonstrating that there is more to tDCS than sending a current in the right direction. Individual differences need to be investigated further in future studies. Coupling volume conduction modeling results to experiments or to cortical neuron (network) models can provide additional valuable information. In conclusion: while simulations of tDCS require more knowledge on the workings of the technique, they also help gain this information.







1. Akhtari, M., Bryant, H., Mamelak, A., Flynn, E., Heller, L., Shih, J., Mandelkern, M., Matlachov, A., DM, R., Best, E., DiMauro, M., Lee, R., & Sutherling, W. (2002). Conductivities of three-layer live human skull. *Brain Topogr*, 14(3), 151–67.
2. Albert, D. (1966). The effects of polarizing currents on the consolidation of learning. *Neuropsychologia*, 4(1), 65–77.
3. Antal, A., Boros, K., Poreisz, C., Chaieb, L., Terney, D., & Paulus, W. (2008). Comparatively weak after-effects of transcranial alternating current stimulation (tacs) on cortical excitability in humans. *Brain Stimul*, 1(2), 97–105.
4. Antal, A., Kincses, T., Nitsche, M., & Paulus, W. (2003). Manipulation of phosphene thresholds by transcranial direct current stimulation in man. *Exp Brain Res*, 150(3), 375–8.
5. Antal, A., Nitsche, M., Kincses, T., Kruse, W., Hoffmann, K., & Paulus, W. (2004). Facilitation of visuo-motor learning by transcranial direct current stimulation of the motor and extrastriate visual areas in humans. *Eur J Neurosci*, 19(10), 2888–92.
6. Antal, A., Terney, D., Poreisz, C., & Paulus, W. (2007). Towards unravelling task-related modulations of neuroplastic changes induced in the human motor cortex. *Eur J Neurosci*, 26(9), 2687–91.
7. Arfai, E., Theano, G., Montagu, J., & Robin, A. (1970). A controlled study of polarization in depression. *Br J Psychiatry*, 116(533), 433–4.
8. Bagshaw, A., Liston, A., Bayford, R., Tizzard, A., Gibson, A., Tidswell, A., Sparkes, M., Dehghani, H., Binnie, C., & Holder, D. (2003). Electrical impedance tomography of human brain function using reconstruction algorithms based on the finite element method. *Neuroimage*, 20(2), 752–64.
9. Baker, A. (1970). Brain stem polarization in the treatment of depression. *S Afr Med J*, 44(16), 473–5.
10. Barker, A., Jalinous, R., & Freeston, I. (1985). Non-invasive magnetic stimulation of human motor cortex. *Lancet*, 11(1), 1106–7.
11. Basser, P., Mattiello, J., & LeBihan, D. (1994). MR diffusion tensor spectroscopy and imaging. *Biophys J*, 66(1), 259–67.
12. Baumann, S., Wozny, D., Kelly, S., & Meno, F. (1997). The electrical conductivity of human cerebrospinal fluid at body temperature. *IEEE Trans Biomed Eng*, 44(3), 220–3.
13. Behrens, T., Woolrich, M., Jenkinson, M., Johansen-Berg, H., Nunes, R., Clare, S., Matthews, P., Brady, J., & Smith, S. (2003). Characterization and propagation of uncertainty in diffusion-weighted MR imaging. *Magn Reson Med*, 50(5), 1077–88.
14. Bienenstock, E., Cooper, L., & Munro, P. (1982). Theory for the development of neuron selectivity: orientation specificity and binocular interaction in visual cortex. *J Neurosci*, 2(1), 32–48.
15. Bindman, L., Lippold, O., & Redfearn, J. (1964). The action of brief polarizing currents on the cerebral cortex of the rat (1) during current flow and (2) in the production of long-lasting after-effects. *J Physiol*, 172(3), 369–82.
16. Boggio, P., Amancio, E., Correa, C., Cecilio, S., Valasek, C., Bajwa, Z., Freedman, S., Pascual-Leone, A., Edwards, D., & Fregni, F. (2009). Transcranial dc stimulation coupled with tens for the treatment of chronic pain: a preliminary study. *Clin J Pain*, 25(8), 691–5.
17. Boggio, P., Khoury, L., Martins, D., Martins, O., de Macedo, E., & Fregni, F. (2009). Temporal cortex direct current stimulation enhances performance on a visual recognition memory task in Alzheimer disease. *J Neurol Neurosurg Psychiatry*, 80(4), 444–7.
18. Boggio, P., Nunes, A., Rigonatti, S., Nitsche, M., Pascual-Leone, A., & Fregni, F. (2007). Repeated sessions of noninvasive brain dc stimulation is associated with motor function improvement in stroke patients. *Restor Neurol Neurosci*, 25(2), 123–9.
19. Boggio, P., Rigonatti, S., Ribeiro, R., Myczkowski, M., Nitsche, M., Pascual-Leone, A., & Fregni, F. (2008). A randomized, double-blind clinical trial on the efficacy of cortical direct current stimulation for the treatment of major depression. *Int J Neuropsychopharmacol*, 11(2), 249–54.



20. Bossetti, C., Birdno, M., & Grill, W. (2008). Analysis of the quasi-static approximation for calculating potentials generated by neural stimulation. *J Neural Eng*, 5(1), 44–53.
21. Bradnam, L., Stinear, C., Barber, P., & Byblow, W. (2012). Contralesional hemisphere control of the proximal paretic upper limb following stroke. *Cereb Cortex*, 22(11), 2662–71.
22. Camacho, D., Hopper, R., Lin, G., & Myers, B. (1997). An improved method for finite element mesh generation of geometrically complex structures with application to the skullbase. *J Biomech*, 30(10), 1067–70.
23. Cappelletti, M., Gessaroli, E., Hithersay, R., Mitolo, M., Didino, D., Kanai, R., Cohen Kadosh, R., & Walsh, V. (2013). Transfer of cognitive training across magnitude dimensions achieved with concurrent brain stimulation of the parietal lobe. *J Neurosci*, 33(37), 14899–907.
24. Carney, M. (1969). Negative polarisation of the brain in the treatment of manic states. *Ir J Med Sci*, 8(3), 133–5.
25. Carney, M., Cashman, M., & Sheffield, B. (1970). Polarization in depression. *Br J Psychiatry*, 117(539), 474–5.
26. Chatrian, G., Lettich, E., & Nelson, P. (1985). Ten percent electrode system for topographic studies of spontaneous and evoked EEG activity. *Am J EEG Technol*, 25, 83–92.
27. Costain, R., Redfearn, J., & Lippold, O. (1964). A controlled trial of the therapeutic effect of polarization of the brain in depressive illness. *Br J Psychiatry*, 110, 786–99.
28. Creutzfeldt, O., Fromm, G., & Kapp, H. (1962). Influence of transcortical d-c currents on cortical neuronal activity. *Exp Neurol*, 5(6), 436–52.
29. Cuffin, B. (1993). Effects of local variations in skull and scalp thickness on EEG's and MEG's. *IEEE Trans Biomed Eng*, 40(1), 42–8.
30. Dannhauer, M., Brooks, D., Tucker, D., & MacLeod, R. (2012). A pipeline for the simulation of transcranial direct current stimulation for realistic human head models using SCIRun/bioMesh3D. In *Conf Proc IEEE Eng Med Biol Soc*, (pp. 5486–9).
31. Dannhauer, M., Lanfer, B., Wolters, C., & Knösche, T. (2011). Modeling of the human skull in EEG source analysis. *Hum Brain Mapp*, 32(9), 1383–99.
32. Datta, A., Baker, J., Bikson, M., & Fridriksson, J. (2011). Individualized model predicts brain current flow during transcranial direct-current stimulation treatment in responsive stroke patient. *Brain Stimul*, 4(3), 169–74.
33. Datta, A., Bansal, V., Diaz, J., Patel, J., Reato, D., & Bikson, M. (2009). Gyri-precise head model of transcranial direct current stimulation: Improved spatial focality using a ring electrode versus conventional rectangular pad. *Brain Stimul*, 2(4), 201–7.
34. Datta, A., Elwassif, M., Battaglia, F., & Bikson, M. (2008). Transcranial current stimulation focality using disc and ring electrode configurations: Fem analysis. *J Neural Eng*, 5(2), 163–74.
35. Ditye, T., Jacobson, L., Walsh, V., & Lavidor, M. (2012). Modulating behavioral inhibition by tDCS combined with cognitive training. *Exp Brain Res*, 219(3), 363–8.
36. Dmochowski, J., Datta, A., Bikson, M., Su, Y., & Parra, L. (2011). Optimized multi-electrode stimulation increases focality and intensity at target. *J Neural Eng*, 8(4), 046011.
37. Elbert, T., Lutzenberger, W., Rockstroh, B., & Birbaumer, N. (1981). The influence of low-level transcortical DC-currents on response speed in humans. *Int J Neurosci*, 14(1–2), 101–14.
38. Enticott, P., Arnold, S., Fitzgibbon, B., Hoy, K., Susilo, D., & Fitzgerald, P. (2012). Transcranial direct current stimulation (tDCS) of the inferior frontal gyrus disrupts interpersonal motor resonance. *Neuropsychologia*, 50(7), 1628–31.
39. Faes, T., van der Meij, H., de Munck, J., & Heethaar, R. (1999). The electric resistivity of human tissues (100 Hz–10 MHz): a meta-analysis of review studies. *Physiol Meas*, 20(4), R1–10.
40. Fang, Q. & Boas, D. (2009). Tetrahedral mesh generation from volumetric binary and gray-scale

- images. In *Proc IEEE Int Symp Biomed Imaging*, (pp. 1142–5).
41. Faria, P., Hallett, M., & Miranda, P. (2011). A finite element analysis of the effect of electrode area and inter-electrode distance on the spatial distribution of the current density in tDCS. *J Neural Eng*, 8(6), 066017.
  42. Faria, P., Leal, A., & Miranda, P. (2009). Comparing different electrode configurations using the 10–10 international system in tDCS: a finite element model analysis. In *Conf Proc IEEE Eng Med Biol Soc*, (pp. 1596–9).
  43. Francis, J., Gluckman, B., & Schiff, S. (2003). Sensitivity of neurons to weak electric fields. *J Neurosci*, 23(19), 7255–61.
  44. Fregni, F., Boggio, P., Lima, M., Ferreira, M., Wagner, T., Rigonatti, S., Castro, A., Souza, D., Riberto, M., Freedman, S., Nitsche, M., & Pascual-Leone, A. (2006). A sham-controlled, phase II trial of transcranial direct current stimulation for the treatment of central pain in traumatic spinal cord injury. *Pain*, 122(1), 197–209.
  45. Fregni, F., Boggio, P., Mansur, C., Wagner, T., Ferreira, M., Lima, M., Rigonatti, S., Marcolin, M., Freedman, S., Nitsche, M., & Pascual-Leone, A. (2005). Transcranial direct current stimulation of the unaffected hemisphere in stroke patients. *Neuroreport*, 16(14), 1551–5.
  46. Fregni, F., Boggio, P., Nitsche, M., Bormpohl, F., Antal, A., Feredoes, E., Marcolin, M., Rigonatti, S., Silva, M., Paulus, W., & Pascual-Leone, A. (2005). Anodal transcranial direct current stimulation of prefrontal cortex enhances working memory. *Exp Brain Res*, 166(1), 23–30.
  47. Fregni, F., Boggio, P., Santos, M., Lima, M., Vieira, A., Rigonatti, S., Silva, M., Barbosa, E., Nitsche, M., & Pascual-Leone, A. (2006). Noninvasive cortical stimulation with transcranial direct current stimulation in Parkinsons disease. *Mov Disord*, 21(10), 1693–702.
  48. Fregni, F., Gimenes, R., Valle, A., Ferreira, M., Rocha, R., Natalle, L., Bravo, R., Rigonatti, S., Freedman, S., Nitsche, M., Pascual-Leone, A., & Boggio, P. (2006). A randomized, sham-controlled, proof of principle study of transcranial direct current stimulation for the treatment of pain in fibromyalgia. *Arthritis Rheum*, 54(12), 3988–98.
  49. Fregni, F. & Pascual-Leone, A. (2007). Technology insight: noninvasive brain stimulation in neurology—perspectives on the therapeutic potential of rTMS and tDCS. *Nat Clin Pract Neurol*, 3(7), 383–93.
  50. Fregni, F., Thome-Souza, S., Nitsche, M., Freedman, S., Valente, K., & Pascual-Leone, A. (2006). A controlled clinical trial of cathodal DC polarization in patients with refractory epilepsy. *Epilepsia*, 47(2), 335–342.
  51. Fricke, K., Seeber, A., Thirugnanasambandam, N., Paulus, W., Nitsche, M., & Rothwell, J. (2011). Time course of the induction of homeostatic plasticity generated by repeated transcranial direct current stimulation of the human motor cortex. *J Neurophysiol*, 105(3), 1141–9.
  52. Gabriel, C., Gabriel, S., & Corthout, E. (1996). The dielectric properties of biological tissues: I. Literature survey. *Phys Med Biol*, 41(11), 2231–49.
  53. Gabriel, S., Lau, R., & Gabriel, C. (1996). The dielectric properties of biological tissues: II. Measurements in the frequency range 10 Hz to 20 GHz. *Phys Med Biol*, 41(11), 2251–69.
  54. Galea, J., Jayaram, G., Ajagbe, L., & Celnik, P. (2009). Modulation of cerebellar excitability by polarity-specific noninvasive direct current stimulation. *J Neurosci*, 29(28), 9115–22.
  55. Groppa, S., Bergmann, T., Siems, C., Mölle, M., Marshall, L., & Siebner, H. (2010). Slow-oscillatory transcranial direct current stimulation can induce bidirectional shifts in motor cortical excitability in awake humans. *Neuroscience*, 166(4), 1219–25.
  56. Grundey, J., Thirugnanasambandam, N., Kaminsky, K., Drees, A., Skwirba, A., Lang, N., Paulus, W., & Nitsche, M. (2012). Neuroplasticity in cigarette smokers is altered under withdrawal and partially restituted by nicotine exposition. *J Neurosci*, 32(12), 4156–62.
  57. Güllmar, D., Haueisen, J., Eiselt, M., Giessler, F., Flemming, L., Anwander, A., Knösche, T., Wolters,

- C., DümpeImann, M., Tuch, D., & Reichenbach, J. (2006). Influence of anisotropic conductivity on EEG source reconstruction: Investigations in a rabbit model. *IEEE Trans Biomed Eng*, 53(9), 1841–50.
58. Halko, M., Datta, A., Plow, E., Scaturro, J., Bikson, M., & Merabet, L. (2011). Neuroplastic changes following rehabilitative training correlate with regional electrical field induced with tDCS. *Neuroimage*, 57(3), 885–91.
59. Hall, K., Hicks, R., & Hopkins, H. (1970). The effects of low level DC scalp positive and negative current on the performance of various tasks. *Br J Psychiatry*, 117(541), 689–91.
60. Hamada, M., Strigaro, G., Murase, N., Sadnicka, A., Galea, J., Edwards, M., & Rothwell, J. (2012). Cerebellar modulation of human associative plasticity. *J Physiol*, 590(10), 2365–74.
61. Haueisen, J., Ramon, C., Eiselt, M., Brauer, H., & Nowak, H. (1997). Influence of tissue resistivities on neuromagnetic fields and electric potentials studied with a finite element model of the head. *IEEE Trans Biomed Eng*, 44(8), 727–735.
62. Heidemann, R., Porter, D., Anwander, A., Feiweier, T., Heberlein, K., Knösche, T., & Turner, R. (2010). Diffusion imaging in humans at 7T using readout-segmented EPI and GRAPPA. *Magn Reson Med*, 64(1), 9–14.
63. Hess, C., Mills, K., & Murray, N. (1986). Magnetic stimulation of the human brain: facilitation of motor responses by voluntary contraction of ipsilateral and contralateral muscles with additional observations on an amputee. *Neurosci Lett*, 71(2), 235–40.
64. Holdefer, R., Sadleir, R., & Russell, M. (2006). Predicted current densities in the brain during transcranial electrical stimulation. *Clin Neurophysiol*, 117(6), 1388–1397.
65. Horvath, J., Carter, O., & Forte, J. (2014). Transcranial direct current stimulation: five important issues we aren't discussing (but probably should be). *Front Syst Neurosci*, 8(2), 1–8.
66. Hummel, F., Celnik, P., Giraux, P., Floel, A., Wu, W., Gerloff, C., & Cohen, L. (2005). Effects of non-invasive cortical stimulation on skilled motor function in chronic stroke. *Brain*, 128(3), 490–9.
67. Im, C., Jung, H., Choi, J., Lee, S., & Jung, K. (2008). Determination of optimal electrode positions for transcranial direct current stimulation (tDCS). *Phys Med Biol*, 53(11), N219–25.
68. Im, C., Park, J., Shim, M., Chang, W., & Kim, Y. (2012). Evaluation of local electric fields generated by transcranial direct current stimulation with an extracephalic reference electrode based on realistic 3D body modeling. *Phys Med Biol*, 57(8), 2137–50.
69. Iyer, M., Mattu, U., Grafman, J., Lomarev, M., Sato, S., & Wassermann, E. (2005). Safety and cognitive effect of frontal dc brain polarization in healthy individuals. *Neurology*, 64(5), 872–5.
70. Javadi, A. & Cheng, P. (2013). Transcranial direct current stimulation (tDCS) enhances reconsolidation of long-term memory. *Brain Stimul*, 6(4), 668–74.
71. Jayaram, G., Tang, B., Pallegadda, R., Vasudevan, E., Celnik, P., & Bastian, A. (2012). Modulating locomotor adaptation with cerebellar stimulation. *J Neurophysiol*, 107(11), 2950–7.
72. Jeffery, D., Norton, J., Roy, F., & Gorassini, M. (2007). Effects of transcranial direct current stimulation on the excitability of the leg motor cortex. *Exp Brain Res*, 182(2), 281–7.
73. Jenkinson, M., Beckmann, C., Behrens, T., Woolrich, M., & Smith, S. (2012). FSL. *Neuroimage*, 62(2), 782–90.
74. Jocks, I. (2013). The compositiones medicamentorum of scribonius largus. Master's thesis, University of Glasgow.
75. Jones, D. (2004). The effect of gradient sampling schemes on measures derived from diffusion tensor MRI: a Monte Carlo study. *Magn Reson Med*, 51(4), 807–15.
76. Kuo, H., Bikson, M., Datta, A., Minhas, P., Paulus, W., Kuo, M., & Nitsche, M. (2013). Comparing cortical plasticity induced by conventional and high-definition 4 x 1 ring tDCS: a neurophysiological study. *Brain Stimul*, 6(4), 644–8.
77. Lang, N., Nitsche, M., Paulus, W., Rothwell, J., & Lemon, R. (2004). Effects of transcranial direct current

- stimulation over the human motor cortex on corticospinal and transcallosal excitability. *Exp Brain Res*, 156(4), 439–43.
78. Law, S. (1993). Thickness and resistivity variations over the upper surface of the human skull. *Brain Topogr*, 6(2), 99–109.
  79. Leemans, A. & Jones, D. (2009). The B-matrix must be rotated when correcting for subject motion in DTI data. *Magn Reson Med*, 61(6), 1336–49.
  80. Lifshitz, K. & Harper, P. (1968). A trial of transcranial polarization in chronic schizophrenics. *Br J Psychiatry*, 114(510), 635–7.
  81. Lindenberg, R., Renga, V., Zhu, L., Nair, D., & Schlaug, G. (2010). Bihemispheric brain stimulation facilitates motor recovery in chronic stroke patients. *Neurology*, 75(24), 2176–2184.
  82. Lippold, O. & Redfearn, J. (1964). Mental changes resulting from the passage of small direct currents through the human brain. *Br J Psychiatry*, 110, 768–72.
  83. Logothetis, N., Kayser, C., & Oeltermann, A. (2007). In vivo measurement of cortical impedance spectrum in monkeys: implications for signal propagation. *Neuron*, 55(5), 809–23.
  84. Loo, C., Alonzo, A., Martin, D., Mitchell, P., Galvez, V., & Sachdev, P. (2012). Transcranial direct current stimulation for depression: 3-week, randomised, sham-controlled trial. *Br J Psychiatry*, 200(1), 52–9.
  85. López-Alonso, V., Cheeran, B., Río-Rodríguez, D., & Fernández-Del-Olmo, M. (2014). Inter-individual variability in response to non-invasive brain stimulation paradigms. *Brain Stimul*, 7(3), 372–80.
  86. Madhavan, S., Weber, K. n., & Stinear, J. (2011). Non-invasive brain stimulation enhances fine motor control of the hemiparetic ankle: implications for rehabilitation. *Exp Brain Res*, 209(1), 9–17.
  87. Maeoka, H., Matsuo, A., Hiyamizu, M., Morioka, S., & Ando, H. (2012). Influence of transcranial direct current stimulation of the dorsolateral prefrontal cortex on pain related emotions: A study using electroencephalographic power spectrum analysis. *Neurosci Lett*, 512(1), 12–6.
  88. Maes, F., Collignon, A., Vandermeulen, D., Marchal, G., & Suetens, P. (1997). Multimodality image registration by maximization of mutual information. *IEEE Trans Med Imaging*, 16(2), 187–98.
  89. Marangolo, P., Marinelli, C., Bonifazi, S., Fiori, V., Ceravolo, M., Provinciali, L., & Tomaiuolo, F. (2011). Electrical stimulation over the left inferior frontal gyrus (IFG) determines long-term effects in the recovery of speech apraxia in three chronic aphasics. *Behav Brain Res*, 225(2), 498–504.
  90. Marin, G., Guerin, C., Baillet, S., Garnero, L., & Meunier, G. (1998). Influence of skull anisotropy for the forward and inverse problem in EEG: Simulation studies using FEM on realistic head models. *Hum Brain Mapp*, 6(4), 250–269.
  91. Marshall, L., Helgadóttir, H., Mölle, M., & Born, J. (2006). Boosting slow oscillations during sleep potentiates memory. *Nature*, 444(7119), 610–3.
  92. Maxwell, J. (1865). A dynamical theory of the electromagnetic field. *Phil Trans R Soc Lond*, 155, 459–512.
  93. Meijs, J., Weier, O., Peters, M., & van Oosterom, A. (1989). On the numerical accuracy of the boundary element method. *IEEE Trans Biomed Eng*, 36(10), 1038–49.
  94. Merton, P., Hill, D., Morton, H., & Marsden, C. (1982). Scope of a technique for electrical stimulation of human brain, spinal cord, and muscle. *Lancet*, 2(8298), 597–600.
  95. Metuki, N., Sela, T., & Lavidor, M. (2012). Enhancing cognitive control components of insight problems solving by anodal tDCS of the left dorsolateral prefrontal cortex. *Brain Stimul*, 5(2), 110–5.
  96. Mills, K., Boniface, S., & Schubert, M. (1992). Magnetic brain stimulation with a double coil: the importance of coil orientation. *Electroencephalogr Clin Neurophysiol*, 85(1), 17–21.
  97. Miranda, P., Faria, P., & Hallett, M. (2009). What does the ratio of injected current to electrode area tell us about current density in the brain during tDCS? *Clin Neurophysiol*, 120(6), 1183–7.
  98. Miranda, P., Lomarev, M., & Hallett, M. (2006). Modeling the current distribution during transcranial

- direct current stimulation. *Clin Neurophysiol*, 117(7), 1623–9.
99. Miyaguchi, S., Onishi, H., Kojima, S., Sugawara, K., Tsubaki, A., Kirimoto, H., Tamaki, H., & Yamamoto, N. (2013). Corticomotor excitability induced by anodal transcranial direct current stimulation with and without non-exhaustive movement. *Brain Res*, 1529, 83–91.
  100. Montenegro, R., Okano, A., Cunha, F., Gurgel, J., Fontes, E., & Farinatti, P. (2012). Prefrontal cortex transcranial direct current stimulation associated with aerobic exercise change aspects of appetite sensation in overweight adults. *Appetite*, 58(1), 333–8.
  101. Munck de, J. & Peters, M. (1993). A fast method to compute the potential in the multi-sphere model. *IEEE Trans Biomed Eng*, 40(11), 1166–74.
  102. Nadeem, M., Thorlin, T., Gandhi, O., & Persson, M. (2003). Computation of electric and magnetic stimulation in human head using the 3-D impedance method. *IEEE Trans Biomed Eng*, 50(7), 900–7.
  103. Neuling, T., Rach, S., Wagner, S., Wolters, C., & Herrmann, C. (2012). Good vibrations: oscillatory phase shapes perception. *Neuroimage*, 63(2), 771–8.
  104. Nitsche, M., Cohen, L., Wassermann, E., Priori, A., Lang, N., Antal, A., Paulus, W., Hummel, F., Boggio, P., Fregni, F., & Pascual-Leone, A. (2008). Transcranial direct current stimulation: State of the art 2008. *Brain Stimul*, 1(3), 206–23.
  105. Nitsche, M., Doemkes, S., Karaköse, T., Antal, A., Liebetanz, D., Lang, N., Tergau, F., & Paulus, W. (2007). Shaping the effects of transcranial direct current stimulation of the human motor cortex. *J Neurophysiol*, 97(4), 3109–17.
  106. Nitsche, M., Koschack, J., Pohlers, H., Hulleman, S., Paulus, W., & Happe, S. (2012). Effects of frontal transcranial direct current stimulation on emotional state and processing in healthy humans. *Front Psychiatry*, 3(58), doi:10.3389/fpsy.2012.00058.
  107. Nitsche, M., Nitsche, M., Klein, C., Tergau, F., Rothwell, J., & Paulus, W. (2003). Level of action of cathodal DC polarisation induced inhibition of the human motor cortex. *Clin Neurophysiol*, 114(4), 600–4.
  108. Nitsche, M. & Paulus, W. (2000). Excitability changes induced in the human motor cortex by weak transcranial direct current stimulation. *J Physiol*, 527(3), 633–9.
  109. Nitsche, M. & Paulus, W. (2001). Sustained excitability elevations induced by transcranial DC motor cortex stimulation in humans. *Neurology*, 57(10), 1899–1901.
  110. Oh, S., Lee, S., Cho, M., Kim, T., & Kim, I. (2006). Electrical conductivity estimation from diffusion tensor and T2: a silk yarn phantom study. *Proc Intl Soc Mag Reson Med*, 14, 30–4.
  111. Oostendorp, T., Hengeveld, Y., Wolters, C., Stinstra, J., van Elswijk, G., & Stegeman, D. (2008). Modeling transcranial DC stimulation. In *Conf Proc IEEE Eng Med Biol Soc*, (pp. 4226–9).
  112. Opitz, A., Windhoff, M., Heidemann, R., Turner, R., & Thielscher, A. (2011). How the brain tissue shapes the electric field induced by transcranial 2 magnetic stimulation. *Neuroimage*, 58(3), 849–59.
  113. Parazzini, M., Fiocchi, S., & Ravazzani, P. (2012). Electric field and current density distribution in an anatomical head model during transcranial direct current stimulation for tinnitus treatment. *Bioelectromagnetics*, 33(6), 476–87.
  114. Parazzini, M., Fiocchi, S., Rossi, E., Paglialonga, A., & Ravazzani, P. (2011). Transcranial direct current stimulation: estimation of the electric field and of the current density in an anatomical human head model. *IEEE Trans Biomed Eng*, 58(6), 1773–80.
  115. Parent, A. (2004). Giovanni Aldini: from animal electricity to human brain stimulation. *Can J Neurol Sci*, 31(4), 576–84.
  116. Park, J., Hong, S., Kim, D., Suh, M., & Im, C. (2011). A novel array-type transcranial direct current stimulation (tDCS) system for accurate focusing on targeted brain areas. *IEEE Trans Magn*, 47(5), 882–5.
  117. Pisoni, A., Papagno, C., & Cattaneo, Z. (2012). Neural correlates of the semantic interference effect:

- New evidence from transcranial direct current stimulation. *Neuroscience*, 223, 56–67.
118. Plonsey, R. & Heppner, D. (1967). Considerations of quasi-stationarity in electrophysiological systems. *Bull Math Biophys*, 29(4), 657–64.
  119. Plow, E., Obretenova, S., Jackson, M., & Merabet, L. (2012). Temporal profile of functional visual rehabilitative outcomes modulated by transcranial direct current stimulation. *Neuromodulation*, 15(4), 367–73.
  120. Pohlmeier, R., Buchner, H., Knoll, G., Rienäcker, A., Beckmann, R., & Pesch, J. (1997). The influence of skull-conductivity misspecification on inverse source localization in realistically shaped finite element head models. *Brain Topogr*, 9(3), 157–62.
  121. Polson, M., Barker, A., & Freeston, I. (1982). Stimulation of nerve trunks with time-varying magnetic fields. *Med Biol Eng Comput*, 20(2), 243–4.
  122. Priori, A. (2003). Brain polarization in humans: a reappraisal of an old tool for prolonged non-invasive modulation of brain excitability. *Clin Neurophysiol*, 114(4), 589–95.
  123. Priori, A., Berardelli, A., Rona, S., Accornero, N., & Manfredi, M. (1998). Polarization of the human motor cortex through the scalp. *Neuroreport*, 9(10), 2257–60.
  124. Priori, A., Mameli, F., Cogiamanian, F., Marceglia, S., Tiriticco, M., Mrakic-Sposta, S., Ferrucci, R., Zago, S., Polezzi, D., & Sartori, G. (2008). Lie-specific involvement of dorsolateral prefrontal cortex in deception. *Cereb Cortex*, 18(2), 451–5.
  125. Purpura, D. & McMurtry, J. (1965). Intracellular activities and evoked potential changes during polarization of motor cortex. *J Neurophysiol*, 28, 166–85.
  126. Quartarone, A., Morgante, F., Bagnato, S., Rizzo, V., Sant'Angelo, A., Aiello, E., Reggio, E., Battaglia, F., Messina, C., & Girlanda, P. (2004). Long lasting effects of transcranial direct current stimulation on motor imagery. *Neuroreport*, 15(8), 1287–91.
  127. Radman, T., Datta, A., Ramos, R., Brumberg, J., & Bikson, M. (2009). One-dimensional representation of a neuron in a uniform electric field. In *Conf Proc IEEE Eng Med Biol Soc*, (pp. 6481–4).
  128. Ramon, C., Haueisen, J., & Schimpf, P. (2006). Influence of head models on neuromagnetic fields and inverse source localizations. *Biomed Eng Online*, 5(55).
  129. Ramon, C., Schimpf, P., & Haueisen, J. (2006). Influence of head models on EEG simulations and inverse source localizations. *Biomed Eng Online*, 5(10).
  130. Ramon, C., Schimpf, P., Haueisen, J., Holmes, M., & Ishimaru, A. (2004). Role of soft bone, CSF and gray matter in EEG simulations. *Brain Topogr*, 16(4), 245–8.
  131. Rampersad, S., Oostendorp, T., & Stegeman, D. (2014). Model-based optimization of bipolar tDCS electrode placement. *Under review*.
  132. Rampersad, S., Stegeman, D., & Oostendorp, T. (2013). Single-layer skull approximations perform well in transcranial direct current stimulation modeling. *IEEE Trans Neural Syst Rehabil Eng*, 21(3), 346–53.
  133. Redfearn, J., Lippold, O., & Costain, R. (1964). A preliminary account of the clinical effects of polarizing the brain in certain psychiatric disorders. *Br J Psychiatry*, 110, 773–85.
  134. Roche, N., Lackmy, A., Achache, V., Bussel, B., & Katz, R. (2012). Effects of anodal tDCS on lumbar propriospinal system in healthy subjects. *Clin Neurophysiol*, 123(5), 1027–34.
  135. Rosen, S. & Stamm, J. (1972). Transcortical polarization: facilitation of delayed response performance by monkeys. *Exp Neural*, 35(2), 282–9.
  136. Rullmann, M., Anwander, A., Dannhauer, M., Warfield, S., Duffy, F., & Wolters, C. (2009). EEG source analysis of epileptiform activity using a 1 mm anisotropic hexahedra finite element head model. *Neuroimage*, 44(2), 399–410.
  137. Rush, S. & Driscoll, D. (1968). Current distribution in the brain from surface electrodes. *Anesth Analg*, 47(6), 717–23.

138. Rushton, W. (1927). Effect upon the threshold for nervous excitation of the length of nerve exposed and the angle between current and nerve. *J Physiol*, 63(4), 357–77.
139. Ruthotto, L., Kugel, H., Olesch, J., Fischer, B., Modersitzki, J., Burger, M., & Wolters, C. (2012). Diffeomorphic susceptibility artifact correction of diffusion-weighted magnetic resonance images. *Phys Med Biol*, 57(18), 5715–31.
140. Sadleir, R., Vannorsdall, T., Schretlen, D., & Gordon, B. (2010). Transcranial direct current stimulation (tDCS) in a realistic head model. *Neuroimage*, 51(4), 1310–18.
141. Sadleir, R., Vannorsdall, T., Schretlen, D., & Gordon, B. (2012). Target optimization in transcranial direct current stimulation. *Front Psychiatry*, 3(90), doi: 10.3389/fpsy.2012.00090.
142. Salvador, R., Mekonnen, A., Ruffini, G., & Miranda, P. (2010). Modeling the electric field induced in a high resolution realistic head model during transcranial current stimulation. In *Conf Proc IEEE Eng Med Biol Soc*, (pp. 2073–6).
143. Schmidt, S., Cichy, R., Kraft, A., Brocke, J., Irlbacher, K., & Brandt, S. (2009). An initial transient-state and reliable measures of corticospinal excitability in TMS studies. *Clin Neurophysiol*, 120(5), 987–93.
144. Schwan, H. & Kay, C. (1957). Capacitive properties of body tissues. *Circ Res*, 5(4), 439–43.
145. Shahid, S., Wen, P., & Ahfock, T. (2013). Numerical investigation of white matter anisotropic conductivity in defining current distribution under tDCS. *Comput Methods Programs Biomed*, 109(1), 48–64.
146. Siniatchkin, M., Sendacki, M., Moeller, F., Wolff, S., Jansen, O., Siebner, H., & Stephani, U. (2012). Abnormal changes of synaptic excitability in migraine with aura. *Cereb Cortex*, 22(10), 2207–16.
147. Stagg, C. & Nitsche, M. (2011). Physiological basis of transcranial direct current stimulation. *Neuroscientist*, 17(1), 37–53.
148. Suh, H., Kim, S., Lee, W., & Kim, T. (2009). Realistic simulation of transcranial direct current stimulation via 3-d high-resolution finite element analysis: Effect of tissue anisotropy. In *Conf Proc IEEE Eng Med Biol Soc*, (pp. 638–41).
149. Suh, H., Lee, W., & Kim, T. (2012). Influence of anisotropic conductivity in the skull and white matter on transcranial direct current stimulation via an anatomically realistic finite element head model. *Phys Med Biol*, 57(21), 6961–80.
150. Szeligo, F. (1976). Electrophysiological and behavioral effects of transcortical polarizing current: comparison with the behaviorally determined characteristics of learning. *Brain Res*, 103(3), 463–75.
151. Tang, C., You, F., Cheng, G., Gao, D., Fu, F., Yang, G., & Dong, X. (2008). Correlation between structure and resistivity variations of the live human skull. *IEEE Trans Biomed Eng*, 55(9), 2286–92.
152. Taubin, G. (1995). A signal processing approach to fair surface design. In *Proc Conf Comput Graph Inter Techn*, (pp. 351–8).
153. Terney, D., Chaieb, L., Moliadze, V., Antal, A., & Paulus, W. (2008). Increasing human brain excitability by transcranial high-frequency random noise stimulation. *J Neurosci*, 28(52), 14147–55.
154. Thevenet, M., Bertrand, O., Perrin, F., Dumont, T., & Pernier, J. (1991). The finite element method for a realistic head model of electrical brain activities: preliminary results. *Clin Phys Physiol Meas*, 12(Suppl A), 89–94.
155. Tuch, D., Wedeen, V., Dale, A., George, J., & Belliveau, J. (2001). Conductivity tensor mapping of the human brain using diffusion tensor MRI. *Proc Natl Acad Sci U S A*, 98(20), 11697–701.
156. V, M.-R., van Mierlo, P., Strobbe, G., Staelens, S., Vandenberghe, S., & Hallez, H. (2014). Influence of skull modeling approaches on eeg source localization. *Brain Topogr*, 27(1), 95–111.
157. Vallaghé, S. & Clerc, M. (2009). A global sensitivity analysis of three- and four-layer EEG conductivity models. *IEEE Trans Biomed Eng*, 56(4), 988–95.
158. Vese, L. & Chan, T. (2002). A multiphase level set framework for image segmentation using the Mumford and Shah model. *Int J Comput Vis*, 50(3), 271–93.

159. Wagner, S. (2011). An adjoint FEM approach for the EEG forward problem. Master's thesis, University of Münster.
160. Wagner, T., Fregni, F., Fecteau, S., Grodzinsky, A., Zahn, M., & Pascual-Leone, A. (2007). Transcranial direct current stimulation: A computer-based human model study. *Neuroimage*, 35(3), 1113–24.
161. Whitaker, H., Smith, C., & Finger, S. (2007). *Brain, Mind and Medicine: essays in Eighteenth-Century Neuroscience*. Springer.
162. Wiethoff, S., Hamada, M., & Rothwell, J. (2014). Variability in response to transcranial direct current stimulation of the motor cortex. *Brain Stimul*, 7(3), 468–75.
163. Windhoff, M., Opitz, A., & Thielscher, A. (2013). Electric field calculations in brain stimulation based on finite elements: An optimized processing pipeline for the generation and usage of accurate individual head models. *Hum Brain Mapp*, 34(4), 923–35.
164. Wolters, C. (2003). *Influence of Tissue Conductivity Inhomogeneity and Anisotropy on EEG/MEG based Source Localization in the Human Brain*. PhD thesis, MPI of Cognitive Neuroscience Leipzig.
165. Wolters, C., Anwander, A., Berti, G., & Hartmann, U. (2007). Geometry-adapted hexahedral meshes improve accuracy of finite-element-method-based EEG source analysis. *IEEE Trans Biomed Eng*, 54(8), 1446–53.
166. Zaehle, T., Rach, S., & Herrmann, C. (2010). Transcranial alternating current stimulation enhances individual alpha activity in human EEG. *PLoS One*, 5(11), e13766.
167. Zandieh, A., Parhizgar, S., Fakhri, M., Taghvaei, M., Miri, S., Shahbabaie, A., Esteghamati, S., & Ekhtiari, H. (2012). Modulation of cold pain perception by transcranial direct current stimulation in healthy individuals. *Neuromodulation*, 16(4), 345–8.









# Elektrische hersenstimulatie

---

Al minstens 2000 jaar wordt elektriciteit toegepast als medische behandeling. Voor- dat elektriciteit in zijn huidige vorm beschikbaar was, werd gebruik gemaakt van levende vissen met een elektrisch orgaan. Kortdurende elektrische schokjes op het hoofd bleken onder anderen hoofdpijn en depressie te kunnen verminderen. Pas in de twintigste eeuw werden er systematische wetenschappelijke studies uitgevoerd die ons meer leerden over de effecten van elektriciteit op het brein. Zo bleek dat zelfs een zeer zwakke stroom die via de huid door de hersenen wordt gestuurd al effect heeft en dat deze effecten afhankelijk zijn van zowel de sterkte, duur als de richting van de stroom.

## Meten aan het zenuwstelsel

Ons hele zenuwstelsel, waaronder onze hersenen, bestaat uit een netwerk van vele miljarden neuronen. Dit zijn cellen waarvan de uiteinden met elkaar in verbinding staan, waardoor ze via elektrische of chemische signalen met elkaar communiceren. In de jaren '80 werd een nieuwe techniek ontwikkeld om metingen te doen aan het menselijke zenuwstelsel: *transcranial magnetic stimulation* (TMS). TMS is het zenden van een korte stroompuls door een spoel die tegen het hoofd wordt gehouden. Op deze manier wordt een magnetisch veld opgewekt dat probleemloos door de schedel kan dringen. Hierdoor wordt in de *cortex*, de buitenste laag van de hersenen, via een elektrisch veld een stroompje opgewekt in de neuronen. De cortex is verdeeld in gebieden met verschillende functies. Zo is de *motorische cortex* verantwoordelijk voor de aansturing van onze spieren. Als de TMS puls wordt gegeven boven de motorische cortex kan het opgewekte stroompje via zenuwbannen in ruggenmerg, armen en benen worden doorgegeven aan een spier en daar een samentrekking veroorzaken. De bijbehorende elektrische activiteit in de spier kan nauwkeurig worden gemeten door middel van elektrodes op de huid boven de spier: *elektromyografie* (EMG). Een schematische voorstelling van dergelijke metingen is weergegeven in Figuur 1.3 (p. 6). De sterkte van het EMG signaal boven de spier is een maat voor hoe makkelijk de neuronen in de cortex waarin het stroompje door TMS werd opgewekt kunnen worden geactiveerd: de *exciteerbaarheid*. De ontdekking van TMS heeft een grote invloed gehad op de ontwikkeling van verschillende vormen van elektrische hersenstimulatie. Dergelijke stimulatie kan namelijk een verandering teweeg brengen in de exciteerbaarheid van neuronen. Door middel van TMS en EMG konden deze effecten voor het eerst objectief worden gemeten.

## Beïnvloeden van het zenuwstelsel

Een vorm van elektrische hersenstimulatie die sinds de opkomst van TMS sterk is gegroeid is *transcranial direct current stimulation* (tDCS). Deze methode is het onderwerp van dit proefschrift. De meest voorkomende toepassing van tDCS bestaat uit het zenden van een zwakke (1–2 mA) constante stroom door het hoofd door middel van twee grote (25–35 cm<sup>2</sup>) rechthoekige elektrodes op de hoofdhuid gedurende een periode van 5 tot 20 minuten. De ene elektrode, de *anode*, heeft een hogere elektrische potentiaal ten opzichte van de andere, de *kathode*. Door dit potentiaalverschil gaat er een stroom lopen van de anode, via de huid, schedel en hersenen, naar de kathode. Deze stroom kan tijdelijke veranderingen teweeg brengen in de werking van neuronen. Het effect hiervan is afhankelijk van welk hersengebied gestimuleerd wordt. Het is gebruikelijk om één elektrode te plaatsen boven het hersengebied dat men wil beïnvloeden en de andere op het voorhoofd of de wang. In veel gevallen blijken de effecten omkeerbaar als de anode en kathode worden verwisseld.

Het effect van tDCS stimulatie op de motorische cortex kan bepaald worden door voor en na de stimulatie een meting te verrichten van de exciteerbaarheid via TMS en EMG. Studies met gezonde proefpersonen hebben aangetoond dat door tDCS toe te passen met de anode over de motorische cortex en de kathode op het voorhoofd<sup>a</sup> de exciteerbaarheid van de motorische cortex toenam. Door te stimuleren met de kathode over de motorische cortex nam de exciteerbaarheid juist af. De richting van de stroom, die omdraait door de anode en kathode te verwisselen, bepaalt dus mede wat voor effect er optreedt. Daarnaast zijn de effecten die optreden groter naarmate de stroomsterkte van de stimulatie groter is. Ook blijven de effecten langer aan naarmate de stimulatie duurt langer. De effecten houden aan nadat de stimulatie is gestopt, waarna de exciteerbaarheid meestal binnen een uur weer op het basisniveau is.

Door tDCS toe te passen over verschillende hersengebieden zijn effecten gevonden op uiteenlopende functies en aandoeningen zoals migraine, depressie, verslaving en taalverwerking<sup>b</sup>. Helaas zijn deze effecten vaak klein of van korte duur. Daar tDCS een zeer veilige en makkelijk te gebruiken techniek is met vele mogelijke toepassingen is het van belang de effecten te onderzoeken en proberen te verbeteren. Dit was het doel van de in dit proefschrift beschreven studies. Mogelijkheden tot verbetering zijn te vinden in het aanpassen van de sterkte en duur van de stroom, en de vorm, grootte en plaatsing van de elektrodes. Omdat het onmogelijk is de eindeloze hoeveelheid variaties experimenteel te testen, kan gebruik worden gemaakt van computermodellen om de resultaten te simuleren.

<sup>a</sup>Zie Figuur 4.3a op pagina 76 voor een illustratie.

<sup>b</sup>Zie Tabel 1.1 op pagina 10 voor een compleet overzicht.

## Simuleren van hersenstimulatie

---

Tijdens tDCS worden elektrische velden en stromen opgewekt in het hoofd door twee elektrodes op de hoofdhuid. De richting en sterkte van deze velden bepalen mede hoe sterk de neuronen in een bepaald hersengebied beïnvloed worden. Als we weten hoe deze velden eruit zien in de hersenen kunnen we deze informatie gebruiken om de effecten van tDCS beter te begrijpen en mogelijk de techniek te verbeteren. Hieronder wordt beschreven hoe met behulp van zogenaamde volumegeleidingsmodellen en de beroemde vergelijkingen van Maxwell deze velden berekend kunnen worden.

De vergelijkingen van Maxwell<sup>a</sup> beschrijven onder andere de relaties tussen elektrische velden, ladingen en stromen. Met behulp van deze vergelijkingen kan voor ieder plekje in een bepaald voorwerp uitgerekend worden hoe groot en sterk het elektrische veld is ten gevolge van een lading op het voorwerp. Voor een voorwerp met een simpele vorm, zoals een koperen bol, zijn deze vergelijkingen eenvoudig rechtstreeks op te lossen. Voor een ingewikkelde vorm, zoals een hoofd, is dit onmogelijk. De oplossing kan echter wel worden benaderd door een computermodel te maken waarin de ingewikkelde vorm is opgebouwd uit kleine bouwsteentjes met een simpele vorm. Een weergave van een dergelijk model ziet eruit als een hoofd gemaakt van Lego blokjes. De bouwsteentjes kunnen echter verschillende vormen hebben. In Figuur 1.7d (p. 21) is te zien hoe een hoofd in de computer kan worden nagebootst door het op te bouwen uit elementen in de vorm van *tetraeders*<sup>b</sup>. Dergelijke modellen zijn gebruikt voor het onderzoek beschreven in dit proefschrift. Om het elektrische veld in het hoofd nauwkeurig te kunnen berekenen moet het model de vorm van de verschillende weefsels, zoals huid, schedel en hersenen, zo waarheidsgetrouw mogelijk representeren. Met behulp van MRI scans<sup>c</sup> kan een driedimensionaal beeld gevormd worden van een hoofd. Dit beeld wordt in de computer omgezet in een model van blokjes, waarbij van ieder blokje bekend is welk weefseltype het representeert. Vervolgens kan aan ieder weefseltype de bijbehorende *geleidbaarheid* worden toegekend. De geleidbaarheid is een getal dat aangeeft hoe goed een materiaal elektriciteit geleidt. Er wordt veel onderzoek gedaan om de geleidbaarheid van menselijke weefsels zo nauwkeurig mogelijk te bepalen. Deze complete beschrijving van de vorm en geleidende eigenschappen van een hoofd is een *volumegeleidingsmodel*.

---

<sup>a</sup>Zie vergelijking 1.1 op pagina 12.

<sup>b</sup>Een tetraeder is een piramide waarvan het grondvlak een driehoek is.

<sup>c</sup>Zie Figuur 1.7a op pagina 21 voor een voorbeeld.

## Onderzoek in dit proefschrift

---

Dit proefschrift beschrijft vijf studies die gezamenlijk als doel hadden de effecten van tDCS op de hersenen te onderzoeken en verbeteren. Hiervoor is gebruik gemaakt van geavanceerde volumegeleidingsmodellen, waarvan de resultaten uiteindelijk getest zijn met behulp van gezonde proefpersonen.

### Detail en efficiëntie van volumegeleidingsmodellen

Met de huidige technologische mogelijkheden kunnen zeer gedetailleerde modellen gemaakt worden, waarin steeds meer verschillende weefsels kunnen worden gerepresenteerd met een meer en meer waarheidsgetrouwe vorm. De bouwsteentjes waaruit het model bestaat moeten daarvoor wel steeds kleiner worden, leidend tot een groter aantal steentjes en een langere rekentijd. Daarnaast is het maken van een gedetailleerd model een intensief en tijdrovend proces. Sommige van deze details hebben slechts een klein effect op de accuraatheid van de oplossing. Het is dan ook belangrijk om de balans te vinden tussen mate van detail en efficiëntie. Het eerste deel van dit proefschrift beschrijft twee studies waarin de effecten van bepaalde details werden onderzocht om te kunnen bepalen of ze noodzakelijk zijn voor een accurate oplossing.

In Hoofdstuk 2 werd onderzocht hoe de schedel het beste kan worden gepresenteerd in een volumegeleidingsmodel van tDCS. De menselijke schedel bestaat uit drie lagen waarvan de binnenste laag elektriciteit veel beter geleidt dan de twee buitensten. Dit leidt ertoe dat een groot deel van de stroom die vanaf de anode in de schedel terecht komt, via de binnenste laag wordt afgevoerd naar de kathode en nooit de hersenen bereikt. Een materiaal dat stroom beter geleidt in één richting dan in de anderen wordt *anisotroop* genoemd. De anisotrope schedel heeft een grote invloed op de tDCS stroom en een correcte representatie in een model kan dus ook van groot belang zijn. Omdat het erg moeilijk is de drie dunne schedellagen in een model weer te geven, wordt de schedel in tDCS modellen altijd benaderd als één laag met een gemiddelde geleidbaarheid of één laag waarbij de *anisotrope* geleidbaarheid middels een wiskundige techniek wordt nagebootst. Voor dit hoofdstuk werd een serie modellen gemaakt waarin alleen de schedel verschillend was. Op deze manier kon een model met drie schedellagen vergeleken worden met de verschillende benaderingsmodellen. In deze studie werd aangetoond dat het niet nodig is de drie lagen expliciet te modelleren, mits de gemiddelde geleidbaarheid die wordt gebruikt op een juiste manier gebaseerd wordt op het anisotrope karakter

van de geleidbaarheid.

In Hoofdstuk 3 werd onderzoek gedaan naar de effecten die het toevoegen van verschillende weefsels heeft op de stromen in de hersenen. Hiervoor werd een model gemaakt dat alle details die in eerdere studies zijn bekeken voor het eerst samenbrengt in één model. Om de effecten van ieder weefsel te kunnen isoleren werden stap voor stap details toegevoegd en steeds opnieuw de door tDCS opgewekte stromen berekend. Er werd onderzoek gedaan naar de invloed van de schedel, hersenvocht, grijze en witte stof en de anisotrope geleidbaarheid van sommige weefsels. Dit onderzoek resulteerde in een serie figuren (zie onder andere Figuur 3.1 op pagina 52) die zeer nauwkeurig weergeven hoe de stromen lopen bij standaard toepassingen van tDCS gericht op de motorische en auditieve cortex (het gedeelte van de hersenen dat geluiden verwerkt). In deze figuren konden we zien dat een groot deel van de stroom via de huid, schedel en het hersenvocht langs de hersenen af wordt gevoerd zonder de neuronen te bereiken. Uiteindelijk konden we concluderen dat het voor een accurate oplossing in het doelgebied vooral van belang is de weefsels die zich tussen de anode en kathode bevinden realistisch weer te geven, terwijl andere delen van het hoofd met minder detail benaderd kunnen worden.

De resultaten van Hoofdstuk 2 en 3 uit dit proefschrift brengen 1) nieuwe informatie over hoe de elektrische stromen tijdens tDCS door het hoofd lopen en kunnen daardoor bijdragen aan het begrip van hoe de effecten van tDCS ontstaan, 2) adviezen over hoe simulaties met volumegeleidingsmodellen van tDCS zo efficiënt en accuraat mogelijk kunnen worden uitgevoerd.

## Onderzoeken en optimaliseren van tDCS elektrodeplaatsing

Voor het tweede deel van dit proefschrift werd een nieuw hoofdmodel gemaakt dat het tot op heden meest nauwkeurige volumegeleidingsmodel is van tDCS. Met dit model werden simulaties uitgevoerd van een aantal veelgebruikte tDCS *configuraties* (plaatsing van de elektrodes). Daar de elektrische velden die deze configuraties produceerden in de simulaties niet optimaal bleken te zijn, werd het model vervolgens gebruikt om nieuwe verbeterde configuraties te vinden.

Onderzoekers gebruiken tDCS om verschillende hersengebieden te stimuleren. Hierbij wordt de aanname gebruikt dat het elektrische veld maximaal is recht onder de elektrode en dat de stimulatie dus het meest effectief is als de elektrode recht boven het doelgebied wordt geplaatst. In Hoofdstuk 4 werd onderzocht of dit daadwerkelijk zo is. Met behulp van een gedetailleerd hoofdmodel werd tDCS gesimuleerd voor zes van de meest gebruikte configuraties die gebruikt worden om verschillende hersengebieden te stimuleren. Voor vijf van deze configuraties werd gevonden dat een maximale veldsterkte werd bereikt in een hersengebied midden



tussen de elektrodes, ver van het doelgebied (zie Figuur 4.6a-e (p. 81)). Deze bevinding suggereert dat de effecten van tDCS verbeterd zouden kunnen worden door configuraties te vinden die wél een maximale veldsterkte opleveren in het doelgebied.

Hoofdstuk 5 beschrijft de zoektocht naar deze optimale configuraties. De eerste stap bestond uit het simuleren van duizenden tDCS configuraties met het nauwkeurige hoofdmodel. Daarna werden zes doelgebieden in de hersenen geselecteerd die regelmatig met behulp van tDCS worden onderzocht. Voor ieder van deze doelgebieden werd een selectie gemaakt van de configuraties die de meest optimale elektrische velden produceerden in de simulaties. Hierbij werd gezocht naar configuraties die een maximale veldsterkte opleverden in het doelgebied. Omdat niet exact bekend is welke factor bepalend is voor de effecten van tDCS, werd een tweede optimalisatie gedaan waarbij ook de richting van het veld werd geoptimaliseerd. Door middel van dit onderzoek werden configuraties gevonden die een dubbel zo grote veldsterkte produceerden in het doelgebied in vergelijking met de configuraties die tot op heden standaard gebruikt worden. Optimalisatie van de richting leidde tot een veel kleinere verbetering. Uiteindelijk werden de resultaten van alle doelgebieden in relatie tot elkaar geanalyseerd.

In dit proefschrift werden voor het eerst zes configuraties en doelgebieden onderzocht met hetzelfde model, waarbij dit model ook nog gedetailleerder was dan eerder gebruikte modellen. Door de uitgebreide opzet van deze studies konden voor het eerst algemene conclusies worden getrokken over de plaatsing van tDCS elektrodes en de resulterende velden. Deze sectie van het proefschrift resulteert in een serie adviezen voor optimale elektrodeplaatsing voor ieder doelgebied in de hersenen dat relatief dichtbij de schedel ligt.

## Vergelijken van conventionele en geoptimaliseerde tDCS

In de laatste studie van dit proefschrift werden de optimale configuraties uit de voorgaande simulatiestudie experimenteel getest met gezonde proefpersonen. De motorische cortex werd gekozen als doelgebied voor deze experimenten. De twee optimale configuraties, voor elektrische veldsterkte en -richting, werden vergeleken met de configuratie die tot op heden standaard gebruikt wordt voor stimulatie van de motorische cortex. Het effect van de stimulatie werd geëvalueerd door voor en na het toepassen van tDCS de exciteerbaarheid van de motorische cortex te meten met behulp van TMS en EMG. De gemiddelde resultaten van de groep lieten een verhoogde exciteerbaarheid zien na tDCS met de conventionele configuratie. De configuratie geoptimaliseerd voor sterkte en richting leverde een iets groter effect op. Er was vrijwel geen effect voor de configuratie die een maximale veldsterkte

oplevert in het doelgebied. Deze resultaten suggereren dat elektrische veldsterkte, de tot op heden meest gebruikte maat in tDCS simulatiestudies, niet bepalend is voor de effecten van tDCS op het brein en dat de richting van de stroom in toekomstige studies moet worden onderzocht. Echter, op individueel niveau waren er zeer grote verschillen. Bij sommige proefpersonen werden de grootste effecten verkregen met een configuratie die voor anderen vrijwel geen effect opleverde en vice versa. Deze resultaten konden niet verklaard worden door de modelresultaten aangaande veldsterkte en richting. Er zijn vele individuele factoren in de toestand van het brein die dergelijke verschillen op zouden kunnen leveren en er is meer onderzoek nodig om hier conclusies over te kunnen trekken.

## Conclusie

Het is sinds enkele jaren mogelijk om volumegeleidingsmodellen van tDCS te maken met een zeer hoge kwaliteit en hier worden dan ook steeds meer studies aan gewijd. De meeste van deze studies laten echter na om de gevonden theoretische resultaten in de praktijk te testen. Dit proefschrift beschreef één van de eerste studies waarin theoretisch geoptimaliseerde configuraties ook experimenteel werden getest. De resultaten konden niet verklaard worden met behulp van het model en toonden aan dat de huidige ideeën over de werkingsmechanismen van tDCS niet correct lijken te zijn. Hieruit moeten we concluderen dat de praktische toepasbaarheid van dergelijke modellen beperkt is totdat we meer weten over de werking van tDCS. Echter, de koppeling tussen de resultaten van model en experimenten leverde juist informatie over de werking van tDCS die met modellen of experimenten alleen niet gevonden had kunnen worden.

## Onderschriften bij figuren

**Figuur 1.3** Illustratie van het meten van de exciteerbaarheid van neuronen door middel van TMS en EMG. Een stroompuls in een magneetspoel (b: zwart) boven de motorische cortex (blauw) wekt een magnetisch veld (paars) op dat een elektrisch veld (groen) opwekt in de hersenen. De gele pijlen geven de stroomrichting aan. Het stroompje dat wordt opgewekt wordt via zenuwbanen doorgegeven aan een spier. Omdat we weten welk gedeelte van de motorische cortex welke spieren aanstuurt (a) kunnen we selecteren welke spier we willen stimuleren. Als we bijvoorbeeld kiezen voor een spier in de hand en hier EMG meten (c) levert dit een specifiek signaal op (d).

**Figuur 1.7** Vier stappen in het productieproces van een volumegeleidingsmodel. Op een MRI scan (a) worden de verschillende weefseltypen aangegeven (b), waarna deze worden omgezet in omhulsels van ieder compartiment (c) en deze worden vervolgens opgevuld met tetraeders (d).

**Figuur 3.1** Simulaties van tDCS van de auditieve cortex (a,b) en motorische cortex (c,d). De plaatsing van de elektrodes wordt aangegeven in figuren a en c, waarbij de anode rood en de kathode blauw is. Figuren b en d tonen de stroomdichtheid tijdens stimulatie op een doorsnede door het hoofd ter hoogte van het midden van de anode. De pijlen geven de richting van de stroom aan en de kleur de sterkte, waarbij blauw minimaal en rood maximaal is. Deze figuren laten goed zien hoe de stroom loopt van anode naar kathode.

**Figuur 4.3a** Standaard tDCS elektrodeconfiguratie voor het stimuleren van de motorische cortex. De anode (rood) wordt boven de motorische cortex geplaatst en de kathode (blauw) op het voorhoofd. Deze stimulatie leidt tot een toename in exciteerbaarheid. Als de anode en kathode verwisseld worden leidt dit tot een afname van exciteerbaarheid.

**Figuur 4.6a-e** Simulaties van het elektrische veld ten gevolge van tDCS met vijf verschillende elektrodeconfiguraties die regelmatig gebruikt voor het stimuleren van verschillende gebieden in de hersenen. De zwarte lijnen geven de plaatsing van de elektrodes weer en de zwarte bollen geven aan waar het doelgebied ligt. De sterkte van het elektrische veld wordt getoond op het oppervlak van de hersenen, waarbij blauw minimaal en rood maximaal is. In alle vijf de gevallen is duidelijk te zien dat de veldsterkte maximaal is in een gebied dat ver van het doelgebied af ligt.





Na bijna zes jaar sluit ik nu dan eindelijk mijn promotie af. In deze periode heb ik ontzettend veel geleerd, inhoudelijk over mijn onderzoek en over de wetenschap in het algemeen, maar ook over mezelf en de mensen om me heen. Daarnaast heb ik interessante mensen leren kennen, vrienden gemaakt en veel leuke en bijzondere nieuwe ervaringen opgedaan. Helaas waren er ook behoorlijke tegenvallers en zware tijden. Gelukkig kwam er, uit verschillende hoeken, altijd hulp en steun. Ook was er de nodige afleiding. Voor dit alles zijn er een aantal mensen die ik wil bedanken.

## **Promotores**

Dick, jouw deur stond letterlijk altijd open. Het was een luxe om jou als promotor te hebben: op elke vraag binnen een paar uur antwoord en het commentaar op manuscripten arriveerde veelal binnen een dag. Zelfs het kleinste commentaar – soms kwam het per app – hielp me altijd weer vele stappen vooruit. Je hebt jaren geprobeerd om mijn perfectionisme te reduceren, wat helaas onmogelijk bleek, maar ik heb zeker geleerd om sneller om advies te vragen. Vanaf het begin heb je me alle vrijheid gegeven in mijn onderzoek en niet alleen het vertrouwen gehad dat het goed zou komen, maar dat ook getoond. Je zorgde dat we alle kansen kregen om ons onderzoek te presenteren en kwam voor ons op als dat nodig was. Je betrokkenheid was altijd oprecht, ook buiten de wetenschap: van congresfoto's tot reisverslagen, je hing het trots in de koffiekamer.

Thom, ook jij was er altijd, maar dan virtueel. Een mail over een bug leverde me vaak de volgende dag al een nieuw programma op. Je hielp me niet alleen met mijn modellen, maar ook met ieder ander probleem dat mijn computer bracht. En dat waren er onwaarschijnlijk veel. Elk antwoord kwam met uitgebreide uitleg, af en toe een RTFM, maar 'cross 13' hadden we ook inderdaad zelf moeten kunnen bedenken ;) Zonder jouw programma's en hulp had mijn onderzoek er heel anders uit gezien.

Dick en Thom, jullie zijn als een wetenschappelijke vader en oom, bedankt voor alles. Het waren mooie tijden en ik heb veel van jullie geleerd. Het was zeker niet altijd makkelijk, maar aan jullie heeft dat niet gelegen.

## **Kamergenootjes**

Moniek en Arno, de afgelopen jaren deelden we niet alleen een kamer, maar ook vele leuke en moeilijke momenten tijdens onze promoties. Van verhuizingen tot overstromingen en van onterechte reviews tot lovende, studies met en zonder resultaten, en vooral heel veel taart. Als de deur dicht ging werd er óf geklaagd óf heel hard

gelachen. Wat het ook was, het hielp altijd. Ook buiten het huis hebben we van alles ondernomen: de pannenkoekenavonden, avondjes karten of skiën, na congressen samen op pad in Rome en Denemarken, vele tripjes naar Münster (soms met een omweg) en road trips door Utah. Dank voor de gezelligheid, steun en hulp. Moniek, bedankt voor je hulp bij allerlei praktische zaken; je leerde me de weg in het ziekenhuis toen ik begon, maar hebt me ook daarna vaak geholpen. Arno, bedankt dat ik jouw brein heb mogen lenen voor twee van de studies in dit proefschrift, en voor de cover. Ik vind het erg jammer dat ik niet bij jullie promoties kan zijn en dat Moniek ook de mijne zal missen. Gelukkig weten we inmiddels alle drie dat er meer in de wereld is dan werk en dat iedere kans om er wat van te zien met beide handen moet worden gegrepen.

## Op de KNF

Angelique Arnoldussen, ook wij hebben veel samengewerkt, maar dan op een ander vlak: van razende reporters tot eindredacteuren van de website. En ook wij hebben veel gekletst, geklaagd en gelachen. Daarnaast kon ik altijd bij je terecht met vragen en problemen omtrent alles wat administratief was. Bedankt voor al je hulp.

Vincent Jansen, het was een plezier om zo een leergierige student te mogen begeleiden bij zijn stage. De vele uren die we in het lab doorbrachten, soms resulterend in een TMS-arm, hebben een mooi artikel opgeleverd. Het resultaat was niet wat we hoopten, maar des te meer hebben we ervan geleerd. Bedankt voor je bijdrage.

Mark Massa en Leo Haegens, bedankt voor de technische ondersteuning bij de opzet van mijn experimenten. Van het maken van nieuwe elektrodes tot metingen aan een meloen, jullie stonden altijd klaar om te helpen. Nens van Alfen, bedankt voor de ondersteuning met de proefpersonen.

Verder wil ik graag alle onderzoekers, laborantes en artsen van de KNF, en de vele studenten die in de afgelopen jaren voorbij zijn gekomen, bedanken voor het delen in elkaars onderzoek, de gezelligheid op de afdeling en buiten het ziekenhuis tijdens dagjes uit en andere activiteiten.

## Onderzoekers

Edwin van Asseldonk, bedankt voor je bijdrage aan de analyse van de tDCS experimenten en het artikel dat eruit voortkwam. Met jou samenwerken is niet alleen leerzaam en nuttig, maar ook Brabants gezellig.

Carsten Wolters, Sven Wagner, Felix Lucka, Benjamin Lanfer, Ümit Aydin, Johannes Vorwerk and Seok Lew, our combined efforts have resulted in three publications, of

which two are part of this thesis. Thank you for the many fruitful discussions and collaborations. Special thanks to Carsten for inviting us repeatedly to his lab, but also to his home.

Til Ole Bergman, Lennart Verhagen en alle andere deelnemers aan de brain stimulation meetings, bedankt voor de nuttige en prettige interactie tijdens de meetings en daarbuiten, en voornamelijk Til voor de discussies over tDCS.

## **Vriendjes..**

Juul en Frank, twaalf jaar geleden begonnen we samen aan onze studie, we kozen dezelfde afstudeerrichting en gingen stage lopen op dezelfde afdeling. Van een roterende stoel tot oogspoeltjes, we deden aan al elkaars experimenten mee, maar het was vooral gezellig. Toen ik begon met mijn promotie op de KNF kon ik de lunches met Frank daar voortzetten. Helaas was jouw stage eerder afgerond dan mijn promotie en verhuisde je naar Den Haag. De wekelijkse etentjes met zijn drieën werden maandelijks en uiteindelijk jaarlijks, maar de gezelligheid bleef onveranderd. Frank, toen je van de andere kant van de Plato naar de andere kant van het land vertrok vond ik dat erg jammer. Ik was altijd blij met je spontane bezoeken in Nijmegen en Arnhem. Juul, wij hebben tijdens onze promoties nog ontelbare uren samen doorgebracht voor een 'snelle lunch'. We begrijpen elkaar meestal volkomen en het is heerlijk om samen te klagen over alles wat er mis is met de wereld en iedereen die niet zo nerderig is als wij ;) Het mag de problemen niet opgelost hebben, vrolijk werden we er wel van. Na al die jaren is er nu dan toch een einde gekomen aan onze lunches en etentjes. Gelukkig komen jullie al snel langs in Boston. Met jullie ben ik mijn studie en wetenschappelijke carrière begonnen en ik ben blij dat jullie straks naast mij staan als ik voor de laatste titel ga. Bedankt voor alle steun en hulp gedurende de jaren en dat jullie mijn paranimfen willen zijn.

## **..en vriendinnetjes**

Hetty en Britt, als collega's begonnen we aan een salsacursus en als vriendinnen kwamen we eruit. Vele dansavondjes en etentjes volgden. We konden samen kletsen over werk, maar ook over alles daarbuiten. Bedankt voor de gezelligheid en de afleiding. Britt, succes met jouw promotie! Hetty, we gingen van slechts een vloer/plafond tussen ons op de Pluto, naar een oceaan, en dus van uurtjes bij de lift naar uurtjes op de app. Het afgelopen jaar was je ook mijn persoonlijke helpdesk voor praktische zaken rondom promotie en visa. Bedankt voor alle antwoorden en tips. Inmiddels wonen we weer in dezelfde tijdzone en binnenkort doen we weer een dansje in New York. Con musica!



Ook anderen brachten de nodige afleiding in het Nijmeegse leven. Maris, de frequentie waarmee we elkaar zagen was chronisch te laag, maar met ons gemiddelde spreektempo haalden we dat ruimschoots in. Leonie, ons wekelijkse squash-uurtje was vooral therapeutisch: lekker bijkletsen en tegelijkertijd afreageren. Ook jij bent nu eindelijk klaar. Ik wens je onmeunig veel succes met je nieuwe baan. De combinatie sport en gezelligheid was er ook in de vele uurtjes met Debbie, Mandy en Lonneke. Jullie vingen mij letterlijk op als ik viel. Ik begon net na de start van mijn promotie en stopte net voor het einde. Daar tussenin hielden al die uurtjes me niet alleen lichamelijk gezond, maar zeker ook geestelijk.

## Brabantse gezelligheid

Na mijn verhuizing naar Nijmegen, de start van mijn promotie, en later mijn verhuizing naar Arnhem, kwam ik steeds een beetje minder vaak in Oirschot. Ondanks dat, is het bij ieder bezoekje alsof ik nooit ben weg geweest. Ik heb er dan ook alle vertrouwen in dat dit niet verandert nu ik weer wat verder weg ben verhuisd. De belangrijkste mensen zijn niet degenen die je het vaakst ziet, maar degenen die er altijd zijn, ook al zie je ze nooit.

Mijn familie: mam, pap, Cathrien, Hendrik, Bas, Tijn, Floris en Oliver; en vriendinnen: Daan, Lies, Laura, Linda en Anne; bedankt voor alle gezelligheid tijdens verjaardagen, etentjes en andere feestjes. Vaak zonder het door te hebben, hebben ook jullie mij geholpen. Een aantal mensen in het bijzonder:

Bianca, jij gaf me het gevoel alsof de rit naar Nijmegen niet verder was dan een ritje naar de supermarkt. Het was altijd gezellig als je op bezoek kwam, maar ook gewoon fijn om een beetje 'thuis' in Gelderland te hebben.

Lin, je sleepte me regelmatig naar een feestje als ik weer eens geen tijd had, want "je moet ook ontspannen". En je had natuurlijk gelijk. In een paar uurtjes danste ik er heel wat frustratie uit en daarna kon ik er weer even tegen. Op zo'n avond of dag leek alles inderdaad even "just as easy as 123".

As en Frans, jullie huis was voor mij ook thuis. Ik kon altijd bij jullie terecht, zowel gepland als spontaan, voor een middag of een heel weekend. As, het was meestal zo gezellig dat ik uren langer bleef dan gepland, maar ook als ik juist opgevrolijkt moest worden leek een uur naar Oirschot rijden een hele logische keus.

Ien, ook in Engeland altijd welkom. Je verjaardag was mijn jaarlijkse mini-vakantie. Soms lag ik in de stoel, soms speelde ik je assistente, maar niemand ging met zoveel plezier naar de tandarts als ik.

Chit, de ritjes naar Nijmegen brachten je vooral veel ellende met de auto, maar gelukkig kwam je toch steeds terug. Niet alleen erg gezellig, maar ook zeer gewaardeerd. Waar ik ook woon, het plekje bij de verwarming blijft voor jou.

## Thuis

Lieve Rich, toen ik je leerde kennen dacht je bij 'promoveren' vooral aan voetbal; nu kun je over dit boekje praten alsof je het zelf geschreven hebt. Wat is het fijn om thuis te komen bij iemand die zoveel interesse toont in je werk, zowel in de inhoud als alles daar omheen. Of ik nu een nieuwe publicatie heb of een nieuw Matlab plotje, je deelt oprecht mijn enthousiasme. Nog bijzonderder is hoeveel begrip jij hebt voor iets dat je zelf niet kent: of ik nu hele dagen wilde werken of hele nachten, jij klaagde nooit. Je steunt en helpt me waar je kan. Je kunt de problemen meestal niet oplossen, maar of ik nu met een onterecht review zit of met de zoveelste gecrashte harde schijf, jij weet ieder probleem in 10 seconden te laten klinken als een non-issue. Met jou is alles makkelijker. Naar Arnhem verhuizen was, ondanks de slechte timing, dan ook een hele makkelijke keus. Samen met jou naar Amerika kan alleen nog maar beter zijn. Home is where the heart is.







## Biography

---

Sumientra Rampersad was born in Ermelo, the Netherlands in 1984. Her family moved to Oirschot in 1986, where she attended primary school. She received secondary education at the Heerbeeck College in Best and graduated in 2002. Due to a wide interest in natural science, she selected the broad and interdisciplinary curriculum of the bachelor's program Natural Sciences of the Radboud University in Nijmegen to continue her education. After finishing the program with an internship at the Department of Applied Physics, an interest in research was born and she continued on with the master's program. Her studies included internships at the Department of Biophysical Chemistry, investigating the structure of an RNA molecule, and at the Department of Medical and Biophysics, researching the effects of eye movements on binocular vision. Sumientra received the Master of Natural Sciences degree with the distinction cum laude in 2008. After a period of traveling, learning Spanish and volunteering in Central America, she returned to Nijmegen to pursue the PhD degree. She started her PhD research at the Radboud University Nijmegen Medical Centre's Department of Neurology in 2009. Her wide interest in physics and the human body was again reflected in her research topic: modeling and measuring the effects of transcranial direct current stimulation. Her research led to collaborations with and short stays at the University of Münster and the University of Utah, various poster and oral presentations at both clinical and engineering conferences, several publications and, ultimately, this dissertation. Since November 2014 Sumientra has been working as a Postdoctoral Research Associate at the Department of Electrical and Computer Engineering of Northeastern University in Boston, USA.



## Publications

---

- ↔ **Simulating transcranial direct current stimulation with a detailed anisotropic human head model**  
Rampersad SM, Janssen AM, Lucka F, Aydin U, Lanfer B, Lew S, Wolters CH, Stegeman DF, Oostendorp TF  
IEEE TRANSACTIONS ON NEURAL SYSTEMS AND REHABILITATION ENGINEERING, 2014, 22(3):441-52
- ↔ **Investigation of tDCS volume conduction effects in a highly realistic head model**  
Wagner S<sup>†</sup>, Rampersad SM<sup>†</sup>, Aydin U, Vorwerk J, Oostendorp TF, Neuling T, Hermann CS, Stegeman DF, Wolters CH (<sup>†</sup>equal contribution)  
JOURNAL OF NEURAL ENGINEERING, 2014, 11(1):016002
- ↔ **The influence of sulcus width on simulated electric fields induced by transcranial magnetic stimulation**  
Janssen AM, Rampersad SM, Lucka F, Lanfer B, Lew S, Aydin U, Wolters CH, Stegeman DF, Oostendorp TF  
PHYSICS IN MEDICINE AND BIOLOGY, 2013, 58(14):4881-96
- ↔ **Single-layer skull approximations perform well in transcranial direct current stimulation modeling**  
Rampersad SM, Stegeman DF, Oostendorp TF  
IEEE TRANSACTIONS ON NEURAL SYSTEMS AND REHABILITATION ENGINEERING, 2011, 21(3):346-53
- ↔ **On handling the layered structure of the skull in transcranial direct current stimulation models**  
Rampersad S, Stegeman D, Oostendorp T  
PROCEEDINGS OF THE ANNUAL INTERNATIONAL CONFERENCE OF THE IEEE ENGINEERING IN MEDICINE AND BIOLOGY SOCIETY, 2011, 2011:1989-92
- ↔ **Binocular onset rivalry at the time of saccades and stimulus jumps**  
Kalisvaart JP, Rampersad SM, Goossens J  
PLOS ONE, 2011, 6(6):E20017

- ↔ **Ligand-induced folding of the guanine-sensing riboswitch is controlled by a combined predetermined induced fit mechanism**  
Ottink OM, Rampersad SM, Tessari M, Zaman GJ, Heus HA, Wijmenga SS  
RNA, 2007, 13(12):2202-12
- ↔ **Model-based optimization of bipolar tDCS electrode placement**  
Rampersad SM, Oostendorp TF, Stegeman DF  
*Under review*
- ↔ **Evaluating the effects of model-based optimal bipolar tDCS configurations on cortical excitability**  
Rampersad SM, Jansen VD, van Asseldonk EDM, Stegeman DF  
*Under review*



## Conference contributions

---

Only first-authored abstracts are listed here.

### Oral presentations

- ↔ Distribution of electric fields during intravenous PRF. Rampersad SM, Oostendorp TF, Stegeman DF. Invited presentation at the International Symposium 'Invasive Procedures in Motion', 2015, Nottwil, Switzerland.
- ↔ Optimized electrode configurations for five common tDCS targets determined via an inverse FE modeling approach. Rampersad SM, Oostendorp TF, Stegeman DF. International Conference on Non-invasive Brain Stimulation, 2013, Leipzig, Germany.
- ↔ A finite element modeling approach to finding optimal stimulation configurations for tDCS. Rampersad SM, Oostendorp T.F., Stegeman D.F. Dutch Biomedical Engineering Conference, 2013, Egmond aan Zee, the Netherlands.
- ↔ tDCS: stimulation and simulation. Rampersad SM, Oostendorp TF, Stegeman DF. Invited presentation at the Institutscolloquium Biomagnetismus und Biosignalanalyse, 2012, Münster, Germany.
- ↔ Effects of transcranial direct current stimulation on motor network connectivity in resting state fMRI. Rampersad SM, van den Akker BPG, Zwiers MP, Norris DG, Stegeman DF. Congress of the International Society of Electrophysiology and Kinesiology, 2010, Aalborg, Denmark.

### Poster presentations

- ↔ A finite element modelling approach to finding optimal stimulation configurations for tDCS. Rampersad S, Oostendorp T, Stegeman D. Magstim Neuroscience Conference, 2012, Oxford, UK.
- ↔ On handling the layered structure of the skull in transcranial direct current stimulation models. Rampersad SM, Stegeman DF, Oostendorp TF. Annual International Conference of the IEEE Engineering in Medicine and Biology Society, 2011, Boston, USA.
- ↔ Modeling transcranial stimulation using a realistic volume conductor model. Janssen AM, Rampersad SM (presenter), Lucka F, Lew S, Oostendorp TF,

Wolters CH, Stegeman DF. Jahrestagung der Deutschen Gesellschaft für Hirnstimulation in der Psychiatrie, 2011, Münster, Germany.

- ↔ Determining the optimal electrode configuration for transcranial direct current stimulation: a model study. Rampersad SM, Oostendorp TF, Janssen AM, Wolters CH, Stegeman DF. European Congress on Clinical Neurophysiology and International Conference on Transcranial Magnetic and Direct Current Stimulation, 2011, Rome, Italy.
- ↔ Incorporating the layered structure of the skull into transcranial direct current stimulation models. Rampersad SM, Oostendorp TF, Stegeman DF. Dutch Biomedical Engineering Conference, 2011, Egmond aan Zee, the Netherlands.
- ↔ No effect of transcranial direct current stimulation on motor network connectivity in resting state fMRI. Rampersad SM, van den Akker BPG, Zwiers MP, Norris DG, Stegeman DF. FENS Satellite Symposium on Motor Control, 2010, Nijmegen, the Netherlands.
- ↔ No effect of transcranial direct current stimulation on motor network connectivity in resting state fMRI. Rampersad SM, van den Akker BPG, Zwiers MP, Norris DG, Stegeman DF. Magstim and University of Oxford TMS Summer School, 2010, Oxford, UK.





